JOINT TRANSPORTATION
RESEARCH PROGRAM
INDIANA DEPARTMENT OF TRANSPORTATION
AND PURDUE UNIVERSITY

Monitoring of a Steel-Reinforced MSE Abutment Wall and Evaluation of its Bearing Capacity Based on the CPT and DCPT

Venkata A. Sakleshpur, Monica Prezzi,
Rodrigo Salgado, Peter Becker, Yaser Zafari

SPR-4329 • Report Number: FHWA/IN/JTRP-2025/04 • DOI: 10.5703/1288284317845

RECOMMENDED CITATION

Sakleshpur, V. A., Prezzi, M., Salgado, R., Becker, P., & Zafari, Y. (2025). *Monitoring of a steel-reinforced MSE abutment wall and evaluation of its bearing capacity based on the CPT and DCPT* (Joint Transportation Research Program Publication No. FHWA/IN/JTRP-2025/04). West Lafayette, IN: Purdue University. https://doi.org/10.5703/1288284317845

AUTHORS

Venkata A. Sakleshpur
Graduate Research Assistant
Lyles School of Civil Engineering
Purdue University

Monica Prezzi, PhD
Professor of Civil Engineering
Lyles School of Civil Engineering
Purdue University
(765) 494-5034
mprezzi@ecn.purdue.edu
Corresponding Author

Rodrigo Salgado, PhD
Charles Pankow Professor of Civil Engineering
Lyles School of Civil Engineering
Purdue University

Peter Becker, PhD, PE
Research Engineer
Indiana Department of Transportation

Yaser Zafari
Graduate Research Assistant
Lyles School of Civil Engineering
Purdue University

JOINT TRANSPORTATION RESEARCH PROGRAM

The Joint Transportation Research Program serves as a vehicle for INDOT collaboration with higher education institutions and industry in Indiana to facilitate innovation that results in continuous improvement in the planning, design, construction, operation, management and economic efficiency of the Indiana transportation infrastructure. https://engineering.purdue.edu/JTRP/index_html

Published reports of the Joint Transportation Research Program are available at http://docs.lib.purdue.edu/jtrp/.

NOTICE

ACKNOWLEDGEMENTS

This research was funded with the support provided by the Indiana Department of Transportation (INDOT) through the Joint Transportation Research Program (JTRP) at Purdue University. The authors greatly appreciate the continuous support received from the JTRP director, Prof. Darcy Bullock, the director of INDOT Research and Development, Dr. Barry Partridge, and the Study Advisory Committee members (Aamir Turk, Athar Khan, Nayyar Zia Siddiki, and Boonam Shin). The authors are grateful for the correspondence with Prof. Richard Bathurst regarding the distribution of the strain gauges along the steel strip reinforcements. The authors thank Kyle Zak, Matt Mickelson, Peter Danzl-Tauer, Abby Sheehan, and Andy Najafiarab from Terracon for the MSE bridge abutment instrumentation; Rameez Raja, Riccardo Zabatta, Marcelle Barcellos, and Guilherme Borges for the backfill and foundation soil classification tests; and Satish Kumar Adari and Rodrigo Velten for the live load test operation. The authors thank Dr. Farshid Sadeghi and his students (Kushagra Singh, Saeed Aamer, and Ujjawal Arya) for their assistance with performing the optical profilometer tests at Kepner Laboratory, Purdue University. The authors are also thankful to Iqbal Khan from INDOT for the site investigation, to Charlie Aimone and Jared Bowman from Beaty Construction, Inc., for the bridge construction operations, to Rob Clark and Shawn Dedeker from Geokon for technical support with the instrumentation work, and to Zay Fox and Emily Stover from Fox Hauling & Construction, Inc., for the trucking logistics.

TECHNICAL REPORT DOCUMENTATION PAGE

1. Report No. FHWA/IN/JTRP-2025/04	**2. Government Accession No.**	**3. Recipient's Catalog No.**
4. Title and Subtitle Monitoring of a Steel-Reinforced MSE Abutment Wall and Evaluation of its Bearing Capacity Based on the CPT and DCPT		**5. Report Date** January 2025 **6. Performing Organization Code**
7. Author(s) Venkata A. Sakleshpur, Monica Prezzi, Rodrigo Salgado, Peter Becker, and Yaser Zafari		**8. Performing Organization Report No.** FHWA/IN/JTRP-2025/04
9. Performing Organization Name and Address Joint Transportation Research Program Hall for Discovery and Learning Research (DLR), Suite 204 207 S. Martin Jischke Drive West Lafayette, IN 47907		**10. Work Unit No.** **11. Contract or Grant No.** SPR-4329
12. Sponsoring Agency Name and Address Indiana Department of Transportation (SPR) State Office Building 100 North Senate Avenue Indianapolis, IN 46204		**13. Type of Report and Period Covered** Final Report **14. Sponsoring Agency Code**

15. Supplementary Notes

Conducted in cooperation with the U.S. Department of Transportation, Federal Highway Administration.

16. Abstract

A two-span bridge, supported by steel H-piles and mechanically stabilized earth (MSE) bridge abutments, was constructed as part of a new interchange on I-65 in Whitestown, Indiana. The east and west MSE abutment walls consisted of precast concrete facing panels, ribbed steel strips, and coarse-grained backfill soil. A section near the middle of the east MSE abutment wall was selected for instrumentation and performance monitoring. A variety of sensors, including earth pressure cells, strain gauges, inclinometers, and crackmeters were used to measure the magnitude and evolution of several quantities, such as the vertical stresses at the base of the leveling pad and within the backfill soil, the lateral stresses on the back of the wall facing, the tensile loads in the reinforcement, the lateral deflection of the wall facing, the contraction of the panel joints, and the settlement of the MSE wall foundation. The data was collected continuously, both during and after bridge construction, using multiplexers and dataloggers powered by solar panels. The results indicated that the vertical stresses measured at the base of the leveling pad were greater than those measured along the base of the reinforced fill and those calculated based on the self-weight of the wall facing. The values of key parameters used in MSE wall design were determined from the instrumentation results and compared with those obtained using design methods available in literature. The relationship developed by INDOT between the DCPT blow count and the factored bearing resistance of MSE wall foundations constructed over fine-grained soils was verified based on the results of the DCPTs performed in this study. In addition, a preliminary procedure to estimate the limit unit bearing capacity of the leveling pad in compacted B-borrow material was developed as a function of the pad width and the DCPT blow count for 0–12 in. penetration.

17. Key Words bridge, MSE abutment wall, steel strip reinforcement, instrumentation, monitoring, data collection, live load test	**18. Distribution Statement** No restrictions. This document is available through the National Technical Information Service, Springfield, VA 22161.

19. Security Classif. (of this report) Unclassified	**20. Security Classif. (of this page)** Unclassified	**21. No. of Pages** 68	**22. Price**

EXECUTIVE SUMMARY

Introduction

A two-span bridge, supported by steel H-piles and mechanically stabilized earth (MSE) bridge abutments, was constructed as part of a new interchange on I-65 in Whitestown, Indiana. The east and west MSE abutment walls consisted of precast concrete facing panels, ribbed steel strips, and coarse-grained backfill soil. A section near the middle of the east MSE abutment wall was selected for instrumentation and performance monitoring. The instrumented wall section consisted of four panels with seven levels of reinforcement. The main goals of the project were (1) to investigate the performance of a steel strip-reinforced MSE abutment wall during construction and while in service, and (2) to verify, based on the dynamic cone penetration test (DCPT) blow count, the INDOT procedure for estimating the factored bearing resistance of MSE wall foundations in fine-grained soils.

This report presents the site investigation results, the instrumentation layout, and the response of the MSE abutment wall to both dead and live loads for various stages during and after construction of the Whitestown Parkway Bridge. The instrumentation included earth pressure cells, strain gauges, inclinometers, and crackmeters. These sensors were used to measure the magnitude and evolution of several quantities, such as the vertical stresses at the base of the leveling pad and within the backfill soil, the lateral stresses on the back of the wall facing, the tensile loads in the reinforcement, the lateral deflection of the wall facing, the contraction of the panel joints, and the settlement of the MSE wall foundation. The data was collected continuously using multiplexers and dataloggers powered by solar panels.

Findings

- The ratio of the vertical stress measured at the base of the leveling pad to the vertical stress calculated based on the self-weight of the wall facing increased from 1.6 at stage 1 of wall construction to 2.4 at stage 5 (the end of wall construction). It subsequently increased to 3.2 after the bridge was constructed and opened to traffic (stage 11). The factor of safety for the leveling pad against bearing capacity failure was estimated to be 3.0 at the end of wall construction and 2.3 after the bridge was constructed and opened to traffic.
- Based on the data obtained from the three instrumented piles and the instrumented zone of the pile cap around these piles, the piles carried about 90% of the dead load from the superstructure during bridge construction, while the remaining 10% was carried by the fill material in contact with the pile cap. The mobilized cap resistance decreased to about 8% at the end of bridge construction and to 6% after the bridge opened to traffic for 4 months. Assuming no contribution from cap resistance (as is typically done in MSE abutment design), the average dead load per pile, which was based on the data obtained for the three instrumented piles, was 477 kN (107 kips) at the end of bridge construction. This value agreed with the unfactored dead load of 456 kN (103 kips) per pile in the design of Bent 3 of the Whitestown Parkway Bridge. During the live load test, approximately 91% of the live load in the instrumented zone of the pile cap was carried by the three instrumented piles, while the remaining 9% of the live load was carried by the fill material in contact with the pile cap.
- The coherent gravity method, the simplified method and the simplified stiffness method are sensitive to the value of the backfill soil peak friction angle ϕ_p used to calculate T_{max} at the end of wall construction. For $\phi_p = 40^\circ$, the simplified stiffness method provided the best estimate of T_{max} for the four instrumented levels of steel strips considered in this study, whereas for $\phi_p = 34^\circ$, the methods generally overpredicted the maximum reinforcement tensile loads at the end of wall construction. For the Whitestown MSE abutment wall, the value of T_{max} increased by about 3%–5% during the time period between the end of bridge construction until up to 4 months after the bridge was opened to traffic. Because the contribution of dilatancy towards soil shear strength may progressively degrade during the service life of the MSE abutment wall due to traffic and other events (e.g., earthquakes and rainstorms), the critical-state friction angle ϕ_c of the backfill soil could be the most appropriate value of friction angle to use in MSE abutment wall design.
- The maximum lateral displacement of the wall facing [= 12.1 mm (0.48 in.) or 0.24% of the height H of the reinforced fill] at the end of bridge construction occurred at a depth of 2.8 m (9.2 ft or 0.56 H) below the top of the reinforced fill; this is close to the depth where the maximum tensile load T_{max} [= 21.8 kN/m (1,494 lb/ft)] was measured in the instrumented steel strips. During the live load test, the lateral displacement of the wall facing increased by a maximum value of 0.8 mm (0.03 in.) compared to the measurement before the test; this occurred at a depth of 0.3 m (1 ft or 0.06H), which was near the elevation of the topmost reinforcement level, where the largest increment in tensile load [= 0.9 kN/m (62 lb/ft)] was measured during the test.
- The vertical displacement w of the MSE wall foundation (below the leveling pad) increased from 20 mm (0.8 in.) at the end of wall construction to 26 mm (1.02 in.) at the end of bridge construction; no significant change in pad settlement was observed during the live load test. The relative settlement w/B of the leveling pad was 6.5% at the end of wall construction and 8.5% at the end of bridge construction. The value of the secant modulus of subgrade reaction of the leveling pad decreased by 20%: from 11,450 kPa/m (73 ksf/ft) for a pad settlement of 12.7 mm (0.5 in.) to 9,150 kPa/m (58 ksf/ft) for a pad settlement of 25.4 mm (1.0 in.).
- The results of the DCPTs performed in the foundation soil prior to wall construction showed that the factored bearing resistance [= 6,600 psf (316 kPa)] obtained using the chart in *INDOT Construction Memorandum 15–08* (Miller, 2015) was greater than the factored bearing pressure [= 5,100 psf (244 kPa)] at the base of the MSE wall foundation specified in the contractor's working drawing. In addition, the value of 6,600 psf (316 kPa) was close to the MSE wall factored bearing resistance of 7,000 psf (335 kPa) derived from the geotechnical report (based on the bearing capacity equation) and specified in the project contract documents.

Implementation

The following steps should be considered for the preparation and testing of the MSE wall foundation.

1. Perform SPT borings and CPT soundings as part of the initial site investigation to determine the site stratigraphy and foundation soil profile for the MSE wall project.
2. Excavate weak, fine-grained, surficial soil layers below the MSE wall foundation based on the geotechnical report for the specific MSE wall project under consideration.
3. After excavation, compact and proof-roll the surface of the fine-grained foundation soil in accordance with INDOT specifications.
4. Perform plate load tests in accordance with AASHTO (2020) and ASTM D1194 on the proof-rolled, fine-grained foundation soil (along the footprint of the MSE wall) to obtain an unfactored bearing resistance of at least 3 tsf for MSE walls shorter than 20 ft high.
    a. A plate diameter of 12 in. (30 cm) may be used for MSE walls shorter than 20 ft (6 m) high, whereas a larger plate diameter of 30 in. (75 cm) is suggested for MSE walls taller than 20 ft (6 m). According to ASTM D1194, the plate load test should be performed until a peak load is reached or until the total settlement reaches at least 10% of the plate diameter. Scale effects, as mentioned in AASHTO (2020), should be considered when extrapolating the results of a plate load test (which reflects the soil response to loading only up to a depth of about two plate diameters) to a full-scale MSE wall foundation. In addition, it is recommended that, prior to performing the plate load tests, the undrained shear strength of the fine-grained foundation soil at the MSE wall project location increase to a depth that corresponds to the width of the MSE wall foundation. The value of 3 tsf (300 kPa) for the unfactored bearing resistance was derived based on a typical backfill soil unit weight of 120 pcf (18.85 kN/m^3) and a factor of safety of 3 against bearing capacity failure. Further research is needed to determine the unfactored bearing resistances for Indiana soils from plate load test results.
5. Backfill the excavation with compacted B-borrow material and follow the quality control procedures provided in INDOT specifications.
6. Construct the MSE wall on top of the compacted B-borrow material.

Based on the results of the instrumentation of the Whitestown MSE abutment wall, the following points may be considered for implementation in MSE wall design.

1. Determine the critical-state friction angle ϕ_c of the backfill soil from direct shear or triaxial compression test results and perform MSE wall external and internal stability design checks using ϕ_c to account for potential degradation of the dilative component of soil shear strength during the service life of the MSE abutment wall.
2. For the reinforcement-panel connection limit state check, set the value of the reinforcement-panel connection load T_{con} equal to the value of the maximum tensile load T_{max} in the reinforcement.
3. Perform preliminary bearing capacity and factor of safety calculations for the leveling pad with the assumption that the unfactored bearing pressure (or unit load) at the base of the leveling pad is equal to two to three times the vertical stress due to the self-weight of the wall facing. Increase the width of the leveling pad and/or the concrete grade, as needed, to ensure the stability and serviceability of the wall.

TABLE OF CONTENTS

LIST OF TABLES

LIST OF FIGURES

1. INTRODUCTION

1.1 Background

Mechanically stabilized earth (MSE) walls have been designed and constructed in the United States and around the world for several decades (Miyata & Bathurst, 2012a). Schlosser (1978) and Mitchell and Villet (1987) reviewed the history and development of the reinforced earth technology and the construction of MSE walls. Over the past two to three decades, MSE walls have been used to serve as bridge abutments. MSE bridge abutments are primarily of two types: "direct" abutments and "mixed" abutments (Anderson & Brabant, 2005; Jones, 1996). In a direct MSE abutment, the bridge beams are supported by a spread footing constructed directly on top of the reinforced fill; the MSE wall retains the approach embankment and supports the loads from the bridge (Anderson et al., 2012; Zevgolis & Bourdeau, 2007). A mixed MSE abutment; however, is a pile-supported abutment, where the wall facing provides lateral support for the reinforced fill, while the piles support mainly the loads from the bridge (FHWA, 2009a, b).

MSE wall systems are designed against both external and internal stability ultimate limit states (AASHTO, 2020; Anderson et al., 2012; Bathurst, 2014, 2019; FHWA, 2009a). The external stability ultimate limit states include sliding, overturning, bearing capacity failure, and global stability (Kim & Salgado, 2012a; Leshchinsky et al., 2012; Luo, 2022; Stark et al., 2019), while the internal stability ultimate limit states include reinforcement rupture, reinforcement pullout, and reinforcement-facing connection failure (Bathurst et al., 2021; Bozorgzadeh et al., 2020; Huang et al., 2012; Kim & Salgado, 2012b). MSE bridge abutments are similar in principle to MSE walls, except that they are subjected to both dead loads from the bridge superstructure as well as live loads from vehicular traffic throughout their entire service life.

Limited studies have been performed to investigate the response of full-scale, instrumented MSE abutment walls to dead or live loads. Runser (1999) reported the construction of mixed MSE abutment walls [consisting of cruciform concrete panel facing, ribbed steel strip reinforcement, and a row of seven H-piles (HP 14×74) behind the wall facing] to support twin, parallel, single-span bridges on US 24 over Minnow Creek, Indiana. The instrumentation results for the south abutment wall were presented by Runser et al. (2001), but the 55.4-ft-(16.9-m)-high instrumented wall section did not consist of piles because the section was located between the eastbound and westbound bridges. The performance of 15 instrumented, steel strip-reinforced MSE walls were reported by Allen et al. (2001); out of these, only two, besides the Minnow Creek wall, were MSE abutment walls: an 18.4-ft-(5.6-m)-high mixed MSE abutment constructed near Lille, France, and a 41.3-ft-(12.6-m)-high direct MSE abutment in Ngauranga, New Zealand (for both these abutments, only the tensile loads in the steel strips were reported). Farouz et al. (2004) presented a case study of a 79.4-ft-(24.2-m)-high, tiered, mixed MSE abutment with steel strip reinforcement and closed-ended pipe piles (filled with concrete and socketed into bedrock) to support a two-span bridge in Richmond, Virginia. Liang and Almoh (2004) instrumented four sections [wall height = 20.0–51.8 ft (6.1–15.8 m)] of a steel strip-reinforced, mixed MSE abutment, with a row of 22 H-piles (HP 14×74) behind the wall facing, for bridge support in Muskingum County, Ohio. Abu-Hejleh et al. (2002) presented a case study of instrumented geosynthetic-reinforced soil (GRS) bridge abutments that were constructed to support a two-span bridge and approach embankment near Castle Rock, Colorado. The overall behavior of the direct GRS abutment walls [wall height = 4.5 m (14.8 ft) and 5.9 m (19.4 ft)] was considered satisfactory, with maximum post-construction outward facing displacement and bridge abutment footing settlement values of 13 mm (0.51 in.) and 11 mm (0.43 in.) (corresponding to 0.22% and 0.18% of the wall height), respectively, while the bridge was in service (Abu-Hejleh et al., 2000, 2003). Lee and Wu (2004) reported the performance of ten GRS bridge-supporting structures with different wall facings (wrapped facing, modular block facing, and rock facing); out of these, four were in-service GRS bridge abutments, while the remaining six were full-scale load tests of GRS bridge piers and abutments.

The above MSE bridge abutment studies focused mainly on the distribution of the vertical and lateral stresses in the wall-soil system, the movement of the wall facing, and the tensile loads in the reinforcements, but the evolution of the vertical stress at the base of the leveling pad, the joint gap width between facing panels, and the load transfer from the bridge superstructure to the piles during and after bridge construction have not been investigated for mixed MSE abutments. By contrast, the response of piled raft foundations to dead loads, and the load redistribution from the pile cap (raft) to the piles have been measured for bridge piers (Mandolini et al., 2005) and high-rise buildings (Shulyat'ev & Kharichkin, 2009; Yamashita et al., 2011). Han et al. (2020, 2021) reported the results of a live load test performed using twelve triaxle trucks on the seven-span Sagamore Parkway Bridge over the Wabash River in Lafayette, Indiana. The live loads were applied near one of the reinforced concrete bridge piers; both the pier and the 3×5 group of open-ended pipe piles supporting it were instrumented with strain gauges to study the transfer of superstructure loads (dead loads during bridge construction and live loads after bridge construction) from the pier to the foundation elements. According to Han et al. (2020, 2021), at the end of bridge construction, the piles carried about 77% of the dead load, while the remaining 23% was carried by the soil below the pile cap, but, during the live load test, the piles carried about 50% of the live load, while the remaining 50% was carried by the soil below the pile cap.

INDOT has expressed an interest in (1) investigating the performance of steel strip-reinforced MSE

abutment walls constructed in Indiana, and (2) verifying their procedure for estimating the factored bearing resistance of MSE wall foundations in fine-grained soils based on the dynamic cone penetration test (DCPT) blow count. In this study, we present the results of monitoring of a 25.3-ft-(7.7-m)-high, steel strip-reinforced, mixed MSE abutment constructed from 2021 to 2023 in Whitestown, Boone County, Indiana. The MSE abutment was instrumented with earth pressure cells, strain gauges, inclinometers, and crackmeters to measure its response both during and after construction (in service) as well as during a live load test performed on the bridge post-construction. The live loads were applied in multiple steps by parking twelve loaded triaxle trucks at specific locations along the approach to the instrumented MSE abutment as well as on the bridge deck near the abutment.

1.2 Subsurface Exploration for MSE Wall Projects

Proper assessment of MSE wall external stability requires knowledge of existing topography, subsurface conditions, and soil properties (Raja et al., 2023). Subsurface investigations for MSE walls generally consist of drilling borings, performing *in situ* tests, and extracting soil samples for laboratory testing (FHWA, 2009a). Although several *in situ* test methods are available for characterizing foundation soil properties (e.g., standard penetration test, cone penetration test, pressuremeter test, and dilatometer test), the vast majority of subsurface explorations involve solely the standard penetration test (SPT). SPT testing yields blow count data that can be correlated with the relative density of sandy soils (Skempton, 1986); however, SPT blow count correlations are unreliable for clayey soils (Salgado, 2022). Whenever possible, geotechnical engineers also perform cone penetration tests (CPTs) to complement the SPT investigation (Dagger et al., 2018; Niazi, 2021; Sakleshpur et al., 2022a, 2022b). Unlike with the SPT blow count, the CPT cone resistance q_c has been shown to correlate well with the relative density D_R of sandy soils and the undrained shear strength s_u of clayey soils (Lunne et al., 1997; Mayne, 2007; Robertson, 2009; Salgado, 2022).

1.2.1 Interpretation of CPT Results in Sand

Niazi (2021) summarized the relationships for estimation of the relative density of sandy soils from CPT results. One of them is the relationship proposed by Salgado and Prezzi (2007), which is applicable for both normally consolidated and overconsolidated sands:

$$D_R = \frac{\ln\left(\frac{q_c}{p_A}\right) - 0.4947 - 0.1041\phi_c - 0.841\ ln\left(\frac{\sigma'_h}{p_A}\right)}{0.0264 - 0.0002\phi_c - 0.0047\ ln\left(\frac{\sigma'_h}{p_A}\right)} \leq 100\% \qquad \text{(Eq. 1.1)}$$

where q_c = cone resistance, p_A = reference stress (= 100 kPa or 1 tsf), ϕ_c = critical-state friction angle (= 28°–36° for silica sand), and σ'_h = *in situ* horizontal effective stress (= $K_0\sigma'_v$), K_0 = coefficient of lateral earth pressure at rest, and σ'_v = *in situ* vertical effective stress at the depth of interest.

Sands with rounded, smooth particles and a poorly graded particle size distribution tend to have ϕ_c values close to 28°, whereas sands with angular, rough particles and a well-graded particle size distribution tend to have ϕ_c values close to 36° (Bolton, 1986; Mitchell & Soga, 2005; Salgado, 2022). The critical-state friction angle can be determined from the results of either direct shear or consolidated-drained/undrained triaxial compression tests performed on reconstituted sand samples sheared up to critical state (Carraro et al., 2009; Han et al., 2018; Lee et al., 2004; Murthy et al., 2007; Salgado et al., 2000). In the absence of such test results, the critical-state friction angle in triaxial compression can be estimated as a function of the sand morphology, gradation, and particle size using (Sakleshpur et al., 2021a and 2021b; 2023):

$$\phi_c(^\circ) = 28.3\left(\frac{D_{50}}{D_{\text{ref}}}\right)^{\zeta}(C_U)^{2\zeta}(R)^{-3\zeta} \qquad \text{(Eq. 1.2)}$$

where D_{ref} = reference particle size (= 1 mm), C_U = coefficient of uniformity, R = particle roundness (Wadell, 1932, 1933), and ζ = exponent (= 0.045). Equation 1.2 is applicable for poorly graded, clean silica sands with D_{50} = 0.15–2.68 mm, C_U = 1.2–3.1, and R = 0.3–0.8.

The coefficient of lateral earth pressure at-rest $K_{0,\text{NC}}$ for a normally consolidated (NC) sand typically ranges from 0.4–0.5, with lower values corresponding to dense sand and higher values corresponding to loose sand (Salgado & Prezzi, 2007). For an overconsolidated (OC) sand, $K_{0,OC} \approx K_{0,NC}\sqrt{\text{OCR}}$ (Brooker & Ireland, 1965); where the overconsolidation ratio (OCR) may be evaluated based on the geologic history of the site (Niazi, 2021; Sakleshpur et al., 2021a).

1.2.2 Interpretation of CPT Results in Clay

In general, drained loading governs the shear strength of sandy soils, and undrained loading governs the shear strength of clayey soils. The undrained shear strength s_u of clay may be determined directly from the results of field vane shear tests, unconfined compression tests, and/or unconsolidated- or consolidated-undrained (UU or CU) triaxial compression tests. Alternatively, the value of s_u may be estimated indirectly from CPT results using (Dagger et al., 2018; Lunne et al., 1997; Mayne, 2007; Robertson, 2009; Salgado, 2022):

$$s_u = \frac{q_t - \sigma_v}{N_k} \qquad \text{(Eq. 1.3)}$$

where q_t = corrected, total cone resistance measured under undrained conditions (Kim et al., 2008;

Salgado & Prezzi, 2014), σ_v = *in situ* vertical total stress at the depth of interest, and N_k = cone factor.

Salgado (2022) found that the values of N_k reported in the literature range from 8.5 to 24.5, but most lie within the 9–15 range, with outliers possibly due to experimental error or partially drained penetration of the CPT probe. Soft NC clays generally have N_k values near the low end of the 9–15 range, whereas stiff OC clays typically have N_k values near the high end of this range (Mayne & Peuchen, 2018, 2022; Niazi, 2021; Salgado, 2013, 2014; Salgado et al., 2004). Kim et al. (2008, 2006) performed cone penetration tests in layers of NC-to-lightly-OC silty clay [$q_t \approx 0.65$–0.8 MPa (6.8–8.3 tsf) and OCR $\approx$ 1.0–1.2] at SR 18 in Carroll County, and in a layer of OC silty clay [$q_t \approx 1.5$ MPa (15.7 tsf) and OCR = 4.9] at SR 49 in Jasper County. The undrained shear strength s_u of the silty clay layers was determined from the results of isotropically-consolidated undrained triaxial compression (CIUC) tests, and the value of N_k was found to be of the order of 9–10 for the Carroll County site and 14 for the Jasper County site (Kim et al., 2009; Seo et al., 2009). The cone factor N_k also depends on the stress paths that soil elements experience near an advancing cone. Bisht et al. (2021, 2024) performed simulations of cone penetration in overconsolidated Boston Blue Clay (OCR = 2.2–4.3) using the material point method (MPM) and found that the value of N_k is in the range of 12.2–13.3 for undrained triaxial compression (UDTXC), 13.2–14.6 for undrained simple shear (UDSS), and 17.6–19.2 for undrained triaxial extension (UDTXE).

1.3 MSE Wall External and Internal Stability Assessment

1.3.1 External Stability

Current INDOT Standard Specifications (INDOT, 2024) require that MSE walls be designed in accordance with the *AASHTO LRFD Bridge Design Specification* (AASHTO, 2020). The AASHTO LRFD methodology for MSE walls requires assuming that MSE wall reinforced soil masses are rigid bodies akin to conventional reinforced-concrete (gravity) retaining walls. As a result, MSE walls must be checked for external stability. External stability design checks include foundation bearing resistance, sliding resistance along the foundation, MSE wall overturning resistance, and global (overall) stability, which is checked separately using a limit equilibrium-based slope stability analysis program. For convenience in notation, the subscripts *rf*, *rt*, and *fn* are used hereafter to indicate that the corresponding soil variables (e.g., unit weight γ and friction angle ϕ) are related to the reinforced fill, the retained backfill, and the foundation soil, respectively.

1.3.2 Sliding Limit State

The external lateral load on an MSE wall must not exceed the sliding resistance of the MSE wall foundation. The load and resistance factor design (LRFD) inequality for the sliding limit state for an MSE wall is (AASHTO, 2020; FHWA, 2009a; Kim & Salgado, 2012a; Salgado, 2022):

Sandy foundation soil:

$$RF(W_{rf} \tan\delta) \geq LF_{EA1}E_{A1} + LF_{EA2}E_{A2}$$

Clayey foundation soil:

$$RF[\min\ (s_u L_r;\ 0.5\sigma'_v L_r)] \geq LF_{EA1}E_{A1} + LF_{EA2}E_{A2} \quad \text{(Eq. 1.4)}$$

where RF = resistance factor, s_u = undrained shear strength of clay near the MSE wall foundation interface, σ'_v [= $\gamma_{rf}H$] = vertical (normal) effective stress acting on the MSE wall foundation interface, W_{rf} [= $\gamma_{rf}HL_r$] = weight of the reinforced fill (per unit length of wall); γ_{rf} = unit weight of the reinforced fill; H = MSE wall height (measured from the top of the leveling pad to the top of the reinforced fill); L_r = reinforcement length; δ = interface friction angle at the base of the MSE wall (= min [$\phi_{p,rf}$;$\phi_{p,fn}$]); $\phi_{p,rf}$ and $\phi_{p,fn}$ = peak friction angles of the reinforced fill and foundation soil; E_{A1} [= $0.5K_A\gamma_{rt}H^2$] and E_{A2} [=$K_A q_{0,rt}H$] = horizontal forces (per unit length of wall) due to the active earth pressures caused by the weight of the retained backfill and any live uniform surcharge load $q_{0,rt}$ acting on top of the retained backfill, respectively; K_A = active earth pressure coefficient of the retained backfill; γ_{rt} = unit weight of the retained backfill; and LF_{EA1} and LF_{EA2} = load factors corresponding to horizontal forces E_{A1} and E_{A2}. The values of LF_{EA1} and LF_{EA2} specified by AASHTO (2020) are 1.50 and 1.75. These load factors correspond to the strength I limit state (basic load combination relating to the normal vehicular use of the bridge without wind), as defined by AASHTO (2020).

According to AASHTO (2020), the value of K_A is calculated using the formulation of Coulomb (1776):

$$K_A = \frac{\sin^2\ (\phi_{p,rt} + \beta_w)}{\sin^2\beta_w \sin\ (\beta_w - \delta)\left[1 + \sqrt{\dfrac{\sin\ (\phi_{p,rt} + \delta)\ \sin\ (\phi_{p,rt} - \alpha_g)}{\sin\ (\beta_w - \delta)\ \sin\ (\alpha_g + \beta_w)}}\right]^2} \quad \text{(Eq. 1.5)}$$

where δ = interface friction angle between the reinforced fill and the retained backfill (= min [$0.67\phi_{p,rf}$; $0.67\phi_{p,rt}$]), $\phi_{p,rf}$ and $\phi_{p,rt}$ = peak friction angles of the reinforced fill and retained backfill, α_g = inclination of the retained backfill surface with the horizontal, and β_w = inclination of the back face of the reinforced fill with the horizontal. For an MSE wall with a horizontal backfill surface, $\alpha_g = 0^\circ$ and $\beta_w = 90^\circ$, and, consequently, Equation 1.5 reduces to (AASHTO, 2020):

$$K_A = \frac{\cos^2\phi_{p,rt}}{\cos\ \delta\left[1 + \sqrt{\dfrac{\sin\ (\phi_{p,rt} + \delta)\ \sin\ \phi_{p,rt}}{\cos\delta}}\right]^2} \quad \text{(Eq. 1.6)}$$

In the absence of laboratory shear test results, the values of $\phi_{p,rf}$, $\phi_{p,rt}$, and $\phi_{p,fn}$ are typically set to 34°, 30°, and 30°, respectively (AASHTO, 2020). For MSE walls that are part of bridge substructures (target reliability index $\beta_T = 3.5$), the *RF* values determined by Kim and Salgado (2012a) for the sliding limit state are: 0.80 for H = 5–7.5 m (16–25 ft), 0.90 for H = 7.5–10 m (25–33 ft), and 1.00 for $H \geq 10$ m (33 ft). In proposing these *RF* values as well as those for the overturning limit state check, Kim and Salgado (2012a) suggested that (1) the appropriate friction angle for use in the calculation of the active earth pressure coefficient is the critical-state friction angle ϕ_c, instead of the peak soil friction angle ϕ_p, and (2) the critical-state interface friction angle δ_c at the base of the MSE wall can be calculated as $\tan^{-1}(\sin\phi_c)$. AASHTO (2020) specifies an *RF* value of 1.0 for the sliding limit state regardless of the MSE wall height; the basis for this value is through calibration by fitting to working stress design (WSD).

1.3.3 Overturning Limit State

Although MSE walls are generally too flexible to fail through overturning, MSE walls must still be checked for overturning stability since the AASHTO LRFD procedure models MSE wall reinforced soil masses as rigid bodies. The LRFD inequality for the overturning ultimate limit state for an MSE wall is (Kim & Salgado, 2012a; Salgado, 2022):

$$RF\left[W_{rf}\left(\frac{L_r}{2}\right)\right] \geq LF_{EA1}E_{A1}\left(\frac{H}{3}\right) + LF_{EA2}E_{A2}\left(\frac{H}{2}\right) \quad \text{(Eq. 1.7)}$$

where all the terms have been defined previously for the sliding limit state. The *RF* values determined by Kim and Salgado (2012a) for the overturning limit state (for $\beta_T = 3.5$) are: 0.75 for H = 5–7.5 m (16–25 ft), 0.80 for H = 7.5–12.5 m (25–41 ft), and 1.00 for H ≥ 12.5 m (41 ft). FHWA (2009a) and AASHTO (2020) do not specify a resistance factor for the overturning limit state, but instead follow a different approach, as outlined below.

FHWA (2009a) and AASHTO (2020) indirectly satisfy the overturning check by limiting the load eccentricity at the base of the MSE wall. In the eccentricity check, the live uniform surcharge load $q_{0,rf}$ acting on top of the reinforced fill and the weight of the wall facing are neglected; however, the live uniform surcharge load $q_{0,rt}$ acting on top of the retained backfill is considered in the analysis as it contributes to the horizontal force E_{A2}. The eccentricity e is calculated using factored loads (AASHTO, 2020; FHWA, 2009a):

$$e = \frac{LF_{EA1}E_{A1}\left(\frac{H}{3}\right) + LF_{EA2}E_{A2}\left(\frac{H}{2}\right)}{LF_{DL}W_{rf}} \quad \text{(Eq. 1.8)}$$

where most of the terms have been defined previously, except for LF_{DL} [= 1.00], which is the load factor corresponding to the self-weight (dead load) W_{rf} of the reinforced fill. According to AASHTO (2020), the eccentricity check is satisfied if $e < L_r/3$, i.e., if the location of the resultant vertical force (calculated based on factored loads) acting on the MSE wall base lies within the middle two-thirds of the wall base width.

1.3.4 Bearing Capacity Limit State

The MSE wall bearing stress (i.e., the total vertical load per unit wall length divided by the effective wall width) must not exceed the bearing resistance of the MSE wall foundation. The LRFD inequality for the bearing capacity limit state for an MSE wall is (AASHTO, 2020; FHWA, 2009a; Salgado, 2022):

$$RF(R_n) \geq LF_{DL}W_{rf} + LF_{LL}q_{0,rf}L_r \quad \text{(Eq. 1.9)}$$

where RF [= 0.65] = resistance factor, R_n [= $q_{bL}B_{\text{eff}}$] = nominal bearing resistance of the MSE wall foundation (per unit length of wall), q_{bL} = nominal limit unit bearing capacity of the MSE wall foundation, B_{eff} [= $B - 2e_B$] = effective width of the MSE wall foundation, B = actual width of the MSE wall foundation (≈ L_r, the reinforcement length), W_{rf} = self-weight (dead load) of the reinforced fill (per unit length of wall), $q_{0,rf}L_r$ = live (vehicular) load on top of the reinforced fill (per unit length of wall), LF_{DL} [= 1.35] and LF_{LL} [= 1.75] = load factors corresponding to W_{rf} and $q_{0,rf}L_r$, and e_B = load eccentricity, given by (AASHTO, 2020; FHWA, 2009a):

$$e_B = \frac{LF_{EA1}E_{A1}\left(\frac{H}{3}\right) + LF_{EA2}E_{A2}\left(\frac{H}{2}\right)}{LF_{DL}W_{rf} + LF_{LL}q_{0,rf}L_r} \quad \text{(Eq. 1.10)}$$

where load factors LF_{EA1} and LF_{EA2} are equal to 1.50 and 1.75.

The limit unit bearing capacity of MSE wall foundations in sandy soils (neglecting the c and q terms of the general bearing capacity equation) is given by (AASHTO, 2020; FHWA 2009a):

$$q_{bL} = \frac{1}{2}\gamma_{fn}B_{\text{eff}}N_\gamma C_{w\gamma} \quad \text{(Eq. 1.11)}$$

where γ_{fn} = unit weight of the foundation soil, $C_{w\gamma}$ = water table correction factor (AASHTO, 2020), and N_γ = bearing capacity factor (Caquot & Kerisel, 1953; Reissner, 1924; Vesic, 1973):

$$N_\gamma = 2(N_q + 1)\tan\phi_{p,fn} \quad \text{(Eq. 1.12)}$$

$$N_q = \left(\frac{1 + \sin\phi_{p,fn}}{1 - \sin\phi_{p,fn}}\right)\exp(\pi\tan\phi_{p,fn}) \quad \text{(Eq. 1.13)}$$

where $\phi_{p,fn}$ = representative peak friction angle of the foundation soil. Equations 1.12 and 1.13 are valid only for materials that follow the Mohr-Coulomb yield criterion with an associated flow rule [dilatancy angle ψ equal to the friction angle ϕ] (Lyamin et al., 2007).

Real sands, however, follow a non-associated flow rule ($\psi < \phi$) (Janabi et al., 2023; Loukidis & Salgado, 2009a, 2011; Yin et al., 2001). The limit unit bearing capacity of a strip footing in sand calculated based on the assumption of an associated flow rule is about 30% to 37% greater than that obtained considering flow rule non-associativity (Raja et al., 2024; Salgado, 2020, 2024).

The limit unit bearing capacity of MSE wall foundations in clayey soils (neglecting the q and γ terms of the general bearing capacity equation) is given by (AASHTO, 2020; FHWA, 2009a):

$$q_{bL} = s_u N_c \qquad \text{(Eq. 1.14)}$$

where s_u = representative undrained shear strength of clay within the influence depth of the MSE wall foundation, and N_c = bearing capacity factor (= 5.14, for $\phi_{p,fn} = 0$). According to AASHTO (2020), Equations 1.11 and 1.14 are valid only for a "general shear" type of mechanism; for "local shear" and "punching shear" type mechanisms, the modified shear strength parameters s_u^* and $\phi^*_{p,fn}$ for use in the above equations are given by: $s_u^* = 0.67 s_u$ and $\phi^*_{p,fn} = \tan^{-1}(0.67\tan\phi_{p,fn})$.

1.3.5 Internal Stability

The process for internal stability design of an MSE wall consists of determining the magnitude and location of the maximum tensile force in each reinforcement layer and the corresponding resistance provided by the reinforcement against rupture, pullout, and facing connection failure (Kim & Salgado, 2008). Although several reinforcement types (e.g., steel strips, steel grids, geotextile sheets, and geogrids) are used in MSE wall construction, the focus of this report is on steel strips.

Maximum tensile load $\mathbf{T_{max}}$. The maximum tensile load $T_{\max}$ that develops in a given reinforcement layer is due to the lateral effective stress σ'_h (= $K_r\sigma'_v$) acting on the back of the wall facing over the tributary area of the reinforcement (Bathurst, 2014; Kim & Salgado, 2012b; Salgado, 2022). To calculate $T_{\max}$ (in units of force per unit length of wall in the longitudinal direction) for a given reinforcement layer located at depth z from the top of an MSE wall, the vertical effective stress σ'_v at that depth is multiplied by the lateral earth pressure coefficient K_r and the tributary vertical spacing s_v of the reinforcement (AASHTO, 2012; FHWA, 2009a). The tributary vertical spacing s_v is the distance between the midpoints of vertically adjacent reinforcement layers, except for the topmost and bottommost reinforcement layers. For the topmost reinforcement layer, s_v is the distance from the top of the reinforced fill (for a level backfill surface) to the midpoint between the first and second layers of reinforcement counted from the top of the wall, whereas for the bottommost reinforcement layer, s_v is the distance from the top of the leveling pad to the midpoint between the first and second layers of reinforcement counted from the bottom of the wall (AASHTO, 2020; FHWA, 2009a).

Several methods have been developed to calculate the maximum tensile load $T_{\max}$ for steel strip-reinforced MSE walls (Table 1.1): the coherent gravity method (AASHTO, 2020; Anderson et al., 2010; Bathurst et al., 2008; Juran & Schlosser, 1978; Schlosser, 1978; Schlosser & Segrestin, 1979); the Federal Highway Administration (FHWA) structure stiffness method (Christopher, 1993; Christopher et al., 1990); and the simplified method (AASHTO, 2020; Allen et al., 2001; Bathurst et al., 2009). All these methods are essentially variants of the traditional (limit equilibrium) tieback wedge method but have been empirically adjusted so that the predicted maximum reinforcement tensile loads are in better agreement with those measured in available full-scale, instrumented MSE walls under initial operational (working stress) conditions. Current practice for estimation of reinforcement loads in the United States is based on the coherent gravity method for inextensible-(steel)-reinforced MSE walls and the simplified stiffness method (Allen & Bathurst, 2015, 2018), which is an updated version of the simplified method, for extensible-(geosynthetic)-reinforced MSE walls. The simplified method is an acceptable alternative for both steel- and geosynthetic-reinforced wall systems (AASHTO, 2020).

1.3.6 Rupture Limit State

The LRFD inequality for the reinforcement rupture limit state for an MSE wall is (AASHTO, 2020; FHWA, 2009a):

$$RF(R_{SF}R_C) \geq LF_{DL}T_{\max,DL} + LF_{LL}T_{\max,LL} \qquad \text{(Eq. 1.15)}$$

where $T_{\max,DL}$ [= $K_r(\gamma_{rf}z)s_v$] = maximum tensile force in the reinforcement (per unit length of wall) due to the lateral earth pressure caused by the self-weight (dead load) of the reinforced fill, K_r = lateral earth pressure coefficient, γ_{rf} = unit weight of the reinforced fill, z = vertical distance from the top of the reinforced fill to the reinforcement layer of interest, s_v = tributary vertical spacing of the reinforcement, s_h = horizontal spacing of the reinforcement, $T_{\max,LL}$ [= $K_r(q_{0,rf})s_v$] = maximum tensile force in the reinforcement (per unit length of wall) due to the lateral earth pressure caused by the live uniform surcharge load $q_{0,rf}$ acting on top of the reinforced fill, LF_{DL} [=1.35] and LF_{LL} [=1.75] = load factors corresponding to forces $T_{\max,DL}$ and $T_{\max,LL}$, RF [=0.75] = resistance factor, R_c [=b/s_h] = reinforcement coverage ratio, R_{SF} [=$f_y A_c/b$] = nominal resistance of the reinforcement against rupture, f_y = yield strength of the reinforcement [usually 65 ksi (450 MPa) for grade 65 steel], and A_c = cross-sectional area of the reinforcement corrected for corrosion loss (AASHTO 2020; FHWA 2009a):

$$A_c = bt_{LT} = b(t_n - t_R) \qquad \text{(Eq. 1.16)}$$

TABLE 1.1
Methods for estimation of K_r and T_{max} for internal stability design of steel strip-reinforced MSE walls

Reference	Equation	Comments
Coherent Gravity Method (AASHTO, 2020)	$T_{max} = K_r \sigma'_v s_v = K_r \left(\frac{\gamma_{rf} z L_r}{L_r - 2e}\right) s_v$ $K_r = \begin{cases} K_0 - \left(\frac{K_0 - K_A}{20}\right) z \text{ for } 0 \le z < 20 \text{ ft} \\ K_A \text{ for } z \ge 20 \text{ ft} \end{cases}$	In the coherent gravity method, K_r decreases linearly from K_0 at the top of the wall to K_A at a depth of 20 ft and remains constant at K_A thereafter. The vertical effective stress σ'_v acting at each reinforcement level is calculated based on Meyerhof (1953) considering the load eccentricity e due to the lateral earth pressure exerted by the retained backfill on the reinforced fill at the elevation of the reinforcement layer.
Simplified Method (AASHTO, 2020)	$T_{max} = K_r \sigma'_v s_v = K_r \gamma_{rf} z s_v$ $\frac{K_r}{K_A} = \begin{cases} 1.7 - \frac{z}{40} \text{ for } 0 \le z < 20 \text{ ft} \\ 1.2 \text{ for } z \ge 20 \text{ ft} \end{cases}$	In the simplified method, K_r decreases linearly from $1.7K_A$ at the top of the wall to $1.2K_A$ at a depth of 20 ft and remains constant at $1.2K_A$ thereafter. The method provides different empirically derived K_r/K_A profiles depending on the reinforcement type and material.
Simplified Stiffness Method (Allen & Bathurst, 2015)	$T_{max} = K_A (\gamma_{rf} H D_{t\,max}) s_v \Phi_g \Phi_{fs}$ $D_{tmax} = \begin{cases} D_{t\,max\,0} + (z/z_b)(1 - D_{t\,max\,0}) \text{ for } z < z_b \\ 1.0 \text{ for } z \ge z_b \end{cases}$ $\Phi_g = \alpha (S_{global}/p_A)^{\beta}$ $\Phi_{fs} = \min\left\{\eta \left(S_{global}/p_A\right) F_f^{\ k}; 1.0\right\}$ $z_b = C_h H^y \Phi_{fs}$ $F_f = \frac{1.5 H^3 p_A}{E b^3 (h_{eff}/H)}$	The simplified stiffness method was developed on the basis that the maximum tensile loads in reinforcement layers under operational conditions are a function of reinforcement stiffness and not the strength of the reinforcement. The T_{max} equation presented here is for the case of a non-surcharged ($q_0 = 0$), vertical MSE wall with steel strip reinforcement and clean, uncemented ($c = 0$), coarse-grained backfill soil. The original equation for T_{max} contains additional terms that account for surcharge, facing batter, backfill soil "cohesion," and local reinforcement stiffness (these terms are not applicable and do not influence the value of T_{max} for the MSE wall investigated in this study). The values of the coefficients and exponents that appear in the equations are as follows: $C_h = 0.40$, $y = 1.2$, $D_{tmax0} = 0.12$, $\alpha = 0.16$, $\beta = 0.26$, $\eta = 0.57$, and $\kappa = 0.15$.

Note: K_0 = At-rest earth pressure coefficient ($=1 - \sin\phi_{p,rf}$), K_A = Rankine active earth pressure coefficient [$= (1 - \sin\phi_{p,rf})/(1 + \sin\phi_{p,rf})$], $\phi_{p,rf}$ = peak friction angle of the reinforced fill (determined from either direct shear or drained triaxial compression test results), γ_{rf} = unit weight of the reinforced fill, σ'_v = vertical effective stress acting on the reinforcement layer located at depth z below the top of the reinforced fill (for a level backfill surface), L_r = reinforcement length, s_v = tributary vertical spacing of the reinforcement layer, D_{tmax} = T_{max} distribution factor that accounts for the nonlinear distribution of reinforcement loads with depth below the top of the wall, Φ_{fb} = facing batter factor (= 1.0 for a vertical wall with wall facing angle $\omega = 0°$), Φ_g = global stiffness factor, Φ_{fs} = facing stiffness factor, p_A = atmospheric pressure [= 101 kPa (1 tsf)], S_{global} = global reinforcement stiffness $\left[= \sum_{i=1}^{n} J_i \ /H\right]$, n = number of reinforcement layers, J = stiffness of the reinforcement layer per unit wall width ($= E_s A_s / s_h$ for steel strip reinforcement), E_s = modulus of steel [typically 200 GPa (29,000 ksi)] determined at a strain level of 0.1%–0.2%, A_s = steel cross-sectional area of the reinforcement at the end of wall construction, s_h = horizontal spacing of the reinforcement, F_f = facing stiffness parameter, b = thickness of the facing column, H = height of the facing column, E = elastic modulus of an "equivalent elastic beam" representing the wall face, and h_{eff} = equivalent height of an unjointed facing column that is 100% efficient in transmitting moment through the height of the facing column (for incremental panel walls, h_{eff} is equal to the height of a facing panel). The methods do not consider the interface friction angle mobilized between the back of the wall facing and the reinforced fill material.

where b = reinforcement width [usually 50 mm (2 in.) for steel strips], t_{LT} = long-term thickness of the reinforcement at the end of the design life, t_n = nominal thickness of the reinforcement at the time of MSE wall construction [usually 4 mm (5/32 in.) for steel strips], and t_R = sacrificial thickness of metal expected to be lost by corrosion during the design life of the structure (AASHTO, 2020; FHWA, 2009a):

$$t_R = 2\dot{c}_r (t_d - t_z) \qquad \text{(Eq. 1.17)}$$

where $\dot{c}_r$ = corrosion rate of carbon steel [= 12 μm (0.47 mils)/year/side], t_d = design life of the structure [typically 75 years for MSE walls and 100 years for MSE bridge abutments (AASHTO, 2020)], and t_z = service life of the galvanization (zinc) coating (= 16 years).

According to AASHTO (2020), for a non-aggressive fill material with pH = 5–10, resistivity ≥ 3,000 ohm-cm, chlorides ≤ 100 ppm, sulfates ≤ 200 ppm, and organic content ≤ 1%, the zinc coating is lost at a rate of 0.58 mil./year/side (15 μm/year/side) for the first 2 years and 0.16 mil./year/side (4 μm/year/side) for subsequent years. Therefore, for a minimum galvanization coating thickness of 3.4 mils (86 μm), the zinc coating will be completely lost in 16 years, and then the base metal (carbon steel) will begin to corrode.

1.3.7 Pullout Limit State

The locus of the maximum reinforcement tensile load T_{max} for MSE walls in working states separates the active zone from the resisting zone; it is typically used

as a proxy for the potential slip surface that would develop within the reinforced fill when the wall reaches an ultimate limit state (AASHTO, 2020; Salgado, 2022). The total length L_r of the reinforcement is the sum of the reinforcement length L_a within the active zone and the reinforcement length L_e within the resisting zone. For inextensible (metallic) reinforced MSE walls, AASHTO (2020) approximates the shape of the potential slip surface as bilinear; L_a increases linearly from a value of zero at the wall base to $0.3H$ at mid-height of the wall and then remains constant at $0.3H$ in the upper half of the wall.

The LRFD inequality for the reinforcement pullout limit state for an MSE wall is (AASHTO, 2020; FHWA, 2009a):

$$RF(R_{PO}R_c) \geq LF_{DL}T_{\max,DL} \qquad \text{(Eq. 1.18)}$$

where most of the terms have been defined previously for the rupture limit state; RF [= 0.90] = resistance factor, and R_{PO} = nominal resistance of the reinforcement against pullout (AASHTO, 2020; FHWA, 2009a):

$$R_{PO} = C_S C_P \mu^*_{\text{ult}} \sigma'_v L_e \qquad \text{(Eq. 1.19)}$$

where C_S = scale effect correction factor (= 1.0 for metallic reinforcements), C_P = reinforcement effective perimeter coefficient (= 2 since friction develops on both sides of the reinforcement), σ'_v [= $\gamma_{rf}z$] = vertical effective stress at the soil-reinforcement interface, L_e = length of the reinforcement in the resisting zone, and μ^*_{ult} = ultimate pullout resistance coefficient, which, for ribbed steel strips, is given by (AASHTO, 2020):

$$\mu^*_{\text{ult}} = \begin{cases} \zeta + \left(\dfrac{\tan\phi_{p,rf} - \zeta}{20}\right) z \text{ for } 0 \leq z < 20 \text{ ft} \\ \tan\phi_{p,rf} \text{ for } z \geq 20 \text{ ft} \end{cases} \qquad \text{(Eq. 1.20)}$$

where ζ = min [1.2 + logC_U; 2.0], and $\phi_{p,rf}$ and C_U = peak friction angle and coefficient of uniformity of the reinforced fill material.

1.4 MSE Wall Foundation QA/QC Methods

A well-compacted foundation bed is essential to prevent excessive settlement (both total and differential settlement) and bearing capacity failure of an MSE wall. Kim et al. (2010) and Ganju et al. (2015) summarized the compaction control specifications adopted by various DOTs in the United States. Approved MSE wall foundation preparation quality assurance methods in Indiana include proof rolling and dynamic cone penetration testing.

1.4.1 Dynamic Cone Penetration Test

The dynamic cone penetration test (DCPT) is a penetration-type *in situ* test used by several DOTs (e.g., Indiana DOT, Iowa DOT, Minnesota DOT, and Ohio DOT) in the United States for quality assurance (QA) and quality control (QC) of soil compaction at shallow depth (NCHRP, 2014). The test involves dropping a 17.6 lb (8 kg) weight from a height of 22.6 in. (57.5 cm) onto a conically tipped rod [cone diameter = 20 mm (0.8 in.) and apex angle = 60°] and measuring the resulting penetration distance (ASTM, 2018a). The results obtained from the DCPT can be interpreted in two ways: (1) the penetration index (PI), which is the penetration of the cone tip into the soil per unit drop of the hammer (in units of in./blow or mm/blow), and (2) the DCPT blow count, which is the number of hammer drops required for the cone tip to penetrate a certain distance into the soil. Salgado and Yoon (2003) and Ganju et al. (2015) summarized the correlations between PI and California Bearing Ratio (CBR) and between PI and subgrade resilient modulus M_R.

The *in situ* dry unit weight γ_d of clayey sand (or sandy loam as per INDOT specifications) can be estimated as a function of the DCPT penetration index using (Salgado & Yoon, 2003):

$$\gamma_d = \gamma_w \quad 10^{1.5} \times \text{PI}^{-0.14} \times \sqrt{\frac{\sigma'_v}{p_A}}^{0.5} \qquad \text{(Eq. 1.21)}$$

where γ_w = unit weight of water [= 9.81 kN/m^3 (62.45 pcf)], PI = penetration index (in mm/blow), σ'_v = vertical effective stress, and p_A = reference stress (= 100 kPa or 1 tsf). Several research studies (Ganju et al., 2018; Kim et al., 2010; Salgado & Yoon, 2003) have also demonstrated that the DCPT blow count correlates with relative compaction (RC), which is the ratio of the dry density ρ_d achieved in the field to the maximum dry density $\rho_{d,\max}$ obtained from a laboratory Proctor compaction test.

Based on the results of 760 DCPTs performed on compacted subgrades and embankments in Indiana along with the results of 76 field sand cone tests, *in situ* water content measurements, and laboratory tests, Ganju et al. (2018) found that the DCPT blow count N_{DCPT} for 0–12 in. (0−30 cm) penetration correlates well with the standard Proctor optimum water content wc_{opt} for coarse-grained soils compacted to 95% relative compaction:

$$N_{\text{DCPT}} = 0.17wc^2_{\text{opt}} - 5.94wc_{\text{opt}} + 59.54 \qquad \text{(Eq. 1.22)}$$

and with the coefficient of uniformity C_U for compacted INDOT structure backfill materials and clean sands (RC = 95%):

$$N_{\text{DCPT}} = 4.03\ln(C_U) + 2.64 \qquad \text{(Eq. 1.23)}$$

For fine-grained soils compacted to 95% relative compaction, the DCPT blow count N_{DCPT} for both 0–6 in. (0−15 cm) and 6–12 in. (15−30 cm) penetration correlates well with the plasticity index I_P of the soil (Ganju et al., 2018):

$$N_{\text{DCPT}} = 13.03e^{-0.222I_P} + 8.05e^{-0.00483I_P} \qquad \text{(Eq. 1.24)}$$

for 0–6 in. (0−15 cm) penetration, and

$$N_{\mathrm{DCPT}} = 22.11e^{-0.234I_P} + 13.04e^{-0.0117I_P} \quad \text{(Eq. 1.25)}$$

for 6–12 in. (15–30 cm) penetration. Equations 1.22–1.25 correspond to $R^2 \geq 0.95$ and are applicable for values of wc_{opt} in the range of 8%–13%, C_U ranging from 3 to 6, and plasticity index equal to or greater than 8%.

Boutet et al. (2011), based on the results of field vane shear tests and DCPTs performed at ten sites in the province of Quebec, Canada, proposed the following relationship between the DCPT penetration index and the undrained shear strength of fine-grained soils:

$$\log s_u = a_0 \times (I_P \times \rho_d^{0.5})^{0.5} \times \log \mathrm{PI} + 2.39 + a_1 \quad \text{(Eq. 1.26)}$$

where s_u = undrained shear strength (in kPa), I_p = plasticity index (in percent), ρ_d = dry density (in g/cm^3), PI = penetration index (in mm/blow), and the coefficient of determination R^2 is equal to 0.95. The values of a_0 and a_1 are −0.20 and 1.51 for soils classified as CH (inorganic clays with high plasticity) according to the Unified Soil Classification System (USCS) and −0.10 and 0 for both CL (inorganic clays with low to medium plasticity) and ML-CL soils (clayey silts and silty clays). The DCPT and field vane shear tests were performed at shallow depths ranging from 20 cm (8 in.) to 60 cm (24 in.) below the ground surface. The fines content, liquid limit, and plasticity index of the tested fine-grained soils ranged from 62%−99%, 20%−60%, and 7%−36%, with higher values corresponding to the CH soils.

INDOT Construction Memorandum 15–08 (Miller, 2015) provides a relationship between the DCPT blow count and the factored bearing resistance of MSE wall foundations constructed over fine-grained soils (Table 1.2). This relationship was inferred from combining a DCPT blow count to California Bearing Ratio (CBR) correlation (ASTM, 2018a) with a separate CBR to unconfined compressive strength correlation (Christopher et al., 2006) and then calculating the factored bearing resistance per AASHTO LRFD (AASHTO, 2020). In addition, this relationship was intended to replace the 5 blows per 6 in. acceptance criteria (i.e., a minimum DCPT blow count of 5 for every 6-in. penetration increment until a total penetration of 30 in. is achieved) used by INDOT for verification of foundation soil compaction prior to construction of the MSE wall. For example, if the factored bearing pressure (or factored unit load) at the base of the MSE wall foundation reported on the contractor's working drawing is 5,900 psf (282 kPa), the DCPT blow count for 12 inches (305 mm) of penetration would need to be at least 16 for a total penetration of 30 in. (762 mm) (i.e., 16 blows for each of the first two 12-in. increments and 8 blows for the last 6-in. increment) prior to construction of the MSE wall—this would then correspond to a factored bearing resistance (or factored unit bearing capacity) of 6,000 psf (287 kPa) (Miller, 2015).

TABLE 1.2
INDOT construction verification chart for factored bearing resistance based on DCPT blow counts (Miller, 2015)

DCPT Blow Count for 12-in. Penetration	Factored Bearing Resistance (psf)
10	4,000
11	4,300
12	4,600
13	5,000
14	5,300
15	5,600
16	6,000
17	6,300
18	6,600
19	7,000
20	7,300
21	7,600
22	8,000
23	8,300
24	8,600
25	9,000
26	9,300
27	9,600
28	10,000
29	10,300
30	10,600
31	11,000

Note: This table is applicable only for fine-grained soils.

1.5 Report Structure

The report has been organized into six chapters. Chapter 1 provides an introduction to MSE walls and bridge abutments, including subsurface exploration protocols for MSE walls, interpretation of CPT results in sand and clay, MSE wall external and internal stability assessment, and QA/QC methods for MSE wall foundations.

Chapter 2 presents the details of the Whitestown Parkway Bridge, and the results of the site investigation carried out prior to construction of Bent 3. The depth profiles of SPT blow count N_{60}, CPT cone resistance q_t, particle size content, Atterberg limits, and colloidal activity, along with the classification of the soil layers are reported in this chapter. The results of direct shear tests performed on the reinforced fill material, surface roughness tests performed on a sample of the steel strip, and uniaxial load-compression test results for the bearing pad are also presented. In addition, the chapter details the construction timeline and instrumentation (sensor layout, installation and protection) of the MSE bridge abutment. The instrumentation consists of earth pressure cells, strain gauges, inclinometers, and crackmeters, while the data acquisition system consists of dataloggers, multiplexers, and solar panels. The chapter concludes with the test procedure and loading protocol for a live load test performed on the bridge using twelve triaxle dump trucks fully loaded with coarse aggregate material.

Chapter 3 presents the instrumentation and monitoring data collected during construction of the MSE

wall. The results include the vertical stresses at the base of the leveling pad and within the backfill soil, the lateral stresses on the back of the wall facing, the tensile loads in the reinforcement, the lateral deflection of the wall facing, the contraction of the panel joints, and the settlement of the MSE wall foundation. The measured lateral stresses and reinforcement tensile loads at the end of wall construction were compared with predictions obtained using design methods specified in AASHTO (2020) for backfill soil friction angles ranging from 32° to 40°.

Chapter 4 presents the instrumentation and monitoring data collected during and after construction of the bridge on top of the MSE wall as well as during the live load test performed on the bridge post-construction. The results include the dead and live loads carried by the piles and pile cap, the vertical and lateral stresses within the MSE abutment, the magnitude and distribution of the tensile loads in the steel strip reinforcements, the vertical and lateral displacement profiles of the MSE abutment, and the horizontal and vertical joint gap widths between the facing panels.

Chapter 5 presents the results of DCPTs performed in the foundation soil prior to wall construction and in compacted B-borrow material near the pressure cells at the base of the MSE wall foundation. The results include the depth profiles of the cumulative DCPT blow count and penetration index, along with the values of DCPT blow count for 0–12 in. (0–0.3 m), 12–24 in. (0.3–0.6 m), and 24–28 in. (0.6–0.7 m) penetration depths. The DCPT-based factored bearing resistance of the MSE wall foundation obtained using the chart in *INDOT Construction Memorandum 15–08* was compared with the factored bearing pressure specified in the contractor's working drawing as well as with the factored bearing resistance derived from the geotechnical report and specified in the project contract documents. The chapter concludes with a preliminary procedure developed to estimate the unfactored (limit) bearing resistance of the leveling pad in compacted B-borrow material as a function of the pad width and the DCPT blow count for 0–12 in. (0–0.3 m) penetration. The procedure relies mainly on (1) the relationship between the DCPT blow count, coefficient of uniformity C_U, and relative compaction RC developed by Ganju et al. (2018), which is subsequently used to calculate relative density D_R and unit weight γ of the B-borrow material, (2) the Bolton (1986) correlation for calculation of peak friction angle ϕ_p based on critical-state soil mechanics and dilatancy, and (3) the Loukidis and Salgado (2009a) expressions for the bearing capacity factors N_q and N_γ accounting for flow rule non-associativity. Chapter 6 summarizes the key findings and conclusions of the report.

2. WHITESTOWN PARKWAY BRIDGE

2.1 Project Details

The Whitestown Parkway Bridge over Interstate I-65 in Perry Township, Boone County, Indiana (longitude = 86°22′12″W and latitude = 39°57′38″N), is a two-span, prestressed concrete beam bridge; the length of each span is 102.25 ft (31.2 m), and the width of the bridge is 94.3 ft (28.8 m). The eastbound and westbound decks of the bridge are 31.7 ft (9.7 m) and 44.7 ft (13.6 m) wide and consist of two and three traffic lanes, respectively. A 12-ft-(3.7-m)-wide pedestrian walkway lies between the eastbound and westbound decks of the bridge. The bridge deck is supported by nine prestressed concrete bulb-tee beams [spaced 10.75 ft (3.3 m) center-to-center], which, in turn, are supported by two end-bents (Bent 1 and Bent 3) and one interior pier (Pier 2). The beams have top and bottom flange widths of 4.1 ft (1.25 m) and 3.3 ft (1.0 m), a section depth of 4 ft (1.2 m), a flange thickness of 5.5 in. (0.14 m), and a web thickness of 8 in. (0.2 m). Pier 2 consists of six reinforced concrete columns, each supported by nine steel H-piles (HP 12×74) arranged in a 3×3 group configuration. Both Bent 1 and Bent 3 are integral, pile-supported MSE bridge abutments with coarse-grained backfill soil, galvanized ribbed steel strip reinforcement, and rectangular precast concrete facing panels. The bridge beams in Bent 1 and Bent 3 are supported by a reinforced concrete pile cap [with length = 135 ft (41.1 m), and width and height = 4 ft (1.2 m)], which, in turn, is supported by a row of 19 steel H-piles [HP 12×74, ASTM A572 grade 50 steel (ASTM, 2018b)] spaced 7 ft (2.1 m) center-to-center. Each H-pile has a flange width of 12.2 in. (310 mm), a section depth of 12.1 in. (308 mm), and flange and web thicknesses of 0.61 in. (15.5 mm).

A zone near the middle of the 223.4-ft-(68.1-m)-long Bent 3 was selected for instrumentation and monitoring (Figure 2.1). The instrumented zone of Bent 3 is 25.3-ft (7.7-m) tall, measured from the top of the leveling pad to the top of the bridge deck, and consists of four levels of rectangular, precast concrete facing panels: a half panel (panel 1 at the bottom of the wall) with a height of 2.40 ft (0.73 m), followed by three levels of full panels (panels 2, 3, and 4) with a height of 4.85 ft (1.48 m) each (Figure 2.2). Both the half and full panels are 9.77 ft (2.98 m) long and 5.5 in. (140 mm) thick, with a minimum 28-day compressive strength of concrete equal to 4,000 psi (27.6 MPa) (RECo, 2025). The half panels have four tie strips, which are cast into the back of the panel during fabrication, whereas the full panels have eight embedded tie strips (four in each row) protruding outwards from the back of the panel.

2.2 Site Investigation

2.2.1 In Situ Testing

Five SPT borings (using an automatic trip hammer) and four CPT soundings (using a CPT truck) were performed at various distances ranging from 4.6–52.5 ft (1.4–16 m) from the instrumented zone of Bent 3, as shown in Figure 2.3. Borings SPT-1 and SPT-2 were performed on September 21st, 2021, whereas borings SPT-3 to SPT-5 were performed on May 9th, 2018.

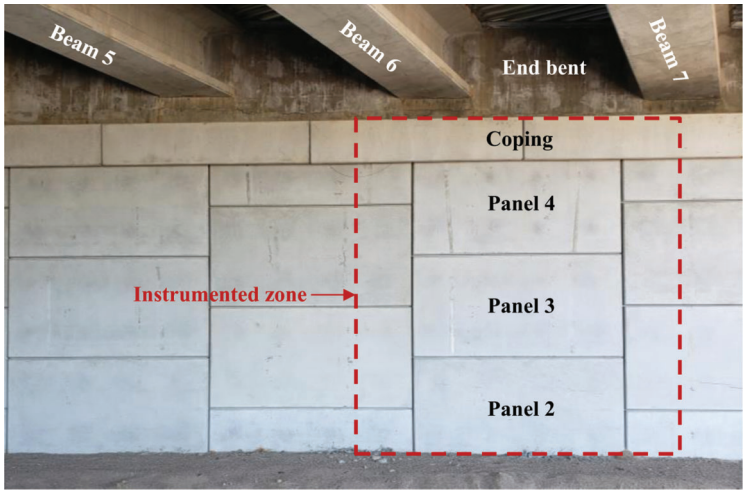

Figure 2.1 Photograph of the instrumented zone of Bent 3 of the Whitestown Parkway Bridge.

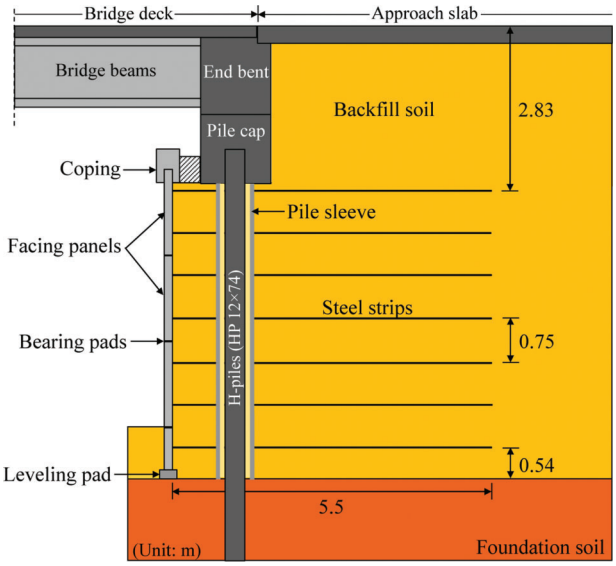

Figure 2.2 Schematic of the cross section of Bent 3 of the Whitestown Parkway Bridge.

Similarly, soundings CPT-1 to CPT-4 were performed on September 22nd, 2021, whereas sounding CPT-5 was performed on November 1st, 2021. The footprint of the MSE abutment lies within a ditch between the shoulder of Perry Worth (PW) Road [corresponding to reduced level (RL) ≈ 929.4 ft (283.3 m)] and the shoulder of the northbound I-65 to Chicago [RL ≈ 933.6 ft (284.6 m)].

Figure 2.4 shows the soil profile [with the soil layers classified according to both the USCS (ASTM, 2017) and AASHTO classification systems (AASHTO, 2008)] and the results of *in situ* and laboratory tests (including Atterberg limits and sieve and hydrometer analyses). The soil profile at the site consists of a top 2.4-m-(8-ft)-thick layer of soft silty clay with low penetration resistance [$N_{60} \approx 4$–10 and $q_t \approx 0.3$–1.0 MPa (3–10 tsf)] and high fines content (= 90%, split equally between silt and clay) and plasticity (liquid limit LL = 50% and plasticity index PI = 25%). This layer is underlain by stiff clayey sandy silt [$N_{60} \approx 20$–30 and $q_{t,\text{avg}} = 5$ MPa (52 tsf)] with low clay content (= 14%) and low plasticity (LL = 18% and PI = 7%). The colloidal activity, as defined by Skempton (1953), of the fine-grained soil layers at the site ranges from 0.45 to 0.55, values that are consistent with the kaolinite group of clay minerals commonly found in soil deposits in Indiana. A 1.8-m-(6-ft)-thick layer of non-plastic, medium-dense-to-dense sand with silt and gravel was found at a depth of 9.1 m (30 ft) below the leveling pad; the penetration resistance of this layer is high [$N_{60} \approx 60$ and $q_{t,\text{avg}} = 40$ MPa (418 tsf)], likely due to the presence of gravel-sized particles in the layer (gravel content = 32% and $D_{50} = 2.1$ mm). The water table was located at the top of this sand-gravel layer according to the SPT boring logs. All SPT borings and CPT soundings were terminated at a depth of about 16 m (52 ft) below the leveling pad, except for boring SPT-5; the data from this boring indicates that the subsequent soil layers also consist of dense silty sand with gravel and stiff clayey sandy silt.

2.2.2 Laboratory Testing

Fill materials. Figure 2.5 shows the particle-size distribution curves of the reinforced fill, the retained backfill, and the embankment soil that is behind the retained backfill; these materials are termed "Type 3 structure backfill," "B-borrow," and "Borrow," respectively, as per INDOT Standard Specifications (INDOT, 2024). The reinforced fill consists of poorly graded (SP), quartz sand (AASHTO classification = A-1-b) with particle sizes D_{10}, D_{30}, D_{50}, and D_{60} equal to 0.22 mm, 0.35 mm, 0.57 mm, and 0.74 mm. The retained backfill also consists of poorly graded (SP), quartz sand (AASHTO classification = A-3) but with D_{10}, D_{30}, D_{50}, and D_{60} equal to 0.18 mm, 0.28 mm, 0.40 mm, and 0.53 mm. The coefficient of uniformity C_U and the coefficient of curvature C_C are equal to 3.45 and 0.78

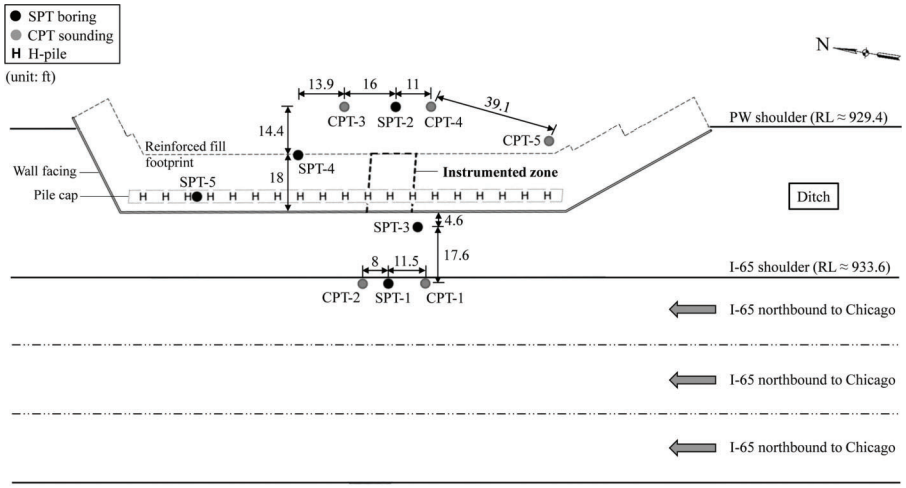

Figure 2.3 Plan view of Bent 3 of the Whitestown Parkway Bridge showing the layout of the SPT borings and CPT soundings.

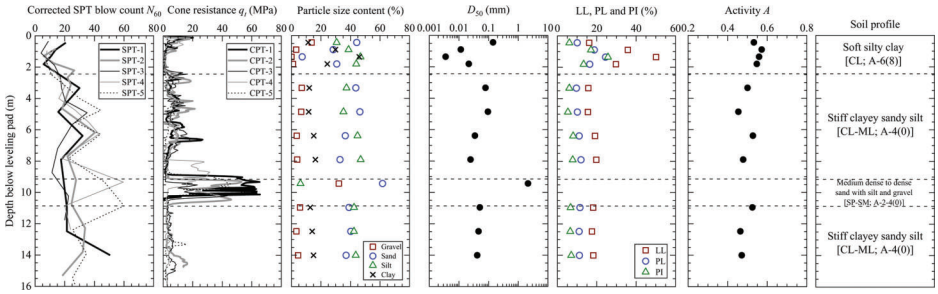

Figure 2.4 Soil profile and results of *in situ* and laboratory tests for Bent 3 of the Whitestown Parkway Bridge.

for the reinforced fill and 3.02 and 0.86 for the retained backfill; the fines content (material passing the US #200 sieve) is less than 1% for both these materials. The minimum and maximum void ratios e_{min} and e_{max} are equal to 0.38 and 0.57 for the reinforced fill and 0.41 and 0.60 for the retained backfill. In contrast, the embankment soil consists of silty sand [AASHTO classification = A-2–4(0)] with 12% gravel, 51% sand, 30% silt, and 7% clay. The liquid limit (LL) and plasticity index (PI) of the soil are 13% and 3%, while the activity A is equal to 0.45.

The reinforced fill has an average water content wc of 3.4%, a dry unit weight γ_d of 17.9 kN/m^3 (114 pcf), and a constant head hydraulic conductivity K of 4.5×10^{-4} m/s (127 ft/day) (Bowser-Morner, 2020). The pH, organic content, and resistivity (at 100% saturation) of the reinforced fill material are 9.0, 0.4%, and 122,400 ohm-cm (Bowser-Morner, 2020), values that satisfy the backfill electrochemical requirements specified in FHWA (2009a) and AASHTO (2020). Figure 2.6 shows the microscopic images of particles of the reinforced fill material retained on three different sieves (US sieve #20, #40, and #60); the percentage by mass of particles retained on these sieves (≈ 20%–25%) was greater than those retained on any of the other sieves, and, therefore, the morphology of these particles is likely to be representative of the reinforced fill. The particle images were analyzed using the MATLAB-based image analysis algorithm developed by Zheng and Hryciw (2015) to determine the morphology parameters of the reinforced fill. Based on the particle morphology analysis results, the average roundness (Wadell, 1932), width-to-length ratio sphericity (Krumbein & Sloss, 1951; Zheng & Hryciw, 2015, 2016), and diameter sphericity (Wadell, 1933) of the reinforced fill material are equal to 0.63, 0.74, and 0.84, respectively. Further details about the procedure for estimation of particle morphology can be found in Rahman et al. (2020).

Figure 2.7 shows the results of direct shear tests performed on dense samples of the fill material (relative density $D_R = 83 \pm 2\%$) for vertical normal stresses of 100, 200, and 300 kPa (2.1, 4.2, and 6.3 ksf). The critical-state friction angle ϕ_c of the sand (= 31.9°) was determined by taking the slope of a regression line (with zero intercept) plotted through the data points consisting of the measured shear stresses at critical state and the corresponding normal stresses. Further details about the test procedure can be found in Han et al. (2018).

Steel strip reinforcement. The reinforcement consists of galvanized, ribbed steel strips [ASTM A572 grade 65 steel with minimum yield strength $f_{y,min}$ = 65 ksi (448 MPa) and minimum ultimate tensile strength $f_{u,min}$ = 80 ksi (552 MPa) (ASTM, 2018b)] manufactured by

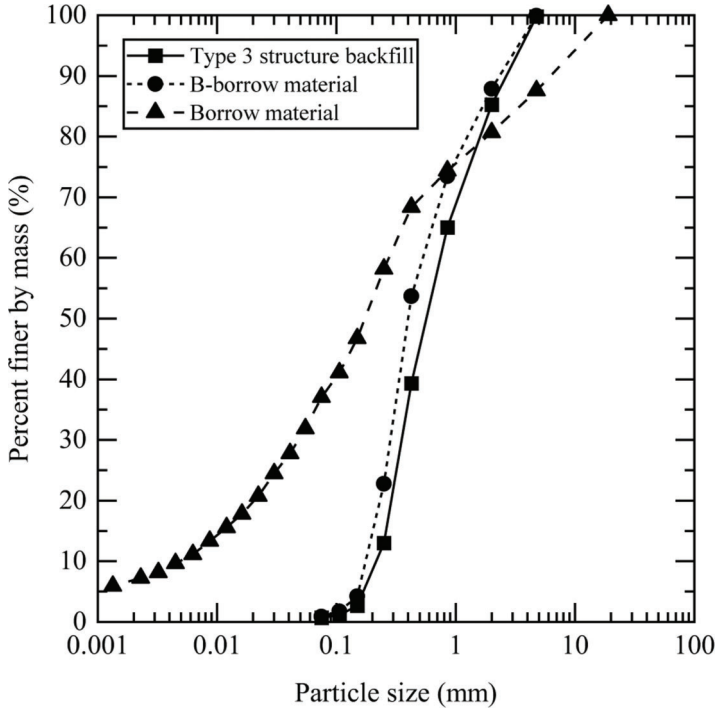

Figure 2.5 Particle-size distribution curves for type 3 structure backfill, B-borrow, and borrow materials.

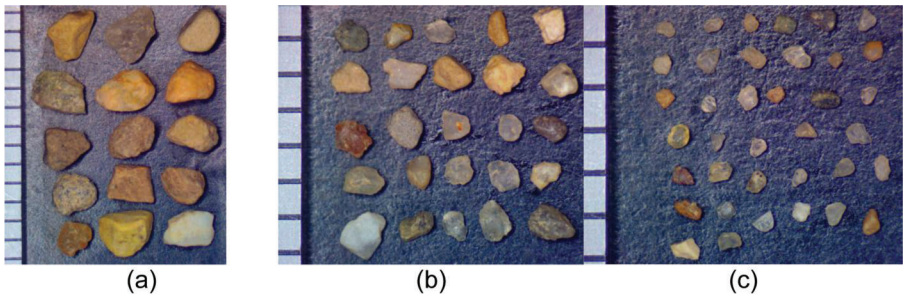

Figure 2.6 Images of particles of the reinforced fill material taken with a microscope: (a) particles retained on US #20 (0.85 mm) sieve, (b) particles retained on US #40 (0.425 mm) sieve, and (c) particles retained on US #60 (0.25 mm) sieve.

The Reinforced Earth Company (RECo). The length L_r of each instrumented steel strip is 18 ft (5.49 m), and both the vertical and horizontal spacings of adjacent strips are 2.46 ft (0.75 m). The width b_r and thickness t_r of the steel section for each strip are 2 in. (50 mm) and 5/32 in. (4 mm), respectively. The steel strips were connected to the back of the facing panels via the panel tie strips and a nut and bolt assembly. Some of the steel strips were skewed to a maximum angle of 15° to avoid intersecting the H-piles behind the wall facing; however, the strips that we selected for instrumentation were installed in a direction perpendicular (skew angle = 0°) to the back of the facing panels between adjacent piles.

Figure 2.8 shows the results of surface roughness of an 11-cm-(4.4-in.)-long and 5-cm-(2-in.)-wide steel strip sample measured using a Bruker NPFLEX optical profilometer (Singh & Sadeghi, 2024) at Kepner Laboratory, Purdue University. The 5-cm-wide steel strip sample was first subdivided into four regions, each of width equal to 1.25 cm (0.5 in.), and the surface roughness was then measured at three equidistant locations along the centerline of the sample in the lateral direction. Figure 2.8c shows a typical 3D contour plot of surface roughness across a measurement area of 5 mm × 0.9 mm (0.2 in. × 0.035 in.); the darker the shading in blue, the deeper the valleys of the surface profile are, whereas the darker the shading in red, the taller the peaks of the surface profile of the steel strip sample are. This can be visualized in Figure 2.8d, which shows the surface roughness profile in 2D along the centerline of the contour plot in the longitudinal direction.

Several parameters have been defined for surface roughness assessment: (1) centerline average roughness R_a, (2) maximum vertical peak-to-valley distance R_t over the entire measurement travel length, (3) maximum vertical peak-to-valley distance $R_{\max}$ over a reference

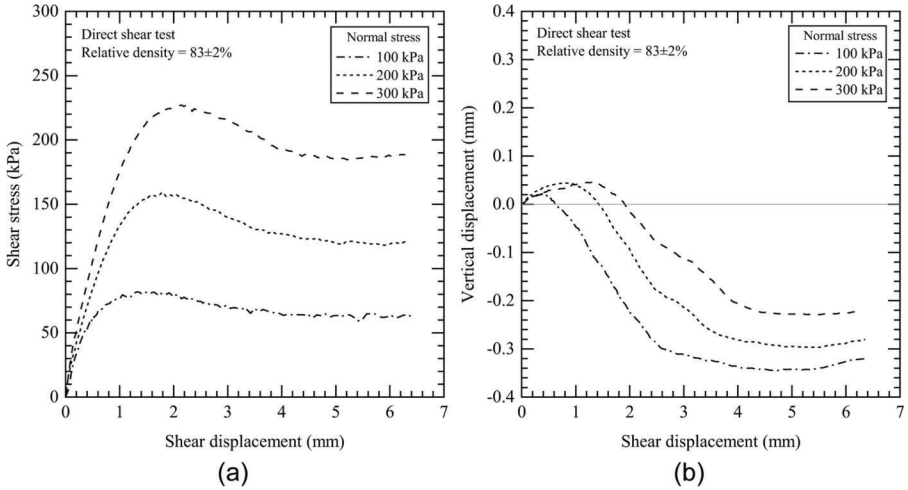

Figure 2.7 Direct shear test results for the reinforced fill material: (a) shear stress versus shear displacement, and (b) vertical displacement versus shear displacement.

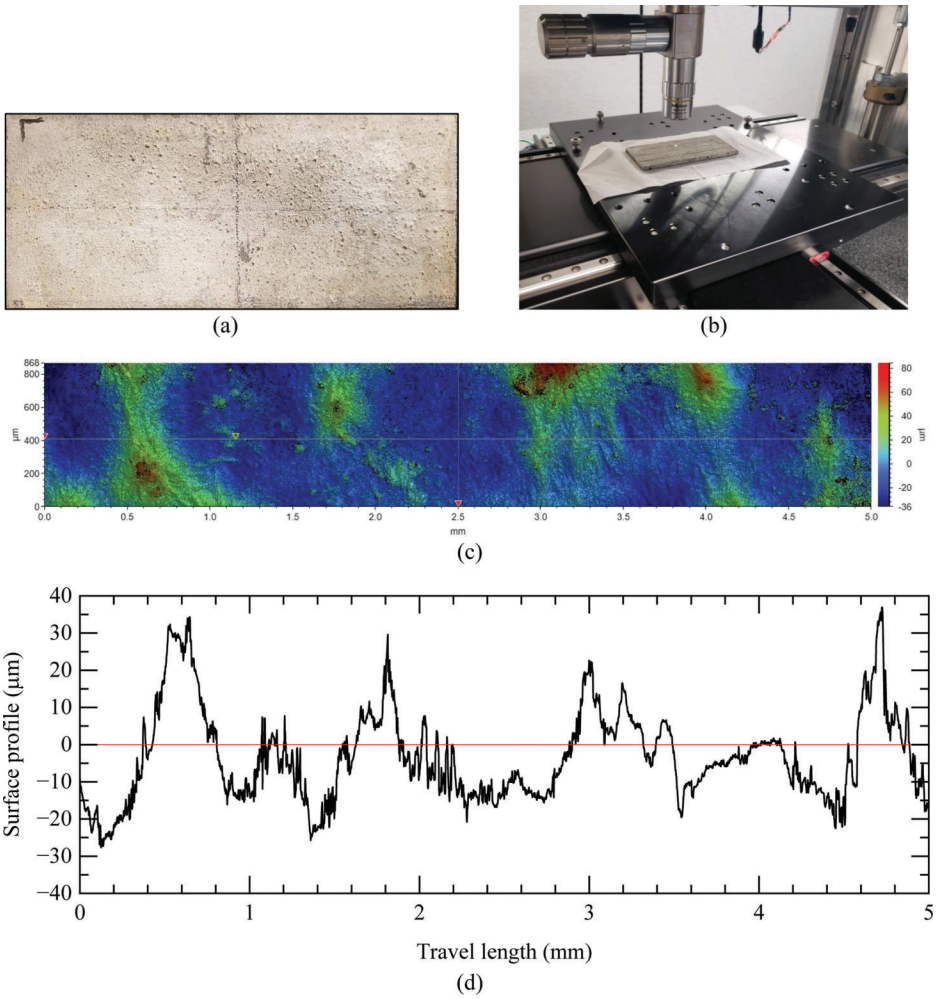

Figure 2.8 Measurement of surface roughness of steel strip reinforcement: (a) 11 cm × 5 cm sample of the steel strip, (b) placement of steel strip sample below the optical profilometer, (c) typical 3D contour plot of surface roughness across a measurement area of 5 mm × 0.9 mm, (d) 2D roughness profile along the centerline of the contour plot in the longitudinal direction.

length L_m (= D_{50}), (4) $R_{max,avg}$, which is the average of all values of R_{max} measured within a moving window (with window size L_m and moving step size δx between two consecutive data points) over the entire measurement travel length, and (5) normalized roughness R_n (= $R_{max,avg}/L_m$) (Han et al., 2018, 2019; Rahman et al., 2020; Tovar-Valencia et al., 2018). Based on the surface roughness analysis results obtained for the steel strip sample, the mean values of R_a, R_t, $R_{max,avg}$, and R_n are equal to 9.0 μm, 73.2 μm, 32.4 μm, and 0.057 μm, respectively. Following Han et al. (2018), for normalized roughness $R_n = 0.057$ and graded sands with $C_U \geq 2$, the ratio of the critical-state interface friction angle δ_c to the internal critical-state soil friction angle ϕ_c is estimated to be 0.85 for the Whitestown MSE wall steel strip-reinforced fill interface.

Bearing Pad. Each horizontal joint between adjacent facing panels consists of two ethylene propylene diene monomer (EPDM) bearing pads [ASTM D2000 grade 2, type B, class-E rubber material with durometer hardness of 80 (ASTM, 2018c)] with length, width, and thickness equal to 10 in. (254 mm), 2.75 in. (69.85 mm), and 0.75 in. (19.05 mm). The initial width of the vertical joint between adjacent facing panels is approximately 0.75 in. (19.05 mm); both the vertical and horizontal panel joints were covered by strips of geotextile filter cloth to prevent the loss of backfill material during the service life of the wall.

Figure 2.9 shows the average vertical load-compression curve of EPDM bearing pads obtained from five laboratory compression tests performed at a temperature of 20°C (68°F). For the Whitestown MSE wall, the vertical load carried by each bearing pad due to the self-weight of a facing panel is equal to 7.7 kN (1.73 kips). From Figure 2.9, we see that the vertical compression of the bearing pad corresponding to an applied vertical load of 7.7 kN (1.73 kips) is approximately 1.9 mm (0.075 in.), corresponding to 10% of the bearing pad thickness.

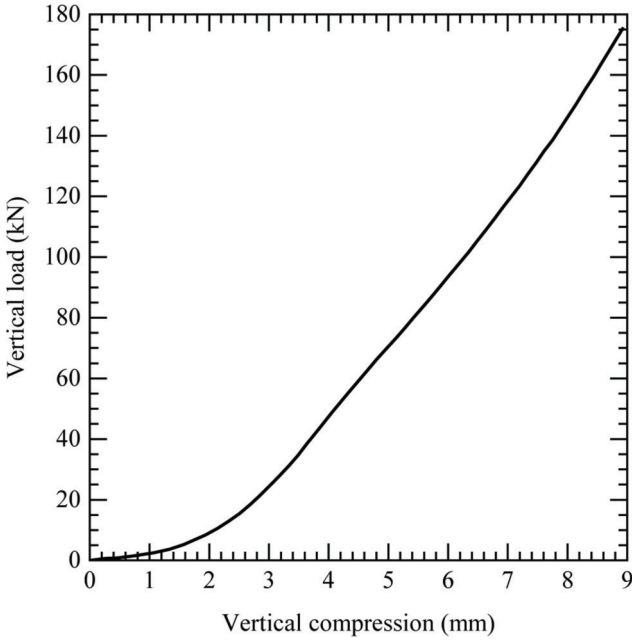

Figure 2.9 Average vertical load-compression behavior of EPDM bearing pad [data provided for five bearing pad samples tested (RECo, 2025)].

2.3 Abutment Construction

2.3.1 Pile Installation

Using a single-acting diesel hammer (Pileco Model D30–32), the H-piles were driven to depths ranging from 67.4–109.2 ft (20.5–33.3 m) below the leveling pad in October 2021, prior to the construction of the MSE wall. The hammer had a ram weight of 6,615 lbs (3,000 kg) and a maximum stroke length of 10.5 ft (3.2 m), generating a maximum rated energy of 69,457.5 lb·ft (94.1 kN·m). To minimize the interaction between the piles and the MSE wall, a 2-ft-(0.6-m)-diameter, corrugated, polyvinyl chloride (PVC) sleeve was placed over each pile after driving. The distance from the back of the wall facing to the front edge of the pile sleeve is 3 ft (0.9 m), and the gap between the pile and the sleeve was filled with pea gravel. The distance from the back of the wall facing to the front edge of the pile is approximately 3.5 ft (1.05 m), corresponding to 3.4 times the width of the pile flange [= 12.2 in. (0.31 m)].

Pile 1 of Bent 3 was driven to a depth of 109.2 ft (33.3 m) below the leveling pad. Dynamic load tests using the pile driving analyzer were performed on this pile by GRL Engineers, Inc., at the end of initial driving (EOID) on October 26th, 2021, and at the beginning of restrike (BOR) on October 29th, 2021. The mobilized pile shaft and base resistances were estimated by GRL Engineers, Inc., using the signal matching analysis program CAPWAP (Pile Dynamics, 2014). The CAPWAP pile capacity calculations indicated that (1) the total capacity Q_{total} of Pile 1 increased from 437 kips (1,944 kN) at EOID [pile set $w = 0.1$ in. (2.5 mm)] to 458 kips (2,037 kN) at BOR [$w = 0.11$ in. (2.8 mm)], values that exceed the specified nominal driving resistance of 392 kips (1,744 kN) for the piles in Bent 3; and (2) the shaft resistance of the pile increased by 11 kips (49 kN) during this period [from 302 kips (1,343 kN) at EOID to 313 kips (1,392 kN) at BOR], contributing to 52% of the increase in Q_{total}, while the base resistance increased by 10 kips (44 kN) [from 135 kips (601 kN) at EOID to 145 kips (645 kN) at BOR].

2.3.2 MSE Wall Construction

The top 5 ft (1.5 m) of clayey foundation soil was excavated along the footprint of the reinforced fill and replaced with compacted B-borrow material prior to construction of the MSE wall. The construction of the wall began on November 8th, 2021, with the pouring of concrete [minimum 28-day compressive strength =

2,000 psi (13.8 MPa) (RECo, 2020)] for the 1-ft-(30-cm)-wide and 0.5-ft-(15-cm)-thick leveling pad. The MSE wall and end bent were constructed in multiple stages, as shown in Table 2.1. Stage 1 involves the construction of the leveling pad and the first row of facing panels, with the reinforced fill material compacted up to the elevation of the first (bottommost) level of steel strips (Figure 2.10a). The reinforced fill was compacted in 6-in. (15-cm) lifts to at least 95% relative compaction using a pair of vibratory plate compactors (Model No. MVH-408GH, Multiquip Inc., Cypress, California). Stage 2 corresponds to the installation of the second row of facing panels, with the reinforced fill material compacted up to the elevation of the third level of steel strips Figure 2.10b. Stages 3 and 4 include the installation of the third and fourth rows of facing panels; the surface of the reinforced fill was at the elevations of the fifth and seventh (topmost) level of steel strips, respectively (Figure 2.10c and Figure 2.10d). The fourth row of facing panels have steel dowels that extend into a layer of cast-in-place (CIP) concrete that is poured on top of the panels; the height of the CIP concrete layer is 0.85 ft (0.26 m). Stage 5, which represents the end of wall construction, was completed on day 39 of construction and involves the installation of the coping on top of the CIP concrete layer (Figure 2.10e). The coping consists of precast concrete blocks that are 10 ft (3 m) long, 1.3 ft (0.4 m) wide, and 2.3 ft (0.7 m) high. The height of the reinforced fill (measured from the base of the leveling pad to the top of the reinforced fill) at the end of wall construction (stage 5) was 16.8 ft (5.13 m). The fill material was not placed all the way to the top of the coping because the pile cap was constructed on top of the reinforced fill at the surface elevation corresponding to stage 5.

Stage 6 involves the construction of the reinforced concrete pile cap over the H-piles, as shown in Figure 2.10f. The piles were embedded 2 ft (0.6 m) within the cap, and the gap between the coping and the pile cap was filled by blocks of expanded polystyrene (EPS) foam. Stage 7 corresponds to the placement of backfill material behind the pile cap and the installation of the bridge beams on top of the cap (Figure 2.10g). Stage 8 includes the construction of the 4.4-ft-(1.35-m)-high end bent above the pile cap (Figure 2.10h), while Stage 9 corresponds to the placement of backfill material behind the end bent and construction of the bridge deck (Figure 2.10i). Stage 10, which represents the end of bridge construction on day 361, involves the construction of the bridge approach slab and the pedestrian and exterior concrete railings on the bridge deck (Figure 2.10j). The thickness of the reinforced concrete deck is 8 in. (0.2 m) while that of the approach slab is 12 in. (0.3 m). The flanges of the H-piles were aligned parallel to the longitudinal direction of the bridge deck, which has a skew angle of 30° with respect to the end bent. The construction of the bridge was paused during stage 10 due to some issues related to the design of the pedestrian railing on the bridge deck. The bridge was opened to traffic on June 26th, 2023, after completion

TABLE 2.1
Main construction stages of Bent 3 of the Whitestown Parkway Bridge in Indiana

Stage	Approximate Time Period	Duration (days)	Time Elapsed (days)[a]	Height of Reinforced fill (m) [ft][b]	Activity
1	11/8/2021 to 11/10/2021	2	2	0.54 [1.8]	Construction of leveling pad and first row of facing panels + placement of backfill material up to the first reinforcement layer
2	11/10/2021 to 11/17/2021	7	9	2.04 [6.7]	Installation of second row of facing panels and placement of backfill material up to the third reinforcement layer
3	11/17/2021 to 11/30/2021	13	22	3.54 [11.6]	Installation of third row of facing panels and placement of backfill material up to the fifth reinforcement layer
4	11/30/2021 to 12/10/2021	10	32	5.04 [16.5]	Installation of fourth row of facing panels and placement of backfill material up to the seventh reinforcement layer
5	12/10/2021 to 12/17/2021	7	39	5.13 [16.8]	Installation of coping and placement of additional backfill material above the seventh reinforcement layer
6	12/17/2021 to 1/11/2022	25	64	5.13 [16.8]	Construction of the reinforced concrete pile cap
7	1/11/2022 to 1/20/2022	9	73	6.32 [20.7]	Placement of backfill material behind the pile cap and installation of the bridge beams on top of the pile cap
8	1/20/2022 to 2/14/2022	25	98	6.32 [20.7]	Construction of the integral end bent
9	2/14/2022 to 5/6/2022	81	179	7.46 [24.5]	Placement of backfill material behind the end bent and construction of the bridge deck
10	5/6/2022 to 11/4/2022	182	361	7.56 [24.8]	Construction of the bridge approach slab and the pedestrian and exterior concrete railings on the bridge deck

Note: Compacted sandy soil was placed in front of the first row of facing panels by the time the abutment was fully constructed (Figure 2.1). The height of this soil layer (measured from the base of the leveling pad) was about 0.7 m (2.3 ft) at the end of wall construction (stage 5) and 0.9 m (3 ft) at the end of bridge construction (stage 10).

[a]Measured from the start of wall construction on November 8th, 2021, to the end of each stage.

[b]Measured from the base of the leveling pad to the top of the backfill soil at the end of each stage.

of the concrete curbs and placement of the hot mix asphalt for the bridge approach roadway.

2.4 Abutment Instrumentation

A variety of sensors, including earth pressure cells, strain gauges, inclinometers, and crackmeters were used to measure the magnitude and evolution of several quantities, such as the vertical stresses at the base of the leveling pad and within the backfill soil, the lateral earth pressure on the back of the wall facing, the tensile loads in the reinforcement, the lateral deflection of the wall facing, the contraction of the panel joints, and the settlement of the MSE wall foundation.

2.4.1 Earth Pressure Cells and Reinforcement Strain Gauges

Figure 2.11a shows the layout of the 6-mm-(0.24-in.)-thick earth pressure cells (Model No. 4800–1, Geokon, Lebanon, New Hampshire) installed at the base of the leveling pad and within the reinforced fill to measure vertical stresses. The pressure cells have a diameter of 230 mm (9 in.) and a measurement range of 1 MPa (20.9 ksf) (Figure 2.11b); they consist of two stainless steel plates welded together around their periphery to leave a narrow space between them for de-aired hydraulic oil. The stresses exerted by the reinforced fill works to squeeze the two plates together, thus building up pressure inside the oil, which is measured by a vibrating-wire pressure transducer (Model No. 4500H, Geokon, Lebanon, New Hampshire). The pressure transducer converts the oil pressure into an electrical signal, which is then transmitted through a signal cable to the readout device. The pressure transducer housing has a thermistor to measure the temperature at the location of the pressure cell. A bubble level was used to ensure that the surface of the pressure cell was flat and that the cell was placed on level ground.

Figure 2.12a shows the layout of the 12-mm-(0.48-in.)-thick pressure cells (Model No. 4810, Geokon, Lebanon, New Hampshire) installed upright on the back of the wall facing to measure the lateral stresses. These pressure cells have a thick back plate that is designed to bear against the external surface of a structure in a way that prevents the bending of the cell, while the thin, pressure-sensitive front plate of the cell reacts to the soil pressure. To smoothen out any surface irregularities that might exist on the facing panel, a thin cement mortar pad was first placed on the back of the panel at the expected location of the pressure cell. The pressure cells were then anchored to the back of the facing panels (between two adjacent tie strips) using the four mounting lugs welded to the edge of each cell (Figure 2.12b). Both the model 4800 and 4810 vibrating-wire pressure cells were installed along two sections of the MSE wall; this was done for the purpose of redundancy as well as to ensure consistency and repeatability of the measurements. The distance between the two instrumented sections (in the longitudinal direction of the wall) is about 2 m (6.5 ft) for the model 4800 pressure cells and 1.4 m (4.6 ft) for the model 4810 pressure cells. Four out of the seven levels of steel strips were instrumented with strain gauges along two sections of the wall facing, as detailed next.

Figure 2.11a shows the layout of the vibrating-wire strain gauges (Model No. 4150, Geokon, Lebanon, New Hampshire) installed on the steel strips along two instrumented sections (section 1 and section 2) spaced 2.2 m (7.3 ft) apart (in the longitudinal direction of the wall) to determine the magnitude and distribution of the tensile loads in the reinforcements. At each gauge location, the zinc galvanization coating was first removed using a power grinder, and the strain gauge was then spot-welded to the surface of the steel strip (Figure 2.11c) using a rapid capacitive discharge bonder (Model S100 Stinger, Bridge Diagnostics, Inc., Louisville, Colorado) with a weld energy of about 20–30 Joules. After the gauge was installed on the surface of the steel strip, a half-cylindrical cover plate [length = 100 mm (4 in.) and diameter = 20 mm (0.8 in.)] was spot-welded over the gauge to protect it from mechanical damage (Figure 2.11d). The openings of the cover plate were sealed using a Permatex gasket sealant gel (RTV silicone) to prevent any intrusion of soil particles or water molecules into the gauge. The galvanization coating was then restored on the steel strip around the gauge location using a Krylon galvanizing primer

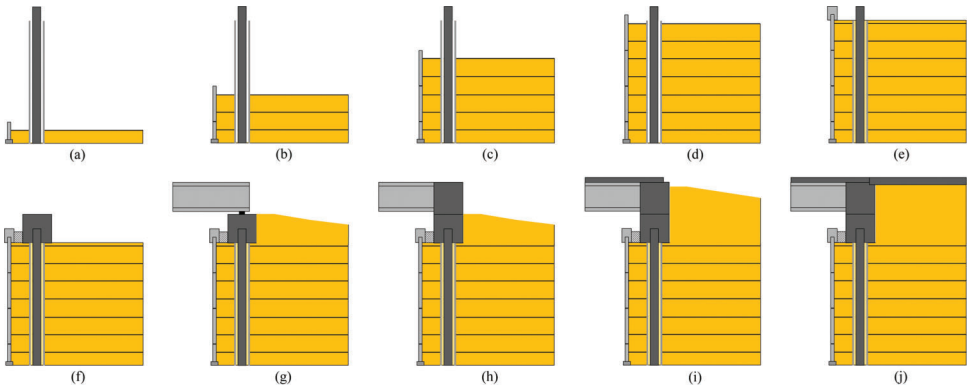

Figure 2.10 Construction of Bent 3 of the Whitestown Parkway Bridge in multiple stages (stages 1–10 are represented in sequence by illustrations a–j).

spray. All strain gauges have a gauge length of 51 mm (2 in.) and a measurement range of 3,000 microstrain. The gauges were installed on the top and bottom surfaces of the reinforcement at each gauge location so that the average of their readings would reflect changes in axial strains alone and cancel out any potential minor bending effects. The gauges were more closely spaced near the expected location of the theoretical maximum tensile strain as per AASHTO (2020) for enhanced resolution. In addition, a pair of strain gauges were installed 15 cm (6 in.) behind the facing panels to determine the loads near the panel-strip connection point.

2.4.2 Crackmeters and Inclinometers

Figure 2.12a shows the layout of the vibrating-wire crackmeters (Model No. 4420–1–100, Geokon, Lebanon, New Hampshire) installed at the horizontal and vertical joints of facing panels 2 and 3 to measure the joint gap width. The crackmeters were installed using ball-jointed expansion anchors by drilling two 10-mm-(0.4-in.)-diameter and 32-mm-(1.25-in.)-deep holes, one on each side of the panel joint, at the desired location (Figure 2.12c). Crackmeter CM-1 was installed at the horizontal joint between panels 2 and 3, whereas crackmeter CM-6 was installed at the horizontal joint between panels 3 and 4. Similarly, crackmeters CM-2 and CM-3 were installed at the vertical joints between panel 2 and panels 2N and 2S, respectively, whereas crackmeters CM-4 and CM-5 were installed at the vertical joints between panel 3 and panels 3N and 3S, respectively. Each crackmeter consists of a heat-treated, stress-relieved spring; one end of the spring is connected to a vibrating-wire sensing element while the other end is connected to an extension rod. When the extension rod is either pulled out from, or pushed into, the gauge body, the spring either elongates or contracts, causing an increase or decrease in tension, which is sensed by the vibrating-wire element. The change in tension (or strain) of the wire is directly proportional to the movement of the extension rod, thus allowing the crackmeter to measure the expansion or contraction of the joint. The crackmeters were protected using half-cylindrical polyvinyl chloride (PVC) pipe segments; the openings of the pipe segments were sealed using Great Stuff™ insulating foam sealant.

Two vertical inclinometer casings (Model No. 6400–2–10, Geokon, Lebanon, New Hampshire) were installed in the space between adjacent piles: one casing at a horizontal distance of about 0.1 m (4 in.) from the back of the facing panels, and the other casing within the reinforced fill at a distance of 2.5 m (8.2 ft) from the back of the panels. Each casing is made up of acrylonitrile butadiene styrene (ABS) plastic and has an outer diameter of 70 mm (2.8 in.), an inner diameter of 59 mm (2.3 in.), and a segment length of 3 m (10 ft). The casings were installed in 75-mm-(3-in.)-diameter boreholes that were drilled up to a depth of 10.6 m (34.8 ft) below the leveling pad prior to wall construction. The casings were grouted in-place at the bottom of the borehole using cement-bentonite tremie grout, and adjoining casing segments were attached using a standard male-to-female connection system and waterproofed using caulk and duct tape. The casing segments were attached in sequence within the zone of the reinforced fill, i.e., a casing segment of the inclinometer was attached to the previous segment when the surface of the reinforced fill was close to its top surface. Baseline measurements of the vertical profile of the casing were recorded using a Durham Geo Slope Indicator (DGSI) digitilt inclinometer probe at depth intervals of 0.6 m (2 ft). Subsequent readings during and after

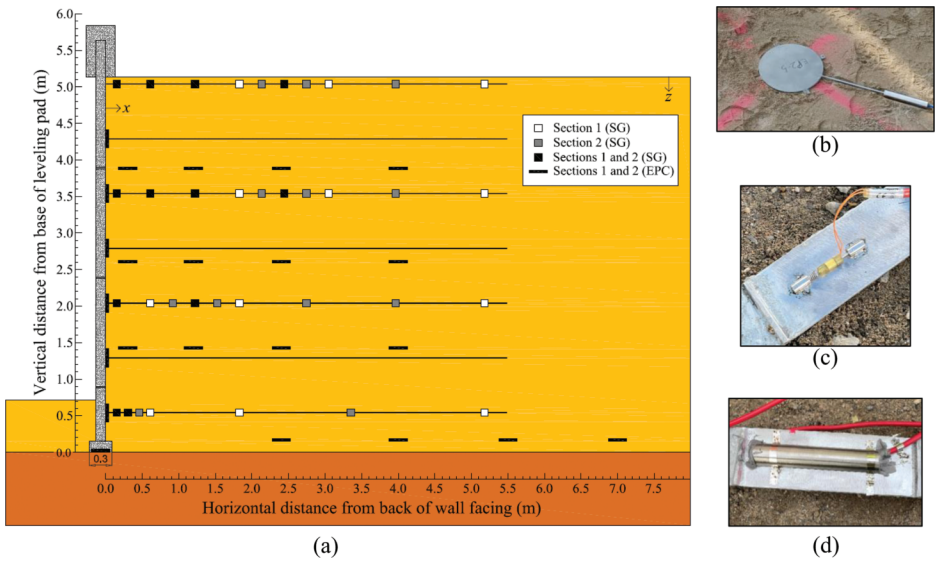

Figure 2.11 Instrumentation of the MSE wall: (a) sensor layout, (b) photograph of an earth pressure cell (EPC) placed flat on the surface of the reinforced fill, (c) photograph of a strain gauge (SG) spot-welded to the surface of the steel strip, and (d) photograph of the cover plate used to protect the strain gauge.

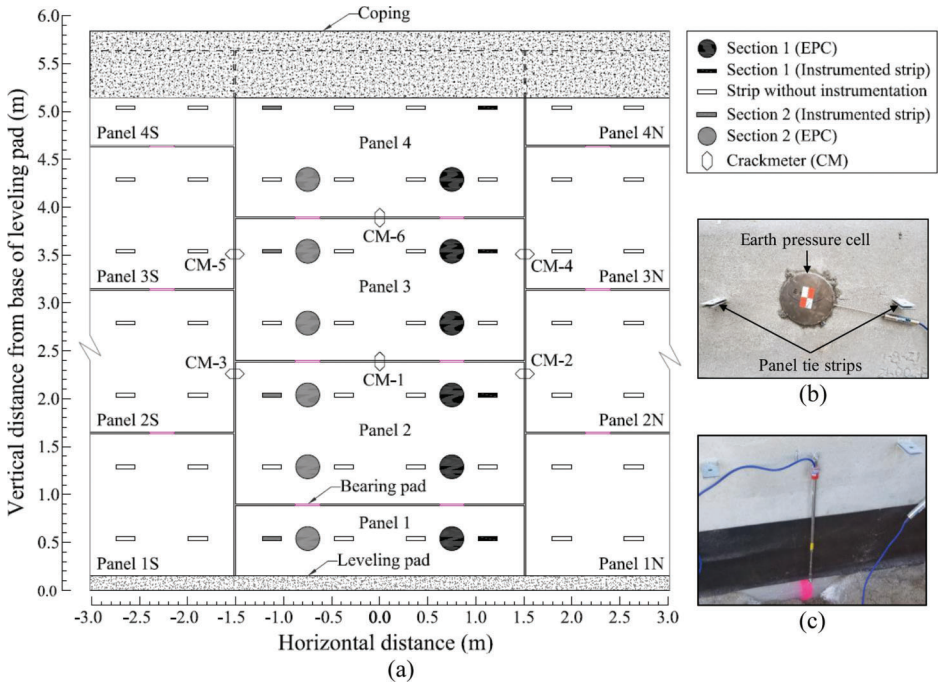

Figure 2.12 View from the back of the wall facing: (a) layout of earth pressure cells and crackmeters, (b) photograph of a pressure cell installed on the back of the facing panel between two adjacent tie strips, and (c) photograph of a crackmeter installed at a horizontal joint between adjacent panels (the joints were covered by geotextile strips).

construction of the bridge abutment were recorded using microelectromechanical (MEMS) in-place inclinometer (IPI) systems.

In addition to the vertical inclinometers, a 12.2-m-(40-ft)-long horizontal inclinometer casing (Model No. 6400–2–10, Geokon, Lebanon, New Hampshire) was installed below the MSE wall foundation and leveling pad prior to wall construction. The east end of the casing is located 8.8 m (29 ft) behind the centerline of the wall facing within the backfill soil, while the west end of the casing is located 3.4 m (11 ft) in front of the facing centerline. A string of 11 MEMS tilt sensors (Model No. 6155C-1, Geokon, Lebanon, New Hampshire), mounted on stainless-steel tubes linked by universal joints, was inserted into the casing from the east end. The length of each sensor segment (measured between adjacent wheel bearings) is approximately 1 m (3.3 ft), except for the last (eleventh) tilt sensor, whose segment length is 0.55 m (1.8 ft). The tilt sensors have a measurement range of $\pm 15^{\circ}$ with respect to the horizontal, and the length and diameter of each tilt sensor are 362 mm (14.25 in.) and 32 mm (1.25 in.).

2.4.3 Pile and Rebar Strain Gauges

A pair of arc-weldable, vibrating-wire strain gauges (Model No. 4000, Geokon, Lebanon, New Hampshire) were installed near the heads of three H-piles (piles 11, 12, and 13 counted in sequence from the north end of the pile cap) located within the instrumented zone of Bent 3 (Figure 2.13a); these piles were driven to a depth of 24.8 m (81.4 ft) below the leveling pad. Pile 12 (Figure 2.13b) was located approximately in the middle of the instrumented zone highlighted in Figure 2.1, whereas piles 11 and 13 were located to the north and south ends of the instrumented zone. Each pair of strain gauges were welded 0.9 m (3 ft) below the pile head on diametrically opposite sides (north and south sides) of the pile flange (as illustrated in Seo et al., 2009) to cancel out any potential bending effects that may exist near the pile head. The arc-weldable strain gauges have a gauge length of 150 mm (6 in.) and a measurement range of 3,000 microstrain; the gauges were protected using steel angles welded over them on each side of the pile flange, and the openings of the steel angles were filled with Great Stuff™ insulating foam sealant. Six vibrating-wire rebar strain gauges (Model No. 4911, Geokon, Lebanon, New Hampshire), with gauge length = 914 mm (36 in.) and measurement range = 3,000 microstrain, were installed in the pile cap (Figure 2.13c). These gauges were tied (using iron-tie wires) to the 19-mm-(0.75-in.)-diameter #6 vertical rebars adjacent to the instrumented piles within the same cross section of the pile cap (i.e., approximately 0.6 m (2 ft) above the base of the pile cap).

2.4.4 Data Acquisition

A Trimble-Seiler Global Positioning System (GPS) mapping device was used to determine the GPS coordinates (northing, easting, and elevation) of each sensor and to verify that the sensor was installed at the desired location marked on the project drawings. After installation, each sensor was first connected to a

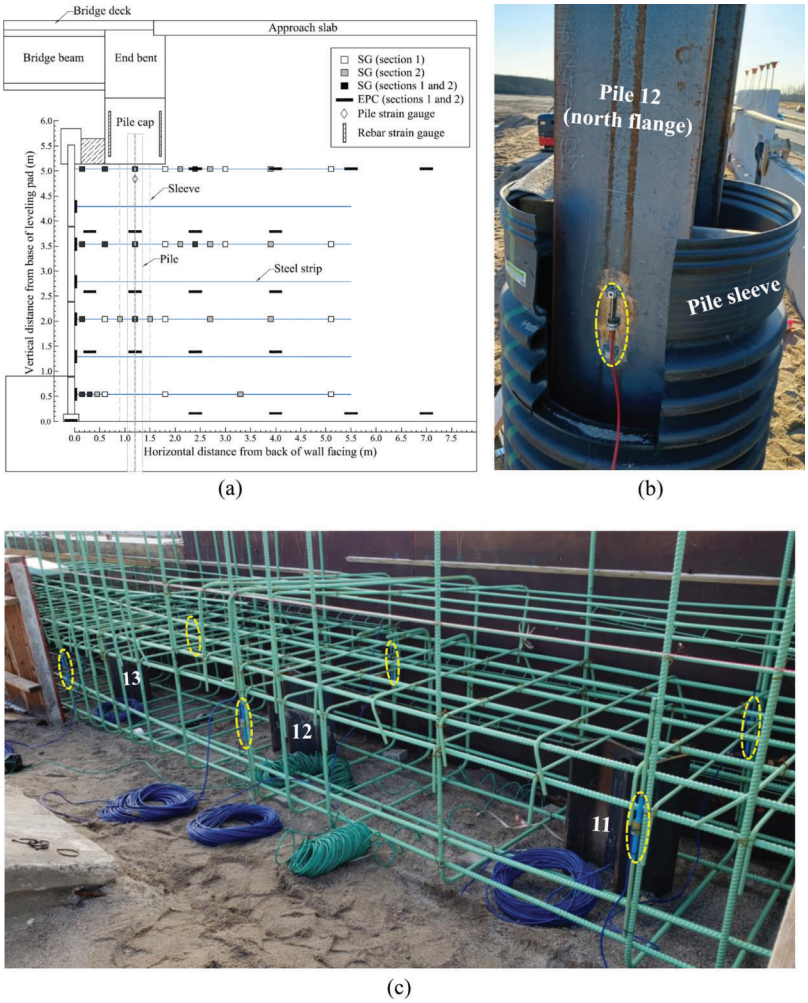

Figure 2.13 Instrumentation of Bent 3 of the Whitestown Parkway Bridge: (a) sensor layout, (b) photograph of arc-weldable strain gauge installed on the north flange of pile 12, and (c) photograph of rebar strain gauges tied to the vertical rebars adjacent to piles 11, 12, and 13.

portable readout unit (Model No. GK-403, Geokon, Lebanon, New Hampshire) to obtain the initial readings and temperatures. The cables from the sensors were then routed through a series of hollow PVC cellular core pipes [inner diameter = 100 mm (4 in.) and wall thickness = 6 mm (0.24 in.)] and connected to the data acquisition (DAQ) system located 10 m (33 ft) beyond the footprint of the MSE wall. The PVC pipes served to protect the sensor cables during placement and compaction of the reinforced fill material; the pipes were installed within the reinforced fill at each elevation where the sensors were present.

The DAQ system consists of twelve multiplexers (Model No. 8032–16–1S, Geokon, Lebanon, New Hampshire) and three dataloggers (Model No. 8600–1, Geokon, Lebanon, New Hampshire) equipped with Campbell Scientific CR-6 measurement and control units—two dataloggers for use with the vibrating-wire sensors and one datalogger for use with the MEMS sensors. Each datalogger was powered by a 20W solar panel (Model No. 8020–7–2, Geokon, Lebanon, New Hampshire) and regulated using a SunKeeper junction-box mounted solar charge controller (Model No. SK-6, Morningstar Corporation, Newtown, Pennsylvania). The solar charge controller was used to keep the 12Vdc battery of the datalogger from overcharging by regulating the voltage and current coming from the solar panel to the battery. LoggerNet, software developed by Campbell Scientific, Inc., was used to display and retrieve the data collected by the dataloggers; the data was collected continuously at a frequency of 4 hours.

2.5 Live Load Test

With the westbound lanes of the bridge temporarily closed to traffic, a live load test was performed on October 30th, 2023, from approximately 8:00 am to 11:30 am. Twelve triaxle dump trucks, fully loaded with coarse aggregate material (#53 stone), were used to apply the live loads on the instrumented MSE abutment. The distance between the front axle and the rear-middle axle of the truck ranged from 4.6–5.7 m

(15.0–18.8 ft), while that between the rear-middle axle and the back axle of the truck was approximately 1.4 m (4.7 ft); the width of the truck was about 2.75 m (9 ft). The gross weight of each truck was measured before the live load test; the average gross weight of all the trucks was 329 kN (74 kips), with a coefficient of variation of 4%. The differences in the gross truck weights measured before and after the live load test were small [≈ 1 kN (0.23 kips)].

TABLE 2.2
Loading protocol for the live load test on the Whitestown Parkway Bridge

	Number of Trucks at Each Location						
Step	**G**	**F**	**E**	**D**	**C**	**B**	**A**
0	0	0	0	0	0	0	0
1(a)	0	0	0	1	0	0	0
1(b)	0	0	0	2	0	0	0
1(c)	0	0	0	3	0	0	0
2	0	0	0	3	3	0	0
3	0	0	0	3	3	3	3
4	0	0	3	3	3	3	0
5	0	3	3	3	3	0	0
6	3	3	3	3	0	0	0
7	0	0	3	3	0	0	0
8(c)	0	0	0	3	0	0	0
8(b)	0	0	0	2	0	0	0
8(a)	0	0	0	1	0	0	0
9	0	0	0	0	0	0	0

2.5.1 Test Procedure and Loading Protocol

The live load test was performed by parking the trucks at specific locations (marked using tape and spray paint) near Bent 3 of the bridge. Table 2.2 summarizes the number of trucks parked at each location (A–G) during the 13 steps of the live load test (steps 1 to 6 are loading steps, while steps 7 to 9 are unloading steps). The load sequence prescribed in Table 2.2 was intended to simulate several trucks approaching Bent 3, driving over Bent 3, and then leaving the bridge. For example, locations A, B, and C lie within the approach roadway of the bridge, location D corresponds to the centerline of the piles and pile cap of Bent 3, while locations E, F, and G correspond to different points along the bridge deck Figure 2.14a). At each of these locations, a maximum of three trucks were parked side-by-side and aligned parallel to the longitudinal direction of the wall, as shown in Figure 2.14b. The instrumented zone of Bent 3 lies below the westbound traffic lane adjacent to the pedestrian walkway (Figure 2.14c). The readings from the sensors were monitored continuously during each step of the live load test, and the next step was executed only after the MSE wall displacements had stabilized for the previous step (stabilization meant that two consecutive readings were the same). The duration of each step of the live load test was approximately 15 minutes on average. Figure 2.15 shows some photographs of the trucks taken during the live load test.

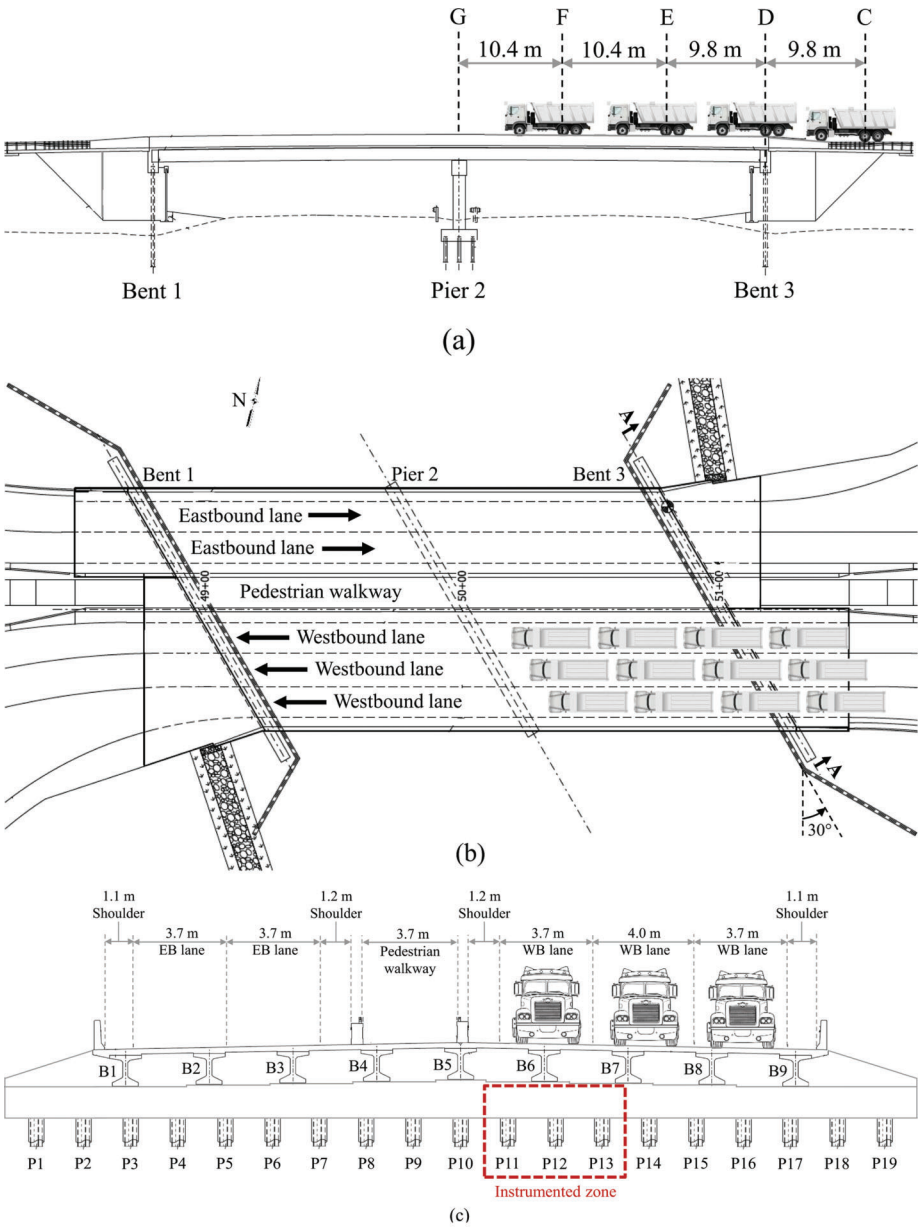

Figure 2.14 Locations on the bridge where the live loads were applied (truck locations for step 5 of the live load test are shown in the figure): (a) side view of the bridge (locations A and B are 10.4 m (34 ft) to the east of location C and are not shown in the figure), (b) top view of the bridge, and (c) view along section A-A of Bent 3 showing the lane configuration (B: beam, P: pile).

Figure 2.15 Photographs of the trucks taken during the live load test on the Whitestown Parkway Bridge: (a) side view, and (b) front view.

3. MONITORING DURING WALL CONSTRUCTION

3.1 Vertical Stresses

3.1.1 Vertical Stresses at Base of Leveling Pad and Within Reinforced Fill

Figure 3.1 shows the evolution of the vertical stresses measured by the earth pressure cells located at the base of the leveling pad and at different elevations (depths) within the reinforced fill during construction of the MSE wall. The vertical stresses were averaged across the two instrumented sections because their values were found to be consistent with each other. The horizontal distance of the pressure cell from the back of the wall facing is denoted by x, while the depth of the pressure cell from the top of the reinforced fill (at the end of wall construction) is denoted by z. A value of x equal to zero corresponds to the pressure cells at the base of the leveling pad (these pressure cells were installed along the centerline of the leveling pad), whereas values of x greater than zero correspond to the pressure cells within the reinforced fill. It can be observed from Figure 3.1d that (1) the vertical stresses at the base of the leveling pad are consistently higher than those measured along the base of the reinforced fill both during and after wall construction, and (2) the vertical stresses from the fill pressure cells installed at different horizontal distances [x = 2.4–7.0 m (8–23 ft)] behind the wall facing are generally close to each other, with a coefficient of variation of about 5%, which may be attributed to minor

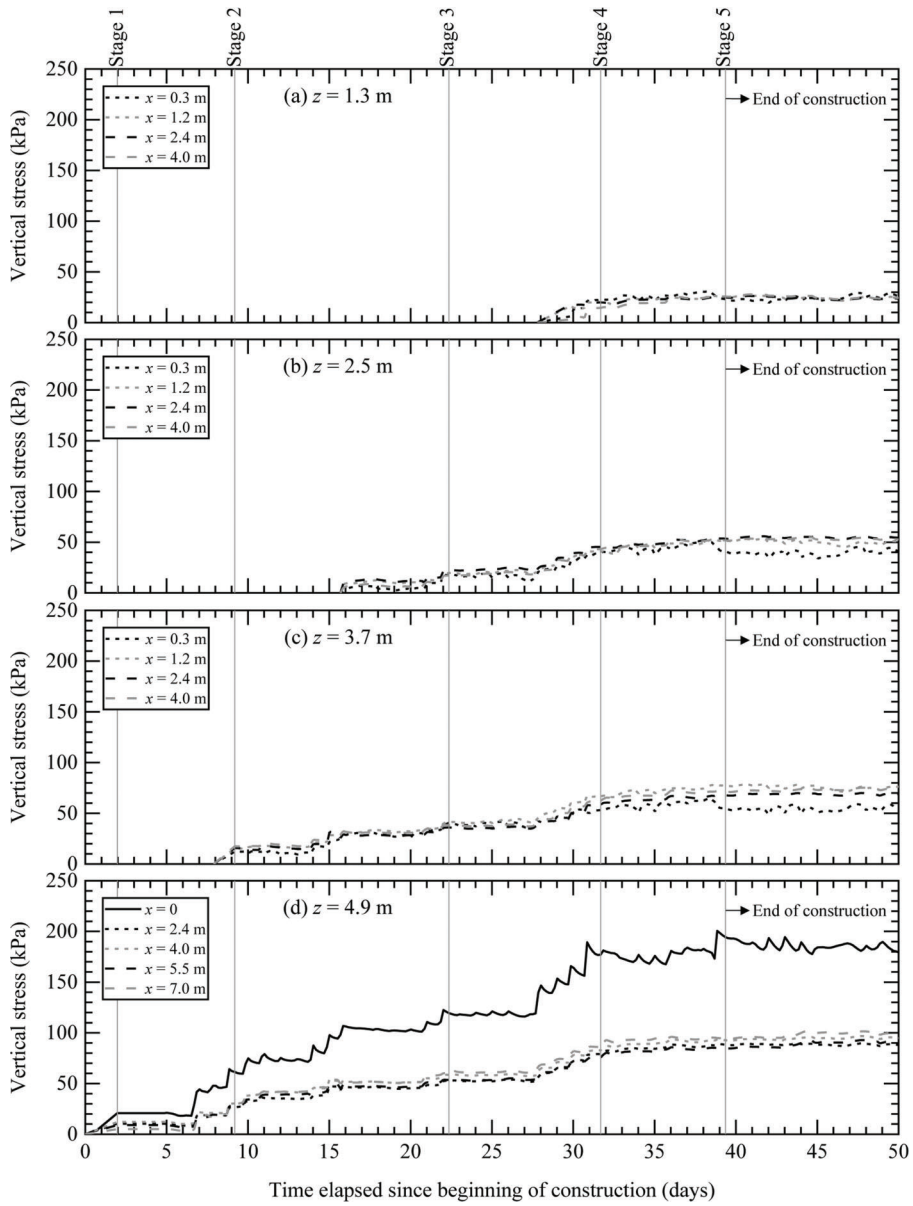

Figure 3.1 Evolution of vertical stresses at four elevations within the MSE wall during and after wall construction: (a) z = 1.3 m (4.3 ft), (b) z = 2.5 m (8.2 ft), (c) z = 3.7 m (12.1 ft), and (d) z = 4.9 m (16.1 ft).

local variations in soil density across the MSE wall footprint. The vertical stresses at the base of the leveling pad increased from 19 kPa (397 psf) at the end of stage 1 to 118 kPa (2,464 psf) at stage 3 and, finally, to 190 kPa (3,968 psf) at the end of wall construction (stage 5). In contrast, the average vertical stresses near the base of the reinforced fill increased from about 8 kPa (167 psf) at the end of stage 1 to 57 kPa (1,190 psf) at stage 3 and, finally, to 91 kPa (1,901 psf) at the end of wall construction (Figure 3.1d). The readings from the pressure cells stabilized after the end of wall construction based on the measurement recorded on day 50 from the start of wall construction.

The vertical stresses measured just behind the facing panels [$x = 0.3$ m (1 ft)] are less than those measured farther away from the back of the panels [$x \geq 1.2$ m (4 ft)], particularly after the end of wall construction (as illustrated by Figure 3.1b) and Figure 3.1c corresponding to $z = 2.5$ m (8.2 ft) and 3.7 m (12.1 ft)]. The reduction in vertical stress just behind the facing panels may be attributed to the effects of soil arching (Paik & Salgado, 2003) and stress transfer from the reinforced fill to the wall facing as the panels attempt to move away from the reinforced fill and the fill material tries to slide down behind the wall. The wall facing provides vertical support to the backfill through friction between the fill material and the wall, which, in turn, reduces the vertical stress in the soil just behind the facing. For $z =$ 1.3 m (4.3 ft), the vertical stresses measured just behind the facing panels are generally in good agreement with those measured farther away from the back of the panels (Figure 3.1a), indicating that the effects of soil arching and stress redistribution are small near the top of the wall.

Figure 3.2 shows the distribution of vertical stresses behind the wall facing four different elevations within the reinforced fill at the end of wall construction. The earth pressure cell (EPC) installed in section 1 at the base of the leveling pad malfunctioned prior to stage 2 of wall construction, and therefore the data from this pressure cell was not included in Figure 3.2d; the malfunction may have been due to potential unstable contact either between the concrete of the leveling pad and the pressure cell or between the surface of the pressure cell and the underlying soil. It can be observed from Figure 3.2 that (1) the vertical stress is highest at the base of the leveling pad (Figure 3.2d), and (2) the vertical stress decreases to values less than γz just behind the facing panels (Figure 3.2a–c), because of arching, as discussed previously in connection with Figure 3.1. For $x \geq 1.2$ m (4 ft), the vertical stresses measured at different elevations within the reinforced fill are generally in good agreement with those calculated based on the backfill self-weight γz. The stresses transferred to the wall facing and the leveling pad during construction of the MSE wall can be quantified through the vertical stress ratio, which is presented and discussed in the next section.

Cell action factors were not applied to the earth pressure cell measurements for the following reasons.

1. The cell action factor depends on two variables: the aspect ratio (ratio of cell thickness to diameter) of the pressure cell and the modular ratio (ratio of the Young's modulus of the pressure cell to the Young's modulus of the soil in which the cell is installed) (Taylor, 1945). Both these variables affect the measurements obtained from pressure cells installed within a compacted soil mass and may cause the cells to measure either higher or lower values of stress depending on the soil conditions and the cell installation method (Peattie & Sparrow, 1954); the cell action factor in essence attempts to correct for these differences. Weiler and Kulhawy (1982) and Dunnicliff (1988) suggested that the errors associated with cell geometry and stiffness compatibility could be minimized by using stiff/rigid pressure cells with aspect ratios less than 0.1. The aspect ratio of the hydraulic-type pressure cells used in this study is 0.026 (cell thickness = 6 mm and cell diameter = 230 mm), and, as mentioned earlier, each cell consists of two, thin, stainless steel plates welded together around their periphery to leave a narrow space between them for de-aired hydraulic oil, making the cell "stiff/rigid" in comparison to the backfill soil used for construction of the Whitestown MSE wall.
2. The pressure cells were installed using the so-called "set-on-surface method" (Hadala, 1967) (i.e., the cells were set flat on level ground followed by standard construction procedures to complete the fill around the cells). According to Hadala (1967), pressure cells installed in a laboratory test chamber on dense sand using the "set-on-surface method" measured values of vertical stresses that were 6% greater (compared to the actual value), on average, versus other methods of cell installation that produced less accurate vertical stress measurements (= 37% and 50% higher vertical stresses for the "tamping-in" and "raised-mound" methods). At the end of construction of the Whitestown MSE wall, we found that the vertical stresses measured by the pressure cells at different elevations and cross sections within the reinforced fill were approximately 7% greater, on average, than those calculated based on the backfill self-weight γz.
3. The response of a pressure cell installed within a compacted soil mass also depends on the degree of soil compaction near the cell versus that further away from the cell location. According to Dunnicliff and Green (1988), if heavy equipment (e.g., rollers), for example, are used to compact the backfill soil, and the pressure cell is installed in an excavated trench that is backfilled and compacted using hand tamping or light machines (to avoid damaging the cell), the pressure cell would be surrounded by a volume of soil with greater compressibility than the rest of the fill, resulting in the measurement of vertical stresses that would be smaller than the actual values. For the Whitestown MSE wall, the entire reinforced fill material was compacted using vibratory plate compactors (both near the cells as well as in locations away from the cells), and, consequently, the effect of soil compaction on the pressure cell measurements would be minimal.

3.1.2 Vertical Stress Ratio

The vertical stress ratio is defined as the ratio of the vertical stress $\sigma_v|_{\mathrm{lp,m}}$ measured at the base of the leveling

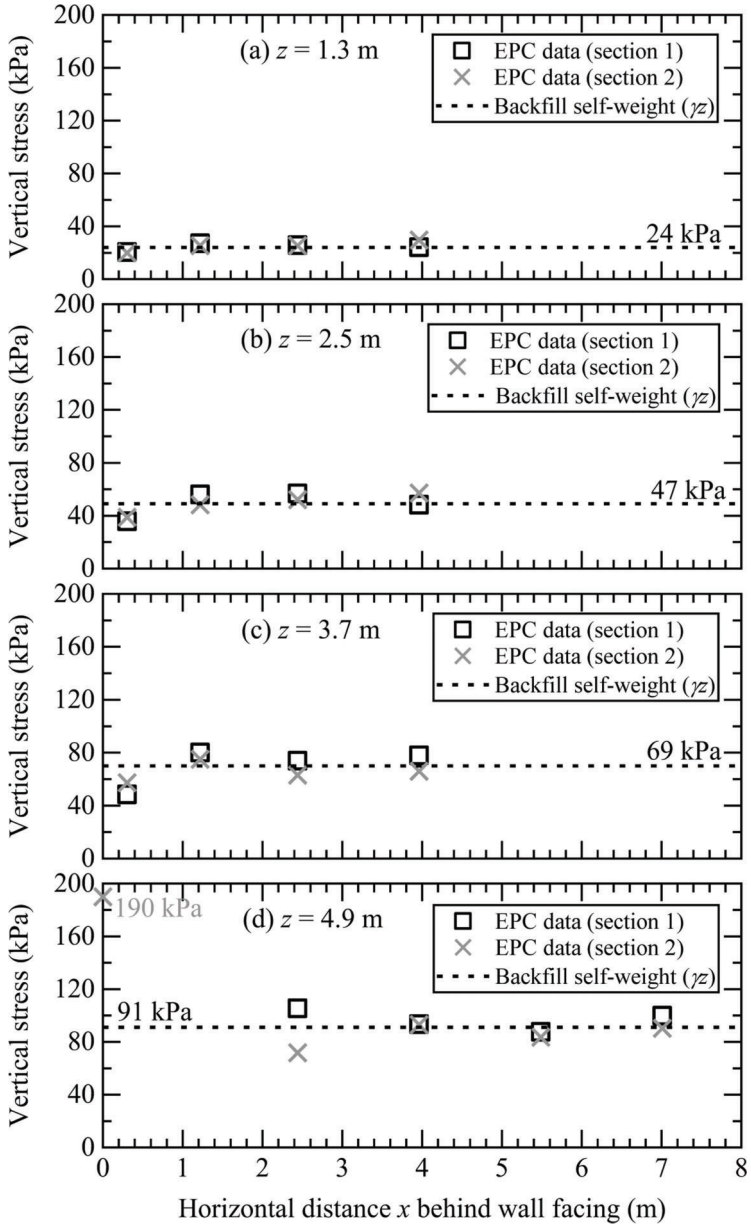

Figure 3.2 Distribution of vertical stresses at four elevations within the MSE wall at the end of wall construction: (a) z = 1.3 m (4.3 ft), (b) z = 2.5 m (8.2 ft), (c) z = 3.7 m (12.1 ft), and (d) z = 4.9 m (16.1 ft).

pad to the average vertical stress $\sigma_v|_{rf,m}$ measured along the base of the reinforced fill [$\sigma_v|_{rf,m}$ is the average of the vertical stresses measured by the pressure cells located along both sections 1 and 2 at z = 4.9 m (16.1 ft) and x = 2.4 m (8 ft), 4.0 m (13 ft), 5.5 m (18 ft), and 7.0 m (23 ft)]. Given the small difference in elevation [≈ 0.2 m (8 in.)] between the pressure cells at the base of the leveling pad and those near the base of the reinforced fill (Figure 2.11a), the average vertical stress $\sigma_v|_{rf,m}$ from the fill pressure cells was increased by 4 kPa (83.5 psf) when calculating the vertical stress ratio to account for the added backfill weight. From Figure 3.3, we see that that the vertical stress ratio $\sigma_v|_{lp,m}$ / $\sigma_v|_{rf,m}$ increases nonlinearly at a decreasing rate with the wall construction stages. For stage 1 of wall construction, the vertical stress at the base of the leveling pad is 57% greater than that measured along the base of the reinforced fill. The values of the vertical stress ratio range from 1.85 to 1.98 for stages 2 to 4 of wall construction. At the end of wall construction (stage 5), the vertical stress at the base of the leveling pad is twice that measured along the base of the reinforced fill. Given that the diameter of the pressure cell covers approximately 77% of the width of the leveling pad, the vertical stress measured by the pressure cell may be thought of as a "representative" or "average" stress underneath the pad.

It is also of interest to compare the vertical stress $\sigma_v|_{lp,m}$ measured at the base of the leveling pad to that calculated based on the self-weight of the wall facing. The vertical stress $\sigma_v|_{lp,c}$ at the base of the leveling pad

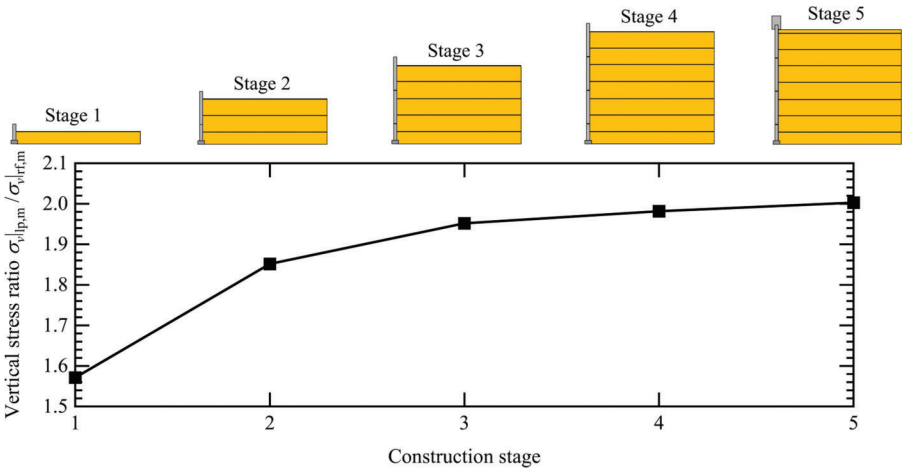

Figure 3.3 Evolution of the vertical stress ratio $\sigma_v|_{lp,m}$ / $\sigma_v|_{rf,m}$ during wall construction.

due to the self-weight of the wall facing is calculated using the relationship: $\sigma_v|_{lp,c} = \Sigma W/(B_{lp}L_R)$; where W [$= \gamma_c bhL_R$] = weight of each component of the wall facing; B_{lp} = width of the leveling pad; L_R = reference length [= 1 m (3.28 ft)]; and γ_c, b, and h = unit weight, width, and height of each component of the wall facing. The facing components considered in the calculation of $\sigma_v|_{lp,c}$ include the leveling pad, the four rows of facing panels, and the coping. Figure 3.4a shows the evolution of the measured and calculated vertical stresses $\sigma_v|_{lp,m}$ and $\sigma_v|_{lp,c}$ at the base of the leveling pad during construction of the MSE wall. Regardless of the wall construction stage, we see that the vertical stress measured at the base of the leveling pad is always greater than that calculated based on the self-weight of the wall facing; the differences between the values of $\sigma_v|_{lp,m}$ and $\sigma_v|_{lp,c}$ increase with the progression of construction of the MSE wall. The additional vertical stresses transferred to the leveling pad may be attributed to (1) downward interface shear stresses mobilized between the back of the precast concrete panels and the reinforced fill material, and (2) downdrag forces generated at the connections between the steel strips and the facing panels; both of which occur due to relative movement between the reinforced fill and the wall facing, as illustrated by Damians et al. (2013, 2016).

To quantify the differences between the values of $\sigma_v|_{lp,m}$ and $\sigma_v|_{lp,c}$, we plot the ratio of these quantities in Figure 3.4b as a function of the wall construction stages. The vertical stress ratio $\sigma_v|_{lp,m}$ / $\sigma_v|_{lp,c}$ increases from a value of 1.6 at stage 1 of wall construction to values ranging from 2.1 to 2.6 for stages 2 to 4 and then decreases slightly to a value of 2.4 at the end of wall construction (stage 5). Because the main difference between stage 4 and stage 5 of wall construction is primarily the installation of the coping on top of the fourth row of facing panels, the values of both $\sigma_v|_{lp,m}$ and $\sigma_v|_{lp,c}$ increase from stage 4 to stage 5 by approximately the same amount (Figure 3.4a), thus resulting in a reduction in the vertical stress ratio between these construction stages. The practical implications of a vertical stress at the base of the leveling pad that is more than twice the stress due to the self-weight of the wall facing include (1) selection of a suitable width and grade of concrete for the leveling pad, and (2) proper compaction of the soil below and around the leveling pad. If the width of the leveling pad is insufficient and/or if the soil below it is weak or poorly compacted, a localized bearing capacity failure may result. The vertical stress ratio $\sigma_v|_{lp,m}$ / $\sigma_v|_{lp,c}$ (= 2.4) at the end of wall construction falls within the range of 1.8–2.8 reported in the literature for the "vertical load factor" based on the results of three full-scale [H = 6.0–16.9 m (20–55 ft)], instrumented, steel strip-reinforced MSE walls (Bastick et al., 1993; Chida & Nakagaki, 1979; Runser, 1999; Runser et al., 2001). The vertical load factor is conceptually similar to the vertical stress ratio; it is defined as the ratio of the total vertical load at the base of the facing panel units (obtained from load cell data) to the self-weight of the facing panels (Damians et al., 2013).

The instrumentation used in this study cannot detect the shear stresses mobilized along the facing-soil interface. However, based on the lateral stresses measured on the back of the wall facing at the end of wall construction (stage 5) and the assumption that the angle of wall friction δ has fully mobilized to its value δ_c at critical state, the critical-state interface shear stress τ_c (= $\sigma'_h \tan\delta_c$) can be plotted along the back of the wall facing at the end of wall construction (Figure 3.5). The lateral effective stress σ'_h was determined by taking the average of the lateral stresses (at each elevation) measured by the pressure cells installed in both sections 1 and 2 on the back of the wall facing. Following Kim and Salgado (2008), the critical-state interface friction coefficient $\tan\delta_c$ (considering plane-strain conditions) is estimated to be of the order of 0.5 for a rough interface. Integrating the shear stress distribution shown in Figure 3.5 across the height of the wall facing (per unit length of wall) results in a total vertical (downward) shear force F_s of 32.6 kN (7.3 kips). Dividing the value of F_s by the contact area (= $B_{lp}L_R$) of the base of the leveling pad leads to a vertical stress of 107 kPa (2,235 psf), which corresponds to 56% of the vertical stress

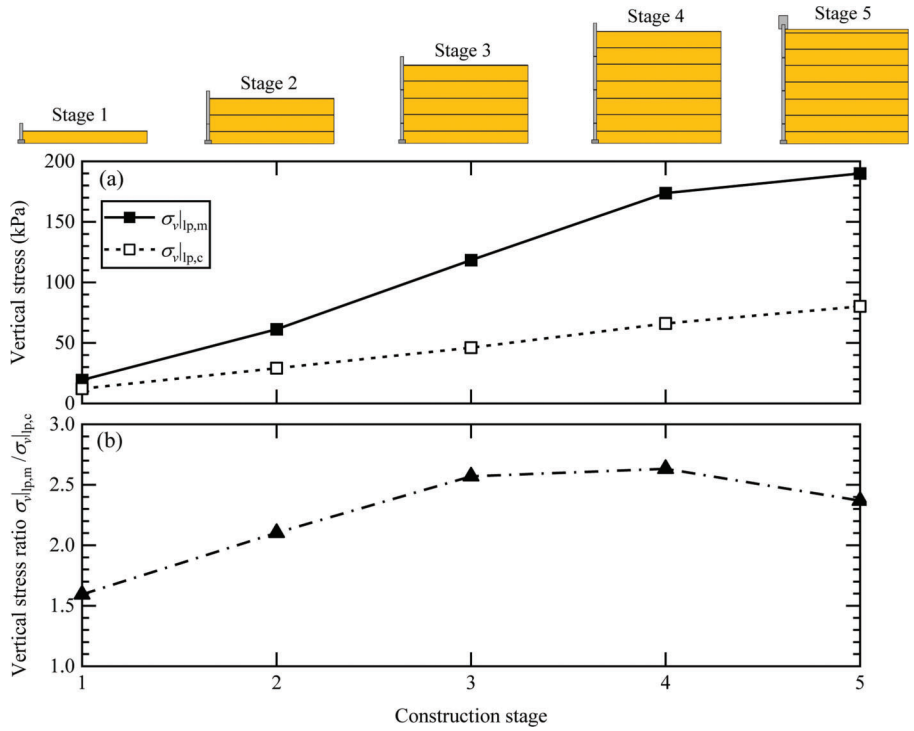

Figure 3.4 Evolution of (a) vertical stresses $\sigma_v|_{lp,m}$ and $\sigma_v|_{lp,c}$, and (b) vertical stress ratio $\sigma_v|_{lp,m}$ / $\sigma_v|_{lp,c}$ during wall construction.

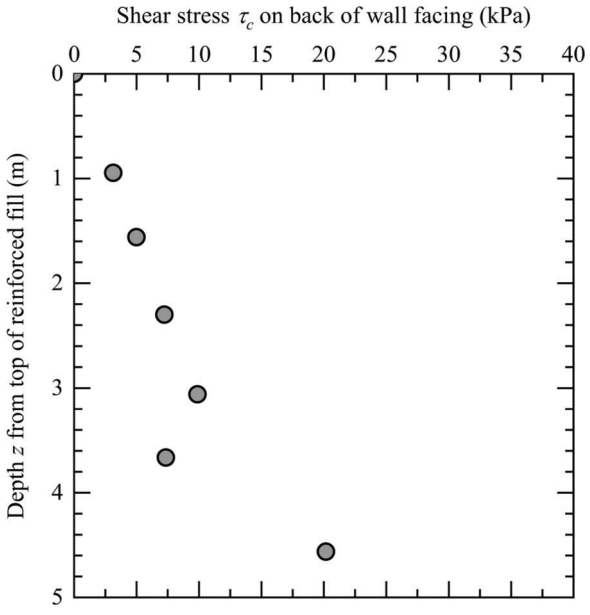

Figure 3.5 Shear stress distribution along the back of the wall facing at the end of wall construction.

$\sigma_v|_{lp,m}$ [= 190 kPa (3,968 psf)] measured by the pressure cell at the base of the leveling pad at the end of wall construction; B_{lp} = width of the leveling pad [= 0.3 m (1 ft)], and L_R = reference length [= 1 m (3.3 ft)]. Given that the vertical stress at the base of the leveling pad due to the self-weight of the wall facing is of the order of 80 kPa (1,671 psf) (corresponding to 42% of $\sigma_v|_{lp,m}$), the balance of the vertical stress [≈ 3 kPa (62 psf) (or 2% of $\sigma_v|_{lp,m}$)] at the base of the leveling pad may be attributed to the transfer of some reinforcement-facing connection downdrag forces to the leveling pad. These calculations provide a quantitatively reasonable explanation for the increased vertical stresses measured by the pressure cell at the base of the leveling pad.

3.2 Lateral Stresses

The lateral effective stress σ'_h acting on the back of the wall facing is equal to the product of the lateral earth pressure coefficient K_r and the vertical effective stress σ'_v. Given the absence of pore water pressure u in the reinforced fill, the stresses measured by the earth pressure cells are approximately equal to the effective stresses in the backfill soil. The coherent gravity method, the simplified method, and the simplified stiffness method require as input the peak friction angle ϕ_p of the reinforced fill material (determined from either direct shear or drained triaxial compression test results), with the caveat that ϕ_p be limited to a maximum value of 40° (AASHTO, 2020). However, direct shear and triaxial compression test results do not produce the same value of friction angle (Bareither et al., 2008; Han et al., 2018; Maccarini, 1993; Rowe, 1969; Thurairajah, 1962). Based on the results of direct shear tests performed in this study on dense samples of the reinforced fill material at a normal stress of 100 kPa (2,089 psf) (Figure 2.7a), the peak shear stress τ_p and the peak friction angle ϕ_p are equal to 81.3 kPa (1,698 psf) and 39.1°. Given that the vertical stresses measured by the pressure cells near the base of the reinforced fill are of the order of 90–100 kPa (1,880–2,089 psf) at the

end of wall construction (Figure 3.1d and Figure 3.2d), the value of ϕ_p at higher elevations (shallower depths) within the reinforced fill will be greater than 39.1° due to the greater contribution of dilatancy towards the peak shear strength of dense sand at lower confining stress levels. However, because the peak friction angle of the reinforced fill material must be capped at 40° (AASHTO, 2020), we set $\phi_p = 40°$ to calculate the lateral effective stresses acting on the back of the facing panels using the coherent gravity method and the simplified method. In the absence of direct shear or triaxial compression test results, AASHTO (2020) recommends the use of a peak soil friction angle equal to 34° for internal stability design of MSE walls. The internal stability design of the Whitestown MSE wall was done by RECo using the coherent gravity method with a peak friction angle of 34° and a soil unit weight of 18.85 kN/m^3 (120 pcf).

Figure 3.6 shows that the lateral stresses calculated using the simplified method are greater than those obtained using the coherent gravity method by about 8–10% for $\phi_p = 34°$ and 4%–9% for $\phi_p = 40°$, depending on the depth z from the top of the reinforced fill. The simplified stiffness method was not included in Figure 3.6 because the method was primarily developed to calculate the maximum tensile load T_{max} in the reinforcement; the method does not provide a formulation for K_r and σ'_h explicitly. The measured lateral stresses on the back of the facing panels at the end of wall construction are in good agreement with predictions obtained using the coherent gravity and simplified methods (with $\phi_p = 40°$), particularly in the upper half of the wall [$z \leq 2.3$ m (7.5 ft)]. However, if we set

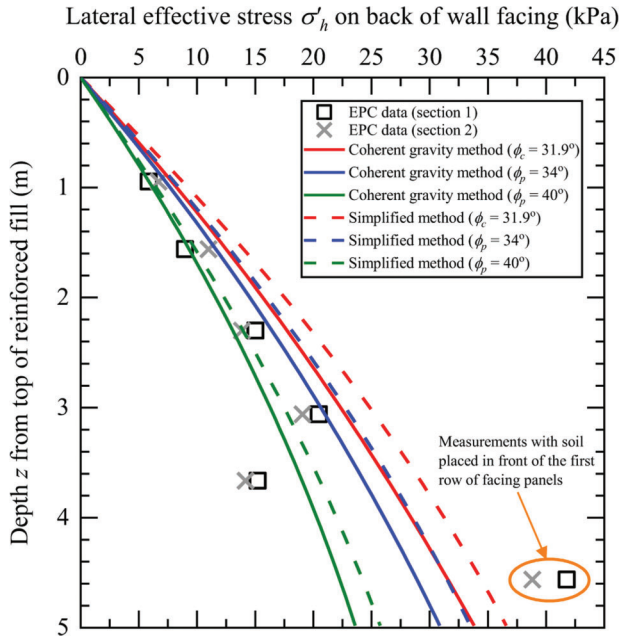

Figure 3.6 Comparison between the predicted and measured distributions of lateral stresses acting on the back of the facing panels at the end of wall construction.

$\phi_p = 34°$, the value recommended by AASHTO (2020) in the absence of laboratory test results, the values of σ'_h calculated using the coherent gravity method and the simplified method are generally higher than those measured by the pressure cells. This illustrates the sensitivity of these methods to the value of ϕ_p used to calculate K_r, and, consequently, σ'_h. Predictions of σ'_h obtained using the critical-state friction angle ϕ_c (= 31.9°) of the reinforced fill material, although conservative in the short term (i.e., end of wall construction), may be applicable for the design of MSE walls in the long term (i.e., throughout their entire service life), as discussed later in the report.

The lateral stresses measured on the back of the facing panels increase from 6 kPa (125 psf) near the top of the wall [$z = 0.9$ m (3 ft)] to about 40 kPa (835 psf) near the bottom of the wall [$z = 4.6$ m (15.1 ft)]. The considerably high lateral stresses measured on the back of the wall facing near the bottom of the wall may be attributed to the placement of compacted sandy soil in front of the wall during construction (Figure 2.2). The passive resistance provided by the soil placed in front of the wall likely reduced the lateral displacement of panel 1, resulting in the mobilization of higher lateral stresses on the back of panel 1 than would be expected in the absence of the passive resistance. Nonetheless, the nonlinear depth profile of the lateral stress measured on the back of the facing panels at the end of wall construction [ignoring the two data points at $z = 4.6$ m (15.1 ft)] indicates a reduction in lateral stress towards the bottom of the wall, likely due to potential arching effects in the backfill soil (Desai & El-Hoseiny, 2005, 2007; Handy, 1985, 2007; Paik & Salgado, 2003).

3.3 Reinforcement Loads

The design methods summarized in Table 1.1 are intended to predict the maximum reinforcement tensile load T_{max} (in units of force per unit length of wall in the longitudinal direction) at the end of wall construction. In these methods, T_{max} is a function of the tributary vertical spacing s_v of the reinforcement (AASHTO, 2020; FHWA, 2009a). For the Whitestown MSE wall, the value of s_v is equal to 0.77 m (2.53 ft) for the first reinforcement layer counted from the bottom of the wall, 0.75 m (2.46 ft) for the second through sixth reinforcement layers, and 0.47 m (1.54 ft) for the seventh (topmost) reinforcement layer.

3.3.1 Distribution of Reinforcement Tensile Loads

The tensile load T in the reinforcement (in units of force per unit length of wall in the longitudinal direction) at a given strain gauge (SG) location was determined using the relationship: $T = \varepsilon E_s A_s / s_h$, where ε = measured strain in the reinforcement at the gauge location (averaged between the top and bottom strain gauges), E_s = Young's modulus of steel [= 200 GPa (29,000 ksi)], A_s = cross-sectional area of the steel strip [= 0.0002 m^2 (0.31 in.^{2})], and s_h = horizontal spacing of

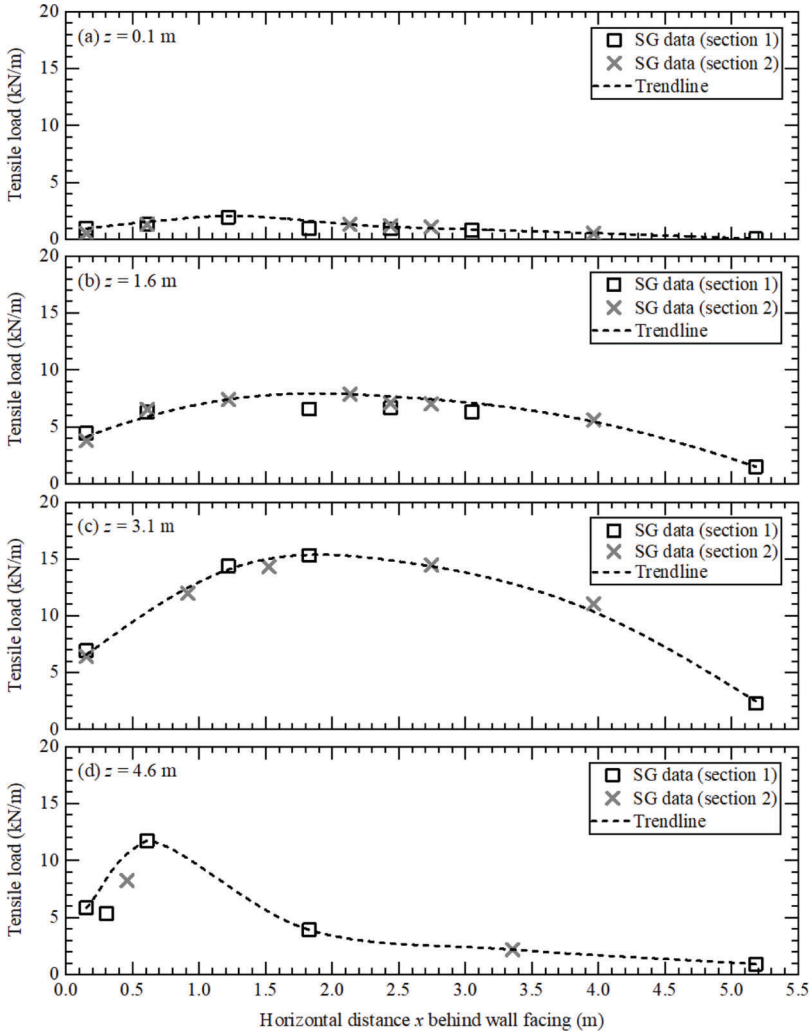

Figure 3.7 Distribution of the reinforcement tensile loads behind the wall facing at the end of wall construction: (a) z = 0.1 m (0.3 ft), (b) z = 1.6 m (5.25 ft), (c) z = 3.1 m (10.2 ft), and (d) z = 4.6 m (15.1 ft).

the steel strips [= 0.75 m (2.46 ft)]. Figure 3.7 shows the distribution of the reinforcement tensile loads for each of the four levels of instrumented steel strips at the end of wall construction. The tensile loads determined from the strain gauges installed in section 1 were generally consistent and close to those obtained from the gauges installed in section 2. The tensile load in each instrumented strip increases from a non-zero value T_{con} near the reinforcement-panel connection to a maximum value T_{max} behind the wall facing and then approaches zero near the free end of the reinforcement. Regardless of the elevation of the steel strip, we see that the measured values of T_{con} are less than T_{max}; this is consistent with observations from other full-scale, instrumented, steel strip-reinforced MSE walls reported in the literature (Christopher et al., 1990; Runser et al., 2001; Stuedlein et al., 2012). For the four instrumented levels of steel strips [located at z = 0.1 m (0.3 ft), 1.6 m (5.25 ft), 3.1 m (10.2 ft), and 4.6 m (15.1 ft)] considered in this study, the values of T_{con} at the end of wall construction are 1.1 kN/m (75 lb/ft), 4.1 kN/m (281 lb/ft), 6.7 kN/m (459 lb/ft), and 5.9 kN/m (404 lb/ft); while those for T_{max} are 1.9 kN/m (130 lb/ft), 7.9 kN/m (541 lb/ft), 15.3 kN/m (1,048 lb/ft), and 11.7 kN/m (802 lb/ft), respectively. The ratio T_{con}/T_{max} ranges from 0.4–0.6, which is less than the value of 1.0 recommended by AASHTO (2020) for use in reinforcement-facing connection design.

The maximum tensile stresses $\sigma_{t,max}$ in the four instrumented levels of steel strips at the end of wall construction range from 12–58 MPa (251–1,211 ksf), corresponding to 2%–12% of the yield strength f_y of grade 65 steel [= 491 MPa (10,255 ksf), on average, based on the analysis of 90 tensile test results for steel strip reinforcements (Kim, 2008; Kim & Salgado, 2012b)]. This range of tensile stresses is much smaller than the allowable tensile stress $\sigma_{t,all}$ of 270 MPa (5,639 ksf) ($\approx$ 55% of f_y) calculated for a factor of safety FS = 1.82 (AASHTO, 1996) against rupture (breakage) of the reinforcement.

3.3.2 Reinforcement Length in Active Zone

Kim and Salgado (2012b) assessed the uncertainty of the locus of T_{max} using data from Schlosser and Segrestin (1979) and obtained the distribution of L_a from reliability analyses for different values of target reliability index β_T (= 2.0, 2.33, and 3.0). Figure 3.8 compares the predicted and measured profiles of the normalized reinforcement length L_a/H within the active zone versus the normalized depth z/H from the top of the reinforced fill at the end of wall construction. In the lower half of the wall, the values of L_a determined from the strain gauge measurements (considering data from both Sections 1 and 2) are greater than those obtained from both AASHTO (2020) and Kim and Salgado (2012b). For example, the measured values of L_a are 53% and 21% greater than those obtained by Kim and Salgado (2012b) (β_T = 3.0) for the first and third reinforcement levels (z/H = 0.92 and 0.62) counted from the bottom of the wall. In the upper half of the wall, however, the values of L_a determined from the strain gauge data are close to the predicted L_a distributions of Kim and Salgado (2012b), with the AASHTO line plotting between the measured data points. The results in Figure 3.8 suggest that it would be prudent to design steel strip-reinforced MSE walls for a higher target reliability index (e.g., β_T = 3.0 instead of 2.0), i.e., for a lower target probability of failure.

3.3.3 Maximum Tensile Load in Reinforcement

Predictions of T_{max} using the coherent gravity, simplified, and simplified stiffness methods were made considering three different values of friction angle: (1) $\phi_c = 31.9^\circ$, (2) $\phi_p = 34^\circ$ [the default value stipulated by AASHTO (2020) in the absence of direct shear or triaxial compression test results for the backfill soil], and (3) $\phi_p = 40^\circ$ [based on the direct shear test results obtained in this study, but capped at 40° as per AASHTO (2020)]. Note that the friction angle that appears in the equations for these methods is defined as either the peak friction angle in direct shear or the peak friction angle in triaxial compression (AASHTO, 2020; Allen et al., 2001; Allen & Bathurst, 2015, 2018). This somewhat flexible definition in terms of test type and stress level adds to some uncertainty in the value of ϕ_p that goes into the equations of these methods to calculate T_{max}. For the simplified stiffness method, the values of J and S_{global} are calculated as 53 MN/m and 74 MPa, thus resulting in a global stiffness factor Φ_g equal to 0.89. Because the computed value of the facing stiffness factor Φ_{fs} exceeded 1.0, it was set equal to 1.0 [as per Allen and Bathurst (2015)] in the calculation of T_{max} using the simplified stiffness method.

From Figure 3.9a, we see that the simplified stiffness method (with $\phi_p = 40^\circ$) provides the best estimate of T_{max} for the four instrumented levels of steel strips at the end of wall construction. The coherent gravity and

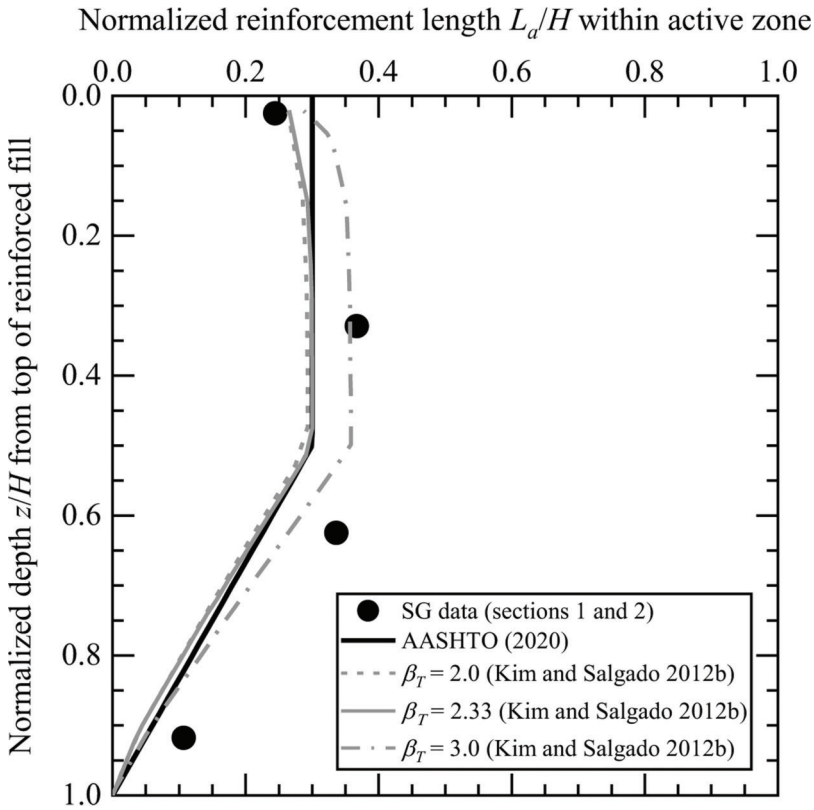

Figure 3.8 Comparison between the predicted and measured profiles of L_a/H with the normalized depth z/H from the top of the reinforced fill at the end of wall construction.

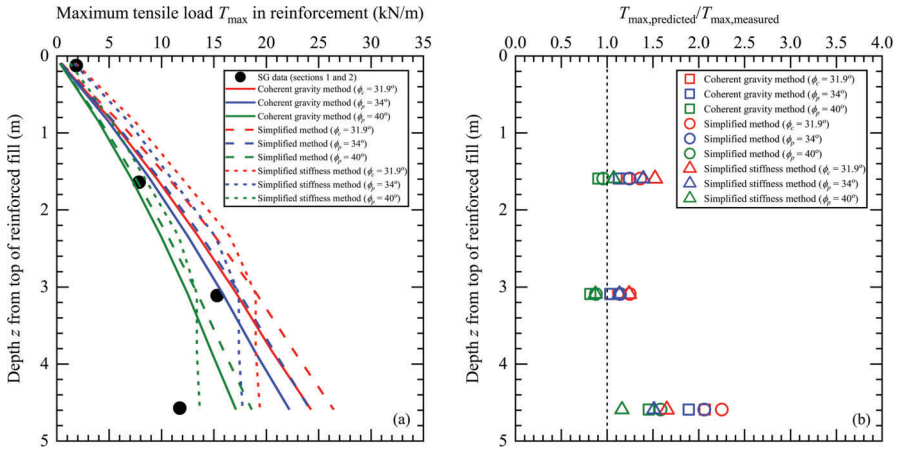

Figure 3.9 Maximum tensile load T_{max} in the reinforcement at the end of wall construction: (a) comparison between the predicted and measured profiles of T_{max} with depth z from the top of the reinforced fill, and (b) ratio of predicted-to-measured values of T_{max}.

simplified methods (with $\phi_p = 40°$) provide good predictions of T_{max} for the fifth reinforcement level [z = 1.6 m (5.25 ft)]; however, these methods underpredict T_{max} for the seventh and third reinforcement levels [z = 0.1 m (0.3 ft) and 3.1 m (10.2 ft)] and significantly overpredict T_{max} for the first reinforcement level [z = 4.6 m (15.1 ft)] counted from the bottom of the wall. All three design methods are sensitive to the value of ϕ_p used to calculate T_{max} at the end of wall construction; the methods generally overpredict the maximum reinforcement tensile loads for $\phi_p = 34°$.

Figure 3.9b quantifies the ratio of the predicted T_{max} to the measured T_{max} for each instrumented steel strip at the end of wall construction. The T_{max} data point for the topmost reinforcement level was excluded because the design methods were generally calibrated against a database of full-scale, instrumented, steel strip-reinforced MSE walls for which the height of reinforced fill above the topmost reinforcement level (excluding any surcharge) was of the order of 0.38 m (1.25 ft) at the end of wall construction (Allen et al., 2001); some MSE walls in the database also had uniform surcharge loads ranging from 24–72 kPa (500–1,500 psf) on top of the walls. For the Whitestown MSE wall, the reinforced fill material was not placed up to the top of the coping because the pile cap was constructed later on top of the reinforced fill at the surface elevation corresponding to stage 5. Therefore, for the Whitestown MSE wall, the height of reinforced fill above the topmost reinforcement level was approximately 0.1 m (0.3 ft) at the end of wall construction, which is much smaller than the typical value of 0.38 m (1.25 ft). Figure 3.9b shows that the design methods generally produce good estimates of the maximum reinforcement tensile loads at the end of wall construction (with $T_{max,predicted}/T_{max,measured}$ ranging from 0.8 to 1.4), except near the bottom of the wall, where the value of $T_{max,predicted}/T_{max,measured}$ is in the range of 1.5–2.0 for the coherent gravity and simplified methods, with higher values corresponding to the use of lower backfill soil peak friction angles (e.g., $\phi_p = 34°$).

The coherent gravity method, the simplified method, and the simplified stiffness method have been calibrated specifically for MSE walls at the end of construction, i.e., under initial operational conditions. However, during the service life of an MSE wall, repeated loading cycles due to traffic and other events (e.g., earthquakes and rainstorms) may degrade the peak shear strength of the reinforced fill progressively (cycle by cycle) over time in terms of either a partial or complete loss of dilatancy (Take et al., 2004), resulting in (1) a decrease in the peak soil friction angle ϕ_p towards the critical-state friction angle ϕ_c (Bolton, 1986, 1996), and (2) an increase in the tensile loads in the reinforcement due to an increase in the lateral earth pressure coefficient. This suggests that it would be prudent to use ϕ_c in the design of MSE walls, because it best represents the level of shear strength that will be available for their entire service life, neglecting the contribution that may come from the dilative component of soil shear strength that will degrade as shear bands form (Bolton, 1991a; 1991b; Bolton & Pang, 1982) or that may, as discussed above, degrade over time. The design methods that we used to estimate T_{max} are based on K_A calculated using the Rankine method. The Rankine method does not account for wall friction, as some methods proposed for traditional retaining walls do (Coulomb, 1776; Lancellotta, 2002; Paik & Salgado, 2003). However, some of the effects of friction degradation over time can be captured through a higher calculated value of K_A.

3.3.4 Lateral Earth Pressure Coefficient

The maximum tensile load T_{max} that develops in a given reinforcement layer is due to the lateral effective stress σ'_h ($= K_r\sigma'_v$) acting on the back of the wall facing over the tributary area of the reinforcement (Bathurst, 2014; Kim & Salgado, 2012b; Salgado, 2022). On this basis, the lateral earth pressure coefficient K_r can be determined from the reinforcement strain gauge data using the relationship: $K_r = T_{max}/(\gamma z s_v)$. Figure 3.10

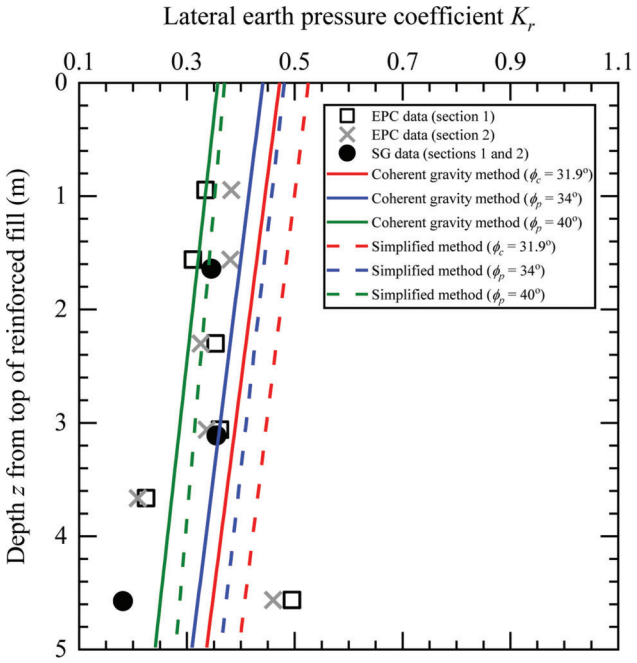

Figure 3.10 Comparison between the predicted and measured profiles of K_r with depth z from the top of the reinforced fill at the end of wall construction.

shows that the values of K_r determined from both the earth pressure cell and reinforcement strain gauge data are generally in the range of 0.18 to 0.38, and that the simplified method (with $\phi_p = 34°$) provides upper-bound estimates of K_r in comparison to the measured data points. The values of K_r calculated using the simplified method are greater than those obtained using the coherent gravity method; the differences in the values of K_r obtained using the coherent gravity method and the simplified method range from 9%–17% for $\phi_p = 34°$ and 3%–16% for $\phi_p = 40°$, depending on the depth z from the top of the reinforced fill. Predictions of K_r obtained using coherent gravity and simplified methods with $\phi_c = 31.9°$ are provided for completeness.

The values of K_r determined from the earth pressure cell (EPC) data are in good agreement with those obtained from the reinforcement strain gauge (SG) measurements (considering data from both sections 1 and 2), except for the bottommost reinforcement level. The lateral displacement of the bottommost facing panel (panel 1) was likely restricted by the passive resistance provided by the compacted sandy soil placed in front of the wall, thus resulting in the buildup of lateral stresses on the back of panel 1, and, consequently, a high K_r value ($\approx$ 0.48). On the other hand, the development of tensile load in the reinforcement depends on the level of displacement of the steel strip, which, in turn, depends on the lateral displacement of the facing panel to which the strip is connected. The smaller the lateral displacement of the facing panel, the smaller the maximum tensile load in the reinforcement is likely to be, hence the low K_r value (= 0.18) determined from the strain gauge data for the bottommost reinforcement level. The value of K_r determined from the strain gauge data for the topmost reinforcement level was found to be unrealistically high (= 1.7), possibly due to the very low confining stress [$\approx$ 2 kPa (0.3 psi)] operative on the reinforcement and was thus excluded from the comparison in Figure 3.10.

3.3.5 Soil-Reinforcement Friction Coefficient

The soil-reinforcement friction coefficient μ^*_{mob} mobilized at the end of wall construction can be determined from the distribution of the tensile load along the reinforcement using:

$$\mu^*_{mob} = \frac{\tau_{mob}}{\sigma'_v} = \frac{T_i - T_j}{2b_r L_{ij}\gamma z} \qquad \text{(Eq. 3.1)}$$

where T_i and T_j = reinforcement tensile loads (in units of force) corresponding to two adjacent points i and j along the trendline plotted in Figure 3.7, τ_{mob} = shear resistance mobilized along the top and bottom surfaces of the reinforcement between points i and j, b_r = width of the reinforcement, L_{ij} [= $x_i - x_j$] = distance between points i and j, and σ'_v [$\approx \gamma z$] = vertical effective stress acting on the surface area of the reinforcement between points i and j. The trendline provides a smooth and continuous distribution of the tensile load T in the reinforcement at the end of wall construction (Figure 3.7); the first derivative $\partial T/\partial x$ of the trendline is equal to zero at the location of T_{max}. The mobilized friction along a segment of the reinforcement depends on the change in T between the two points that make up that reinforcement segment; the smaller the change in T for a given reinforcement length, the smaller the mobilized friction coefficient is.

Figure 3.11 shows the distribution of μ^*_{mob} for each of the four levels of instrumented steel strips at the end of wall construction. Positive and negative values of μ^*_{mob} correspond to the soil-reinforcement interface shear stresses mobilized in the active zone and resisting zone, respectively. The values of the ultimate pullout resistance coefficient μ^*_{ult} recommended by AASHTO (2020) for calculation of ultimate pullout resistance (in the absence of pullout test results) and the allowable pullout resistance coefficient $\mu^*_{all}(=\mu^*_{ult}/FS)$, with FS = factor of safety against pullout [typically equal to 1.5 (Salgado, 2022; Schlosser & Bastick, 1991)], are plotted in Figure 3.11 over the effective reinforcement length L_e determined according to AASHTO (2020). For the Whitestown MSE wall (C_U = 3.45 and $\phi_p = 40°$), the values of μ^*_{ult} determined from AASHTO (2020) (Eq. 1.20) for the four instrumented levels of steel strips [located at z = 0.1 m (0.3 ft), 1.6 m (5.25 ft), 3.1 m (10.2 ft), and 4.6 m (15.1 ft)] are equal to 1.72, 1.49, 1.27, and 1.05, respectively. From Figure 3.11, we see that the values of μ^*_{mob} calculated using Eq. 3.1 are not constant along the reinforcement, indicating that soil-reinforcement interface friction does not mobilize uniformly along the reinforcement at the end of wall construction. The value of μ^*_{mob} is equal to zero at the location of

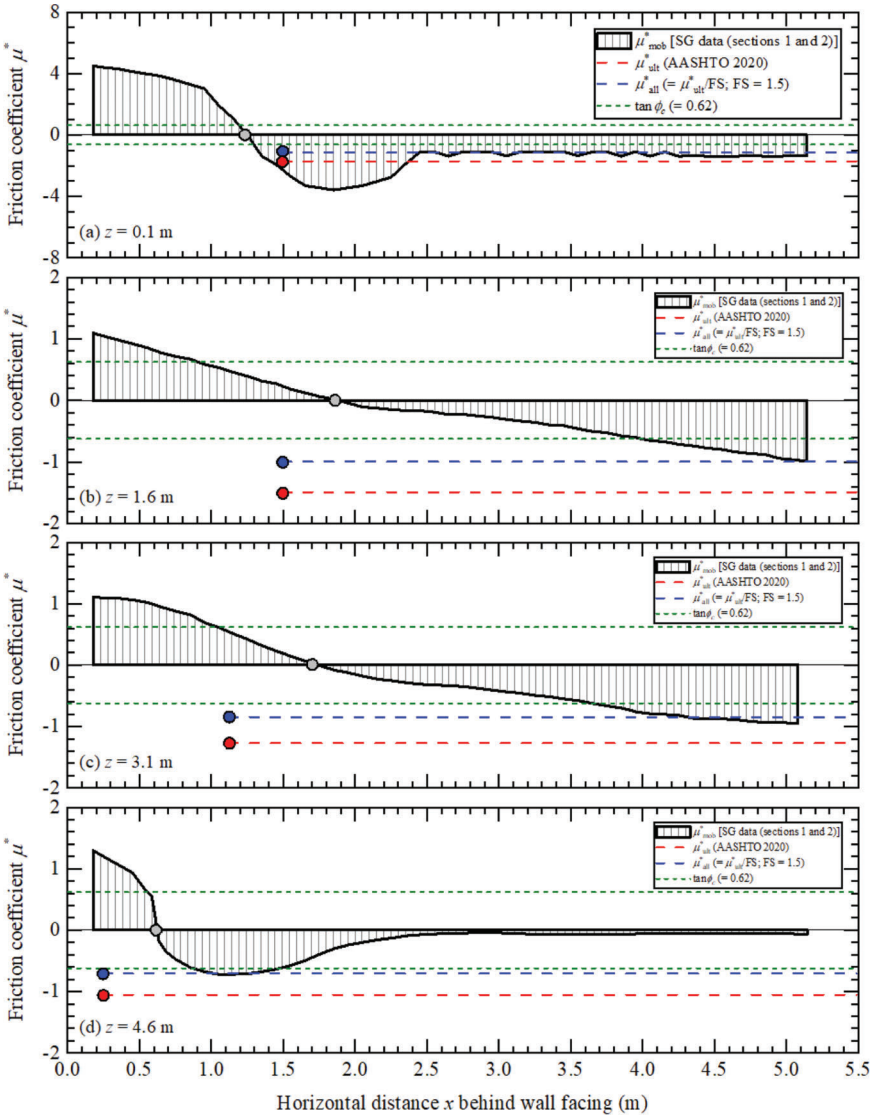

Figure 3.11 Distribution of the mobilized soil-reinforcement friction coefficient at the end of wall construction: (a) z = 0.1 m (0.3 ft), (b) z = 1.6 m (5.25 ft), (c) z = 3.1 m (10.2 ft), and (d) z = 4.6 m (15.1 ft).

T_{max} (indicated by the grey circle in Figure 3.11) because, at that location, an element of the steel strip is being pulled on either side by an equal and opposite force equal to T_{max}, resulting in $\delta T = 0$, and, consequently, zero mobilized friction there. The red and blue circles in Figure 3.11 (red for μ^*_{ult} and blue for μ^*_{all}) represent the locations of T_{max} as predicted by AASHTO (2020). In the vicinity of T_{max} (i.e., near the zone of the expected shear "failure" surface) determined in this study, the values of μ^*_{mob} are less than the critical-state friction coefficient $\tan\phi_c$ (= 0.62) of the reinforced fill material; this suggests that, within this zone, the reinforcement may not have moved enough for the soil-reinforcement frictional resistance to fully mobilize.

The pattern of μ^*_{mob} is different depending on the elevation of the steel strip. For example, for the bottommost reinforcement level, the mobilized friction coefficient is negligible along a significant portion [≈ 2.5 m (8.2 ft)] of the reinforcement length in the resisting zone (Figure 3.11d), whereas for the other instrumented reinforcement levels, the friction coefficient has mobilized to values approaching $\tan\phi_c$ along some of the reinforcement length in the resisting zone (Figure 3.11a–c). The maximum values of μ^*_{mob} measured in the resisting zone (= 0.7–1.0) are in good agreement with the values of μ^*_{all} (calculated for FS = 1.5), except for the topmost reinforcement level, where the maximum value of μ^*_{mob} (= 3.6) in the resisting zone is greater than that of μ^*_{all} (= 1.2). A direct one-to-one comparison between the values of μ^*_{mob} and μ^*_{ult} cannot be made because the values of μ^*_{mob} correspond to an MSE wall at the end of construction (under initial operational conditions) and not for a wall that has

reached an ultimate limit state (for which μ^*_{ult} would be applicable in the context of a reinforcement pullout ultimate limit state check). Frictional resistance would be fully mobilized along the entire length of the reinforcement in the resisting zone only when the steel strip is pulled out in an ultimate limit state.

The vertical axis of Figure 3.11a was plotted with a scale different from those of Figure 3.11b–d in order to reflect the high values of μ^*_{mob} ($\approx$ 3–5) obtained for the topmost reinforcement level. In fact, values of μ^*_{ult} as high as 8–9 have been reported in the literature based on pullout test results for ribbed steel strip reinforcements installed in backfill materials ranging from silty sands to coarse gravels (AASHTO, 1994; Kim, 2008; Kim & Salgado, 2012b; Schlosser & Bastick, 1991). The pullout resistance coefficient decreases with increasing overburden pressure due to the suppression of dilatancy (Balunaini & Prezzi, 2010; Miyata & Bathurst, 2012b; Strahler et al., 2016), with the consequence that soil-reinforcement shear resistance is then derived mainly through friction. The interface friction angle between steel and sand at critical state can be determined as a function of the sand properties (D_{50}, ϕ_c) and the normalized surface roughness of steel using the methodology developed by Han et al. (2018, 2019); the methodology is based on the results of direct interface shear tests performed on sands with different particle sizes, morphologies, and gradations and steel surfaces with different levels of rusting.

3.4 Lateral Displacements

3.4.1 Lateral Displacement of the Wall Facing and the Reinforced Fill

Figure 3.12 shows the outward lateral displacement profiles of the wall facing and the reinforced fill measured 5 days after the end of wall construction. The maximum lateral displacement of the wall facing is 10 mm (0.4 in.), corresponding to 0.2% of the height of the reinforced fill, and occurs at a depth of 3 m ($\approx$ 10 ft) below the top of the reinforced fill. The lateral displacement within the reinforced fill [2.5 m (8.2 ft) behind the wall facing] is smaller than that measured just behind the facing [at x = 0.1 m (4 in.)], with a maximum value of 5.5 mm (0.22 in.) or approximately 0.1% of the reinforced fill height. AASHTO (2020) provides a chart to estimate the maximum lateral displacement of the wall facing that may occur during wall construction as a function of the reinforcement length-to-wall height ratio L_r/H and the reinforcement type (i.e., extensible versus inextensible reinforcement) (Christopher, 1993; Mitchell & Christopher, 1990). For the Whitestown MSE wall (L_r/H = 1.1 with inextensible reinforcement), the predicted maximum lateral displacement of the wall facing using the AASHTO (2020) chart is 14.1 mm (0.56 in.), which is 41% greater than the measured value.

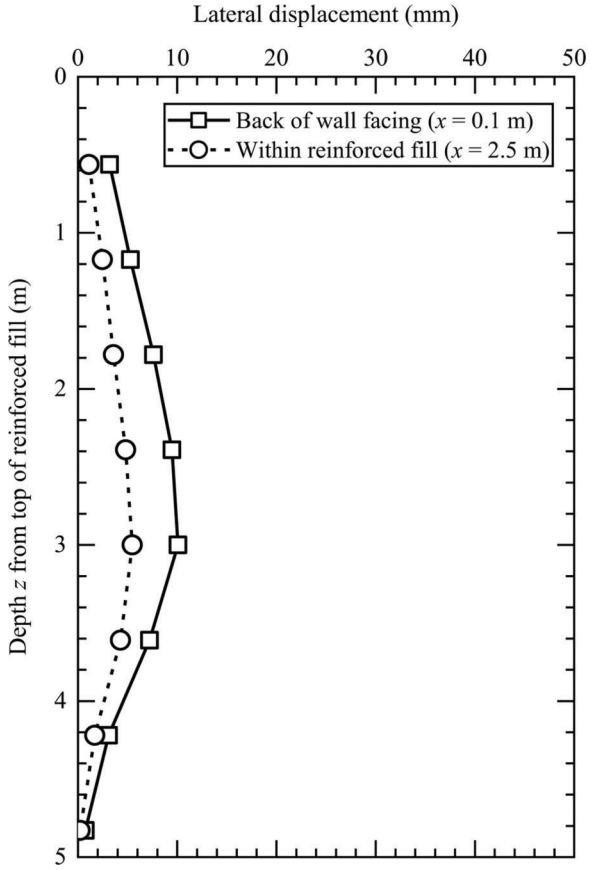

Figure 3.12 Outward lateral displacement profiles of the wall facing and the reinforced fill measured 5 days after the end of wall construction.

3.4.2 Horizontal and Vertical Joint Gap Width Between Facing Panels

Figure 3.13a and Figure 3.13b shows the evolution of the vertical and horizontal joint gap width between facing panels measured by the crackmeters during construction of the MSE wall. It can be observed from Figure 3.13a that (1) the values of vertical joint gap width measured by crackmeters CM-2 and CM-4 are generally consistent both during and after wall construction (indicating a uniform gap closure), reaching a value at the end of wall construction of 18.1 mm (0.71 in.), and (2) the vertical joint gap width measured by crackmeter CM-5 is about 0.5 mm (0.02 in.) less than that measured by crackmeter CM-3. The local oscillations in the joint gap measurements may be attributed to potential contraction/expansion of the precast concrete panels due to changes in temperature and the effects of construction-related activities (e.g., backfill compaction, operation of machinery, and movement of equipment in preparation for construction of the bridge abutment on top of the MSE wall).

Because crackmeters CM-1 and CM-6 were installed at the horizontal joints of facing panels 3 and 4 only after these panels were erected, they do not capture the

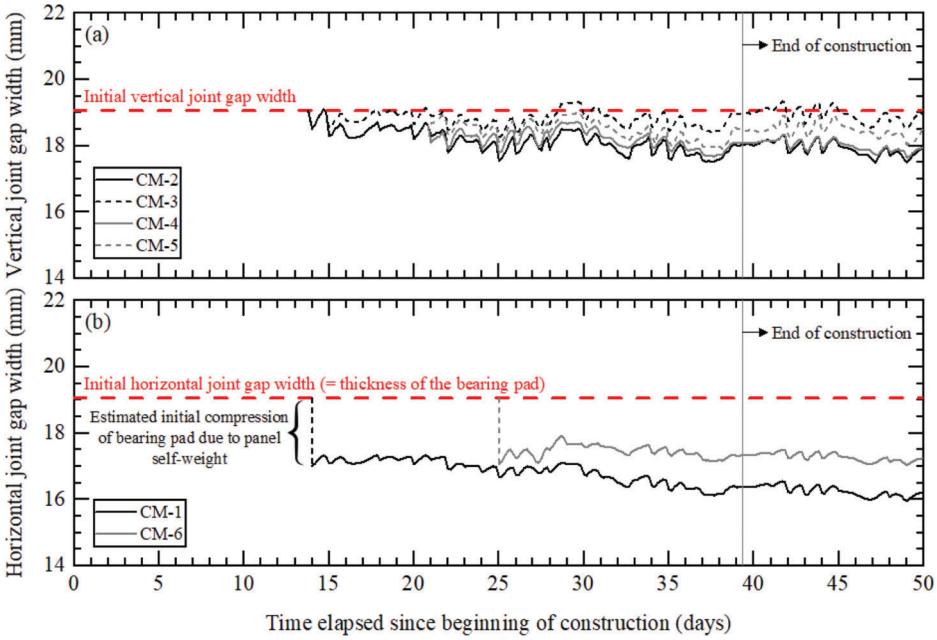

Figure 3.13 Evolution of the horizontal and vertical joint gap width between facing panels during and after wall construction.

initial compression of the bearing pad caused by the self-weight of the panels. Based on the panel dimensions and the unit weight of reinforced concrete, the self-weights of panels 3 and 4 are estimated to be 15.4 kN (3.46 kips) each. Given that each horizontal joint consists of two EPDM bearing pads, the vertical load transferred to each bearing pad due to the panel self-weight is equal to 7.7 kN (1.73 kips), resulting in an estimated initial joint compression of about 1.9 mm (0.075 in.) (Figure 2.9). Therefore, the estimated horizontal joint gap width (accounting for the initial compression of the bearing pads) is 17.1 mm (0.67 in.) by the time CM-1 and CM-6 were installed at their respective locations.

Figure 3.13b shows that the horizontal joint gap width measured by crackmeter CM-1 is less than that measured by crackmeter CM-6 both during and after wall construction, with values equal to 16.4 mm (0.65 in.) for CM-1 and 17.3 mm (0.68 in.) for CM-6 at the end of wall construction. These values are in good agreement with the range of values [$\approx$ 16–18 mm (0.6–0.7 in.)] reported by Damians et al. (2016) based on finite element simulations of a 6-m-(20-ft)-high, steel-reinforced MSE wall with two 20-mm-(0.8-in.)-thick EPDM bearing pads per horizontal joint. FHWA (2009a, 2009b) recommends a minimum horizontal and vertical joint gap width between adjacent facing panels equal to 12.5 mm (0.5 in.) after the wall has been constructed; the values determined from the crackmeter measurements satisfy this requirement. Given that the loads transferred to the bearing pads will increase as we move further down to the base of the wall facing, the horizontal joint gap width between panels 1 and 2 (Figure 2.12a) will be smaller than those between panels 2 and 3 (CM-1) and panels 3 and 4 (CM-6).

3.5 Vertical Displacements

As mentioned in Section 2.4.2 of Chapter 2, the horizontal inclinometer consists of a string of tilt sensor segments connected in series. The vertical displacement w_i of one end of a tilt sensor segment i of length L_i relative to the other end of the segment was determined using the relationship: $w_i = L_i(\Delta\sin\theta_i)$, where θ_i is the inclination of segment i with respect to the horizontal, and $\Delta\sin\theta_i$ represents the change in $\sin\theta_i$ between the initial (reference) and current configurations of segment i. The cumulative vertical displacement w of the MSE wall foundation at a given sensor location was calculated by summing the values of w_i obtained from all tilt sensor segments preceding the segment of interest (i.e., located to the east of the segment of interest) but also including the segment of interest.

Figure 3.14 shows that the cumulative vertical displacements along the base of the retained backfill are small [<5 mm (0.2 in.)], and most of the vertical displacements along the base of the MSE wall foundation occur near the leveling pad. For better visualization of the results, the location of the wall facing and the lateral extents of the reinforced fill, the retained backfill, and the soil placed in front of the facing are also shown in the figure (the height of the wall facing is not to scale). The maximum vertical displacement of the MSE wall foundation increases from 3 mm (0.12 in.) at stage 1 of wall construction to values ranging from 6 mm (0.24 in.) to 17 mm (0.67 in.) for stages 2 to 4, and, finally, to a value of 20 mm (0.8 in.) (or 0.4% of the height of the reinforced fill) at the end of wall construction (stage 5). The 3-mm (0.12-in.) vertical displacement observed for stage 1 of wall construction may be attributed to the immediate

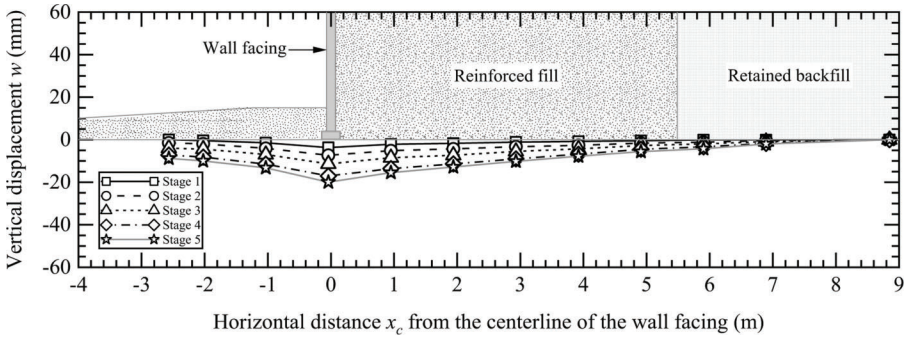

Figure 3.14 Vertical displacement profiles (displacements negative in the downward direction) of the MSE wall foundation for different stages of wall construction.

settlement of both the top 1.5-m-(5-ft)-thick layer of compacted sandy soil and the underlying 0.9-m-(3-ft)-thick layer of soft clay [$q_t \approx 0.3$ MPa (3 tsf)]. The outward lateral displacement of the wall facing during construction may also have contributed to the settlements measured along the base of the reinforced fill. The ratio of the maximum vertical displacement of the MSE wall foundation to the maximum lateral displacement of the wall facing is equal to 2 at the end of wall construction.

4. MONITORING DURING AND AFTER BRIDGE CONSTRUCTION

4.1 Loads in the Piles and Pile Cap

Figure 4.1 shows the evolution of the axial loads carried by the three instrumented piles (piles 11, 12, and 13) and the axial load within the instrumented zone of the pile cap during and after bridge construction; the construction stages listed in Table 2.1 are plotted in the figure for reference. The axial load Q_p carried by each instrumented pile was calculated by multiplying the average strain reading ε_{avg} (obtained from the pair of arc-weldable strain gauges installed near the pile head) by the axial stiffness E_sA_s of the pile; E_s = Young's modulus of steel, and A_s = steel cross-sectional area of the H-pile [= 0.0139 m^2 (21.5 in.^{2})]. Following Han et al. (2020) and Prezzi et al. (2025), the axial load Q within the instrumented cross section of the pile cap was calculated based on the weighted average (by the area of influence in the cross section) of the strains measured by the six rebar strain gauges installed in the pile cap; the Young's moduli E_c and E_s of concrete and steel were taken as 24 GPa (3,481 ksi) and 200 GPa (29,000 ksi) in load calculations.

It can be observed from Figure 4.1 that (1) the loads carried by the three instrumented piles were approximately evenly distributed throughout the construction stages, and (2) the load within the instrumented zone of the pile cap was greater than the total load carried by the three instrumented piles both during and after bridge construction. Considering the equilibrium of the instrumented zone of the pile cap (Figure 2.14c), the superstructure load Q transferred to the pile cap is approximately balanced by the total load Q_{pg} carried by the three instrumented piles and the load Q_{cap} carried by the fill material (surrounding these piles) in contact with the pile cap. For the Whitestown MSE bridge abutment, most of the superstructure load was carried by the piles – the cap resistance Q_{cap} mobilized during bridge construction was approximately equal to 10% of the load in the pile cap, decreasing to about 8% at the end of bridge construction (stage 10) and then to 6% 4 months after the bridge was opened to traffic. Assuming the cap resistance to be equal to zero, as is typically done in MSE abutment design (FHWA, 2009a), the average dead load per pile, based on the data obtained for piles 11 to 13, would be 477 kN (107 kips) at the end of bridge construction. This value is in good agreement with the unfactored dead load of 456 kN (103 kips) per pile used in the design of Bent 3 of the Whitestown Parkway Bridge.

Figure 4.2 shows the evolution of the live load carried by the three instrumented piles (piles 11, 12, and 13) and the live load within the instrumented cross section of the pile cap during the live load test on October 30th, 2023, (i.e., 721 days since the beginning of construction). The live load carried by the piles and the pile cap increased as the trucks drove towards Bent 3 and were parked at their designated locations during each step of the live load test. The live loads carried by the three instrumented piles were approximately evenly distributed, with pile 13 carrying slightly greater live load than piles 11 and 12 throughout most of the live load test, except for load steps 1(a) and 8(a), where pile 12 carried greater live load than piles 11 and 13. The peak live loads in the piles and pile cap were reached at step 6 of the live load test when all twelve trucks were on the bridge, and the live loads decreased to zero at step 9 when all the trucks had left the bridge. The maximum total live load carried by the three instrumented piles was 580 kN (130 kips) at step 6 of the live load test. The live load in the instrumented cross section of the pile cap was greater than the total live load carried by the three instrumented piles, reaching a maximum value of 637 kN (143 kips) at step 6 of the live load test. The difference between these two loads is equal to the live load carried by the fill material (surrounding piles 11 to 13) in contact with the pile cap. From Figure 4.2, we see that, approximately 91% of the

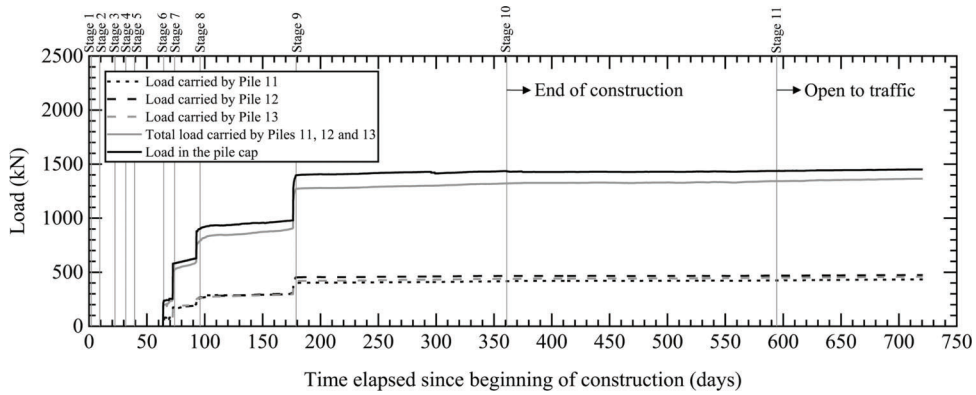

Figure 4.1 Evolution of the loads in the pile cap and piles during and after bridge construction.

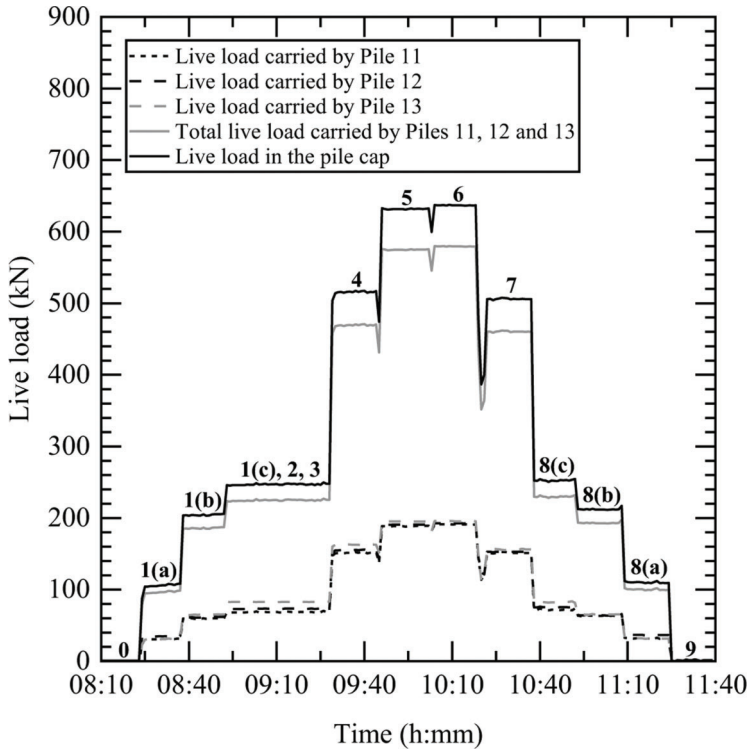

Figure 4.2 Live load in the instrumented cross section of the pile cap versus the total live load carried by the instrumented piles during steps 1 to 9 of the live load test.

live load in the pile cap was transferred to the piles during the live load test, while the remaining 9% of the live load was carried by the fill material in contact with the pile cap.

4.2 Vertical and Lateral Stresses

Figure 4.3 shows the evolution of the vertical stresses measured by the earth pressure cells located at the base of the leveling pad and at different elevations within the reinforced fill during and after bridge construction. The vertical distance from the base of the pile cap to the pressure cell is denoted by z, while the horizontal distance from the back of the wall facing to the pressure cell is denoted by x. From Figure 4.3b–d, we see that the vertical stresses measured within the reinforced fill increase with increasing distance of the pressure cell behind the wall facing. The vertical stresses measured by the pressure cells at $x = 2.4$ m (8 ft) and 4.0 m (13 ft) are consistent and close to each other because these cells are located beyond the pile cap and thus reflect the weight of the fill material placed behind the pile cap and end bent during construction of the bridge abutment; the same is also true for the pressure cells located behind the pile cap at $z = 0.1$ m (0.3 ft), as shown in Figure 4.3a. From Figure 4.3e, we see that the vertical stresses measured at the base of the leveling pad (denoted by $x = 0$) are greater than those measured along the base of the reinforced fill by factors of 2.0 at the end of wall construction (stage 5) and 1.8 after the

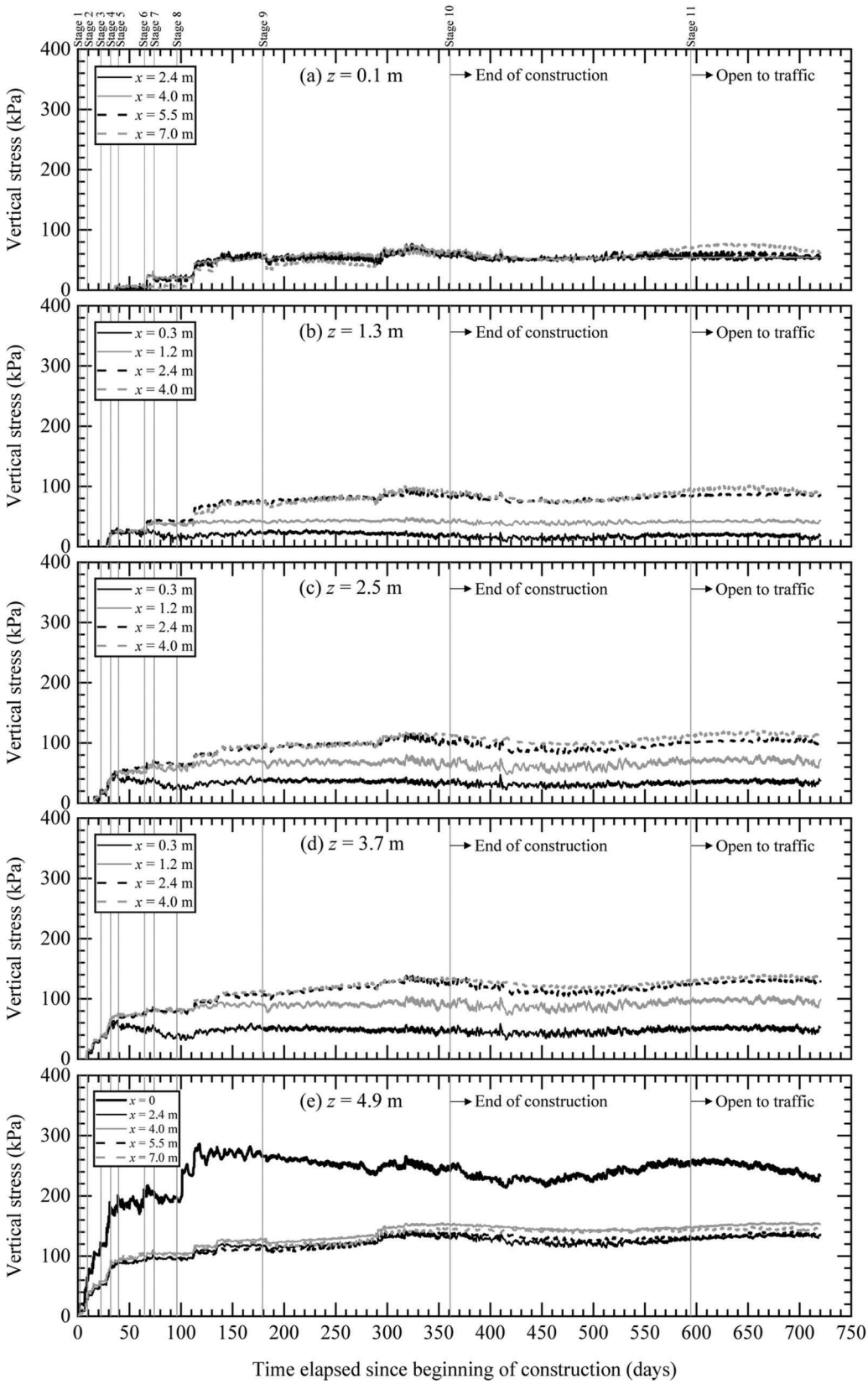

Figure 4.3 Evolution of vertical stresses at five elevations within the MSE abutment during and after bridge construction: (a) z = 0.1 m (0.3 ft), (b) z = 1.3 m (4.3 ft), (c) z = 2.5 m (8.2 ft), (d) z = 3.7 m (12.1 ft), and (e) z = 4.9 m (16.1 ft).

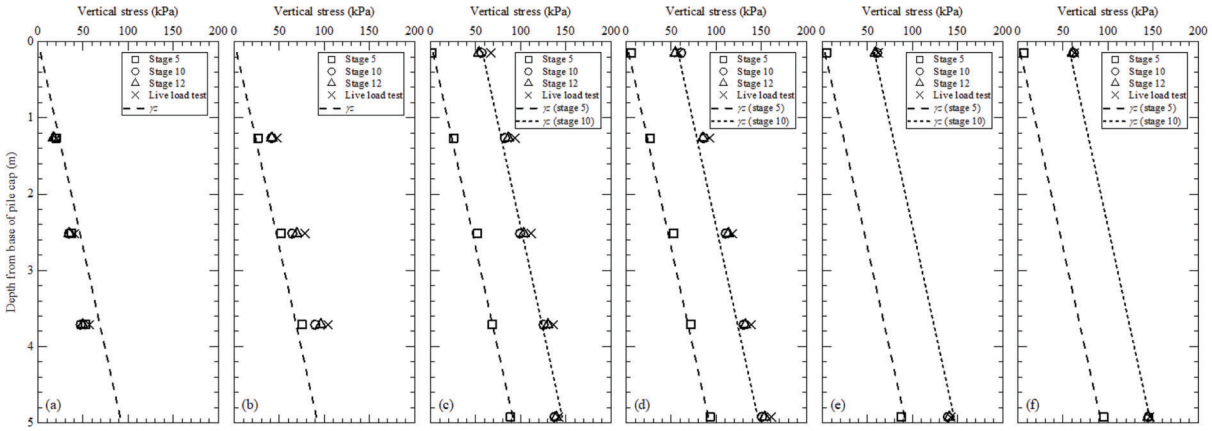

Figure 4.4 Depth profiles of the vertical stresses within the MSE abutment during and after bridge construction: (a) x = 0.3 m (1 ft), (b) x = 1.2 m (4 ft), (c) x = 2.4 m (8 ft), (d) x = 4.0 m (13 ft), (e) x = 5.5 m (18 ft), and (f) x = 7.0 m (23 ft).

bridge was constructed and opened to traffic (stage 11). The fluctuations in the vertical stress measurements at the base of the leveling pad after bridge construction may be attributed in part to some load redistribution due to the load-unload cycles caused by traffic along with changes in temperature and precipitation cycles.

Figure 4.4 shows the depth profiles of the vertical stresses measured by the pressure cells within the MSE abutment for the following stages: end of construction of the MSE wall (stage 5), end of bridge construction (stage 10), 4 months after the bridge was opened to traffic (stage 12) (prior to the live load test), and during the live load test. Figure 4.4a shows that the vertical stresses measured just behind the wall facing [x = 0.3 m (1 ft)] are smaller than those calculated based on the backfill self-weight γz, possibly due to arching effects (as discussed in Chapter 3); however, for $x > 1.2$ m (4 ft), the vertical stresses measured at different elevations within the MSE abutment compare well with those calculated based on γz for both stage 5 and stage 10 (Figure 4.4b–f). From Figure 4.4b, we see that the vertical stresses measured below the centerline of the pile cap [x = 1.2 m (4 ft)] increased by 12–16 kPa (251–334 psf) after the bridge was constructed on top of the MSE wall; this is likely due to the resistance provided by the fill material below the pile cap to the load applied on the cap by the bridge superstructure, as discussed previously. Given that the total cross-sectional area of the 19 H-piles [= 0.26 m^2 (2.84 ft^2)] corresponds to only 0.5% of the entire base area of the pile cap [= 50.2 m^2 (540 ft^2)], the remaining 99.5% of the base area of the pile cap is supported by the fill material below the cap; this partly explains the 12–16 kPa (251–334 psf) increase in vertical stress measured by the column of pressure cells below the pile cap. The vertical stresses measured by the pressure cells within the MSE abutment were generally constant during the period of time from the end of bridge construction up to 4 months after the bridge was opened to traffic; the stresses increased by about 5–9 kPa (104–188 psf) during the live load test compared to those measured before the test.

The vertical stress $\sigma_v|_{\mathrm{lp,m}}$ measured by the pressure cell at the base of the leveling pad and the vertical stress $\sigma_v|_{\mathrm{lp,c}}$ calculated at the base of the leveling pad based on the self-weight of the wall facing are plotted in Figure 4.5a, while the ratio of these two quantities is shown in Figure 4.5b for different stages during and after bridge construction (note that stage 11 in the figure corresponds to the opening of the bridge to traffic). From Figure 4.5a, we see that the vertical stress measured at the base of the leveling pad is consistently greater than that calculated based on the self-weight of the wall facing both during and after construction of the MSE bridge abutment. For example, the vertical stress measured at the base of the leveling pad increased from 19 kPa (397 psf) at the end of stage 1 to 190 kPa (3,968 psf) at stage 5, and, finally, to 255 kPa (5,326 psf) after the bridge was constructed and opened to traffic (stage 11). In contrast, the vertical stress at the base of the leveling pad due to the self-weight of the wall facing increased from 12 kPa (251 psf) at the end of stage 1 to 80 kPa (1,671 psf) at the end of wall construction (stage 5) and remained constant at 80 kPa (1,671 psf) thereafter. The vertical stress ratio at the end of wall construction is equal to 2.4, increasing to a value of 3.2 after the bridge was constructed and opened to traffic. These results highlight the importance of proper soil compaction near the leveling pad along with the selection of a suitable pad width and concrete grade to ensure both the stability and serviceability of the abutment throughout the service life of the bridge; this is even more important for tall MSE abutment walls. The vertical stress at the base of the leveling pad increased by 7 kPa (146 psf) during the live load test compared to that measured before the test.

Figure 4.6 shows the depth profiles of the lateral stresses measured by the pressure cells on the back of the wall facing and the distribution of the lateral earth pressure coefficient K_r for the following stages: end of construction of the MSE wall (stage 5), end of bridge

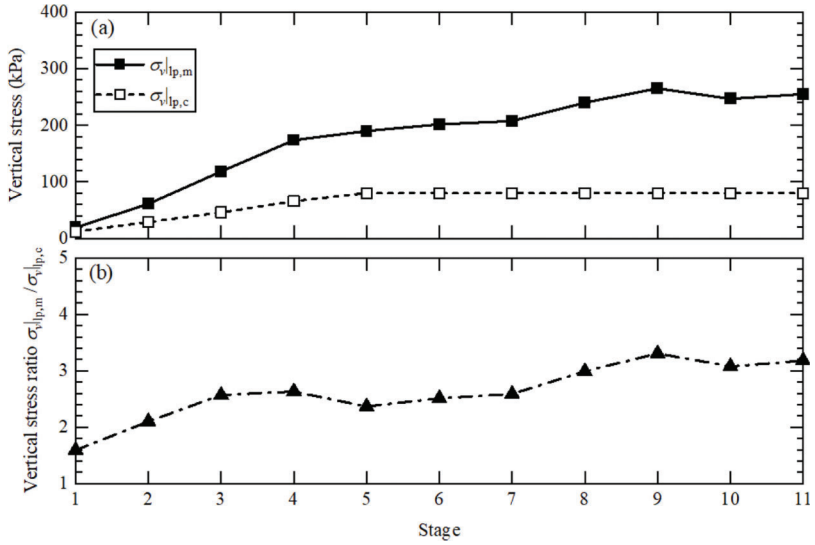

Figure 4.5 Evolution of (a) vertical stresses $\sigma_v|_{lp,m}$ and $\sigma_v|_{lp,c}$, and (b) vertical stress ratio $\sigma_v|_{lp,m}$ / $\sigma_v|_{lp,c}$ during and after bridge construction.

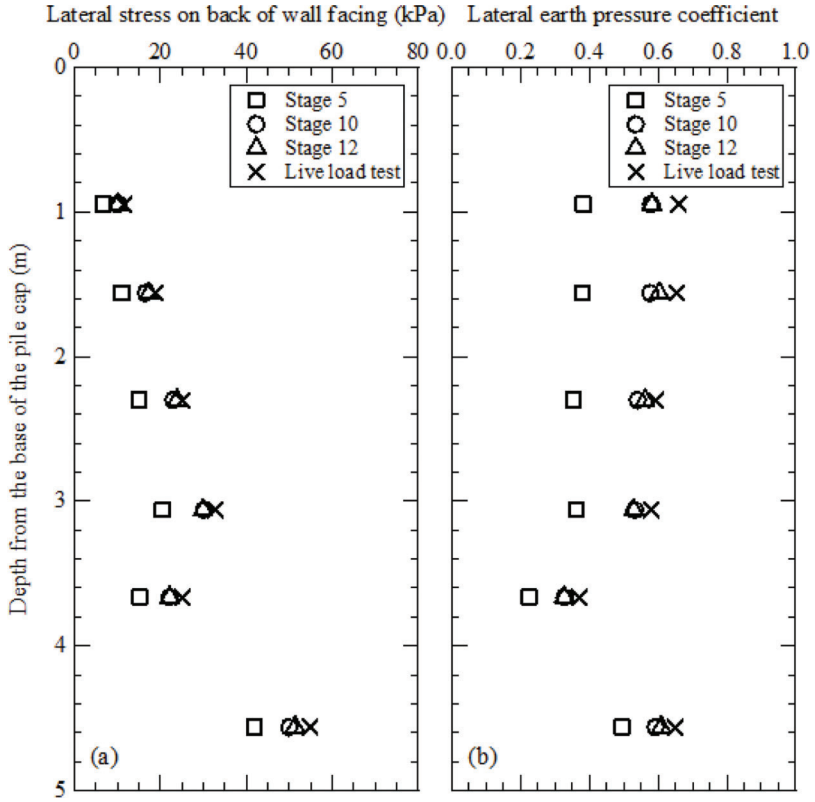

Figure 4.6 Distribution of (a) lateral stresses on the back of the wall facing, and (b) lateral earth pressure coefficient during and after bridge construction.

construction (stage 10), 4 months after the bridge was opened to traffic (stage 12) (prior to the live load test), and during the live load test. The lateral earth pressure coefficient was calculated by dividing the measured lateral effective stresses by the vertical effective stresses obtained based on the backfill self-weight γz, where z is the distance from the base of the pile cap to the elevation of the pressure cell. It can be observed from Figure 4.6a that (1) the lateral stresses on the back of the wall facing increased by about 4–9 kPa (83–188 psf) after the bridge was constructed on top of the MSE wall, with the maximum increase in lateral stress located at a depth of 3.1 m (10.2 ft) below the top of the reinforced fill; (2) the lateral stresses were generally

constant [with a maximum increase of about 1 kPa (21 psf)] during the period of time from the end of bridge construction (stage 10) up to 4 months after the bridge was opened to traffic (stage 12); and (3) the lateral stresses on the back of the wall facing increased by about 1–4 kPa (21–84 psf) during the live load test from those measured before the test. According to FHWA (2009a), the additional lateral stress on the back of the wall facing (due to bridge construction) may decrease linearly or non-linearly with increasing depth below the top of the MSE wall. Based on the pressure cell data obtained in this study, the maximum increase in lateral stress on the back of the wall facing (due to bridge construction) occurred not at the top of the wall, as suggested by FHWA (2009a), but in the lower half of the wall (i.e., at $z/H = 0.62$ for the Whitestown MSE abutment), which is generally consistent with the findings of Pierson (2008) and Huang et al. (2013) based on field testing and numerical simulations of laterally loaded piles behind MSE walls. Figure 4.6b shows that the lateral earth pressure coefficient at the end of wall construction (stage 5) ranges from 0.2 to 0.5, with higher values observed near the bottom of the wall due to the passive resistance provided by the compacted sandy soil placed in front of the wall during construction. The lateral earth pressure coefficient increased to values ranging from 0.3 to 0.6 after the bridge was constructed on top of the MSE wall and opened to traffic.

Based on the lateral stresses measured on the back of the wall facing at the end of both wall construction (stage 5) and bridge construction (stage 10) and the assumption that the angle of wall friction δ has fully mobilized to its value δ_c at critical state, the critical-state interface shear stress τ_c along the back of the wall facing was calculated following the procedure outlined in Chapter 3 and plotted in Figure 4.7. If we integrate the shear stress distribution for stage 10 across the height of the wall facing (per unit length of wall), we obtain a total vertical (downward) shear force F_s of 48.2 kN (10.8 kips). Dividing the value of F_s by the contact area of the base of the leveling pad leads to a vertical stress of 158 kPa (3,301 psf), corresponding to 64% of the vertical stress $\sigma_v|_{lp,m}$ [= 247 kPa (5,154 psf)] measured at the base of the leveling pad at the end of bridge construction. Given that the vertical stress at the base of the leveling pad due to the self-weight of the wall facing is 80 kPa (1,671 psf) (corresponding to 33% of $\sigma_v|_{lp,m}$), the remaining vertical stress [≈ 9 kPa (182 psf) (or 3% of $\sigma_v|_{lp,m}$)] at the base of the leveling pad may be attributed to the transfer of some reinforcement-facing connection downdrag forces to the leveling pad, as illustrated by Damians et al. (2013,2016).

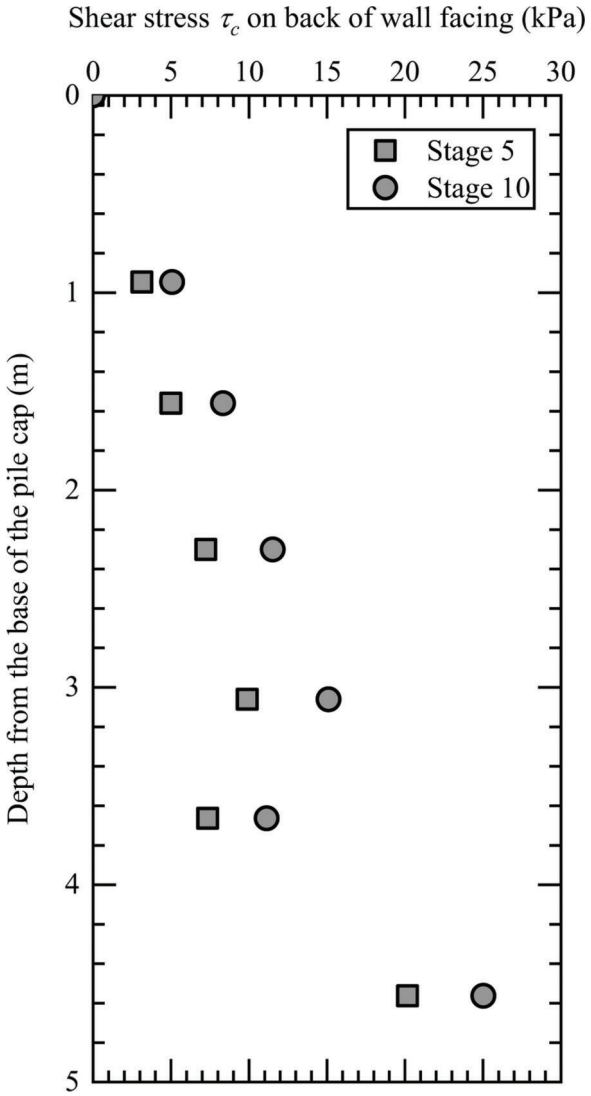

Figure 4.7 Shear stress distribution along the back of the wall facing at the end of wall construction (stage 5) and at the end of bridge construction (stage 10).

4.3 Reinforcement Loads

Figure 4.8 shows the distribution of the reinforcement tensile load T (in units of force per unit length of wall in the longitudinal direction) for each of the four levels of instrumented steel strips for the following stages: end of construction of the MSE wall (stage 5), end of bridge construction (stage 10), 4 months after the bridge was opened to traffic (stage 12) (prior to the live load test), and during the live load test. From Figure 4.8d, we see that the increase in the tensile load in the first (bottommost) reinforcement level [at $z = 4.6$ m (15.1 ft); z is the vertical distance from the base of the pile cap to the reinforcement level of interest] after bridge construction and opening to traffic is small [≈ 0.2–1.0 kN/m (0.01–0.07 kips/ft)] compared to the values measured at the end of wall construction. In contrast, the tensile loads in the third and fifth reinforcement levels [$z = 3.1$ m (10.2 ft) and 1.6 m (5.25 ft)] after bridge construction and opening to traffic increased by about 3–8 kN/m (206–548 lb/ft) and 2–6 kN/m (137–411 lb/ft), respectively, compared to those measured at the end of wall construction (see Figure 4.8b and Figure 4.8c). Figure 4.8a shows that

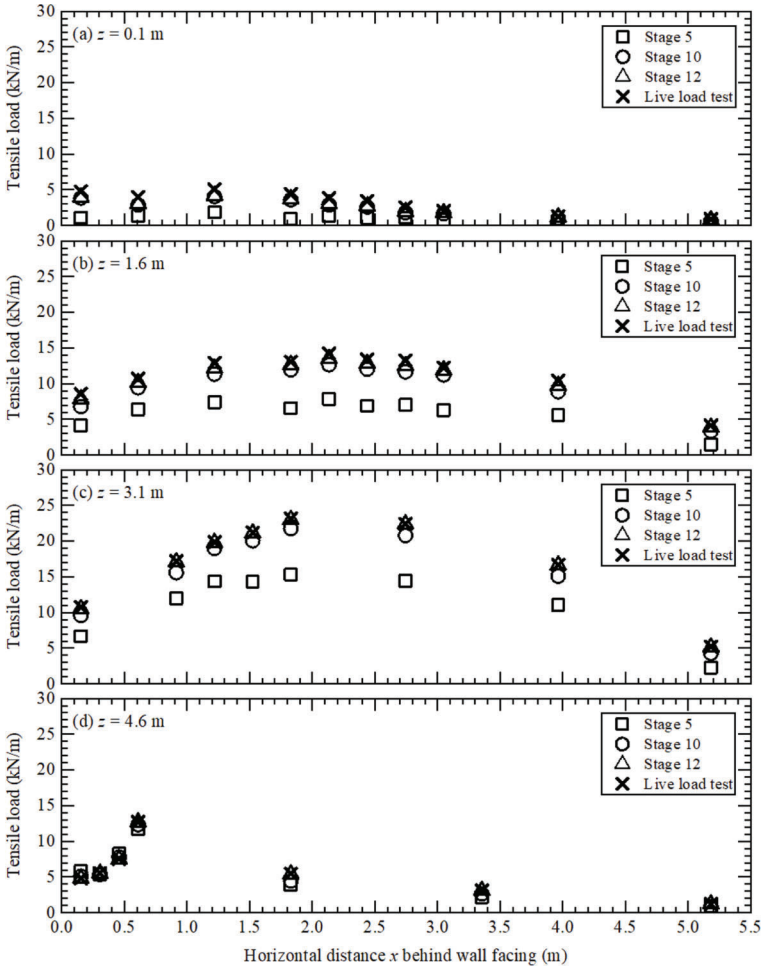

Figure 4.8 Distribution of reinforcement tensile loads behind the wall facing during and after bridge construction: (a) $z = 0.1$ m (0.3 ft), (b) $z = 1.6$ m (5.25 ft), (c) $z = 3.1$ m (10.2 ft), and (d) $z = 4.6$ m (15.1 ft).

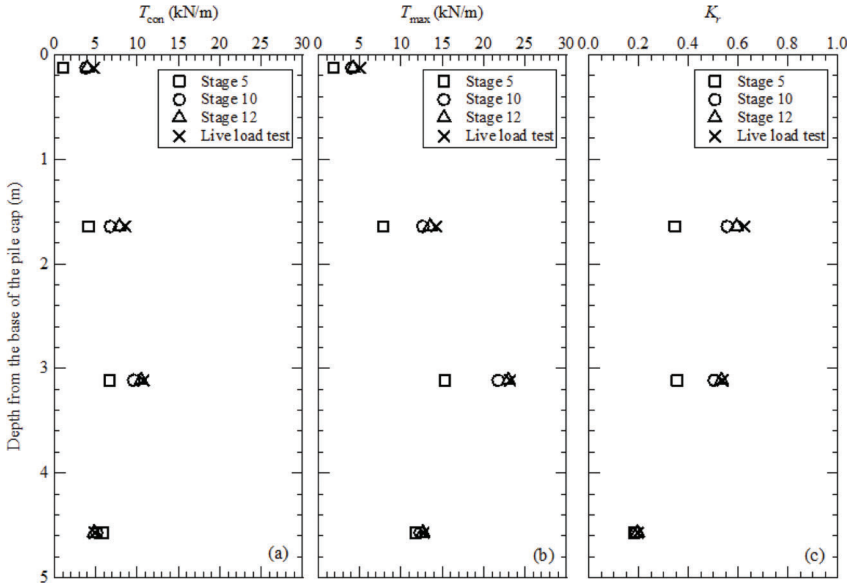

Figure 4.9 Distribution of (a) tensile load T_{con} near the reinforcement-panel connection, (b) maximum reinforcement tensile load T_{max}, and (c) lateral earth pressure coefficient K_r during and after bridge construction.

the effect of bridge construction and live load test operation on the reinforcement-panel connection load T_{con} is more pronounced for the seventh reinforcement level [located near the top of the wall (z = 0.1 m (0.3 ft))], where the value of T_{con} is approximately equal to the maximum tensile load T_{max} in the reinforcement (measured below the centerline of the pile cap). This observation highlights the importance of the reinforcement-panel connection limit state check for internal stability design of MSE bridge abutments, as noted by AASHTO (2020).

Figure 4.9a shows that, for stage 10 (corresponding to the end of bridge construction), the value of T_{con} increases from 3.8 kN/m (260 lb/ft) near the top of the wall [z = 0.1 m (0.3 ft)] to 9.6 kN/m (658 lb/ft) at a depth of 3.1 m (10.2 ft) and then decreases to 5.1 kN/m (349 lb/ft) near the bottom of the wall [z = 4.6 m (15.1 ft)]. The distribution of T_{max} for stage 10 is similar to that of T_{con}, with values ranging from 4.1 kN/m (281 lb/ft) near the top of the wall to 21.8 kN/m (1,494 lb/ft) at a depth of 3.1 m (10.2 ft), and, finally, to 12.3 kN/m (843 lb/ft) near the bottom of the wall (Figure 4.9b). The values of T_{con} and T_{max} were generally constant during the period of time from the end of bridge construction up to 4 months after the bridge was opened to traffic. During the live load test, the values of T_{con} and T_{max} increased by a maximum of 0.9 kN/m (62 lb/ft) [corresponding to the seventh (topmost) reinforcement level] compared to those measured before the test. The ratio T_{con}/T_{max} after bridge construction and opening to traffic ranges from 0.40 to 0.95, with higher values corresponding to reinforcement levels located closer to the base of the pile cap.

The lateral earth pressure coefficient K_r was back-calculated from the reinforcement strain gauge data by dividing the value of T_{max} with $\gamma z s_v$, where s_v is the tributary vertical spacing of the reinforcement. Figure 4.9c shows that the value of K_r is of the order of 0.5 to 0.6 after the bridge was constructed and opened to traffic. These values are in good agreement with those determined from the lateral stresses measured by the pressure cells on the back of the wall facing Figure 4.6b, except for the bottommost reinforcement level [z = 4.6 m (15.1 ft)], where the value of K_r determined from the reinforcement strain gauge data (= 0.20) is less than that obtained from the pressure cell data (= 0.62). This is because the lateral stresses acting on the back of the bottommost facing panel are balanced in part by the passive resistance provided by the compacted sandy soil placed in front of it during bridge construction; consequently, these stresses are not fully transferred to the bottommost reinforcement level, resulting in the mobilization of smaller tensile loads and K_r values than what would be expected in the absence of the passive resistance.

4.4 Vertical and Lateral Displacements

Figure 4.10 shows the outward lateral displacement profiles of the wall facing for the following stages: end of construction of the MSE wall (stage 5), end of bridge construction (stage 10), 4 months after the bridge was opened to traffic (stage 12) (prior to the live load test), and during the live load test. Most of the lateral displacement of the wall facing occurred during construction of the MSE wall. The maximum lateral displacement of the wall facing, which was 10 mm (0.4 in.) at the end of wall construction, increased by a maximum value of 2.1 mm (0.08 in.) at the end of bridge construction. Based on the positions of the tilt sensors along the inclinometer string, the maximum lateral displacement of the wall facing [= 12.1 mm (0.48 in.)] at the end of bridge construction was located at a depth of 2.8 m (9.2 ft) below the top of the reinforced fill; this is close to the depth of 3.1 m (10.2 ft) where the maximum tensile load T_{max} [= 21.8 kN/m (1,494 lb/ft)] was measured in the instrumented steel strips (see Figure 4.9b). During the live load test, the lateral displacement of the wall facing increased by a maximum value of 0.8 mm (0.03 in.) compared to that measured before the test; this occurred at a depth of 0.3 m (1 ft), which is near the elevation of the topmost reinforcement level, where the largest increment in tensile load [= 0.9 kN/m (62 lb/ft)] was measured during the test. Table 4.1 summarizes the values of the

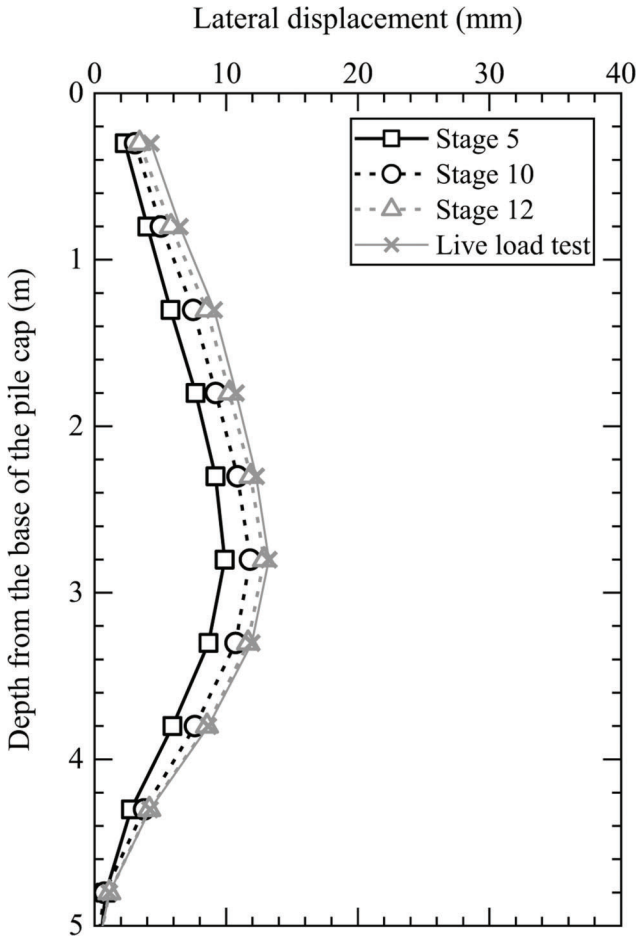

Figure 4.10 Outward lateral displacement profiles of the wall facing during and after bridge construction.

TABLE 4.1
Values of T_{con}, T_{max}, and u/H for various stages during and after bridge construction

	Stage 5			Stage 10			Four Months of Traffic			Live Load Test		
z/H	T_{con} (kN/m)	T_{max} (kN/m)	u/H (%)	T_{con} (kN/m)	T_{max} (kN/m)	u/H (%)	T_{con} (kN/m)	T_{max} (kN/m)	u/H (%)	T_{con} (kN/m)	T_{max} (kN/m)	u/H (%)
0.02	1.1	1.9	0.024	3.8	4.1	0.046	4.0	4.2	0.049	4.8	5.1	0.067
0.32	4.1	7.9	0.138	6.8	12.7	0.169	7.9	13.5	0.189	8.6	14.2	0.201
0.62	6.7	15.3	0.184	9.6	21.8	0.225	10.5	23.0	0.244	10.8	23.2	0.251
0.92	5.9	11.7	0.034	5.1	12.3	0.041	4.8	12.7	0.049	4.9	12.7	0.050

Unit conversion: 1 kN/m = 68.5 lb/ft.

Note: z = depth of the instrumented steel strip below the pile cap, H = height of the reinforced fill (measured from the top of the leveling pad to the base of the pile cap), T_{con} = tensile load in the reinforcement near the connection with the wall facing (in units of force per unit length of wall in the longitudinal direction), T_{max} = maximum tensile load in the reinforcement (in the same units as T_{con}), and u = outward lateral displacement of the wall facing. Stage 5 corresponds to the end of construction of the MSE wall (on 12/17/2021), while stage 10 corresponds to the end of construction of the bridge (on 11/4/2022). The bridge was opened to traffic on 6/26/2023, and the live load test was performed on 10/30/2023.

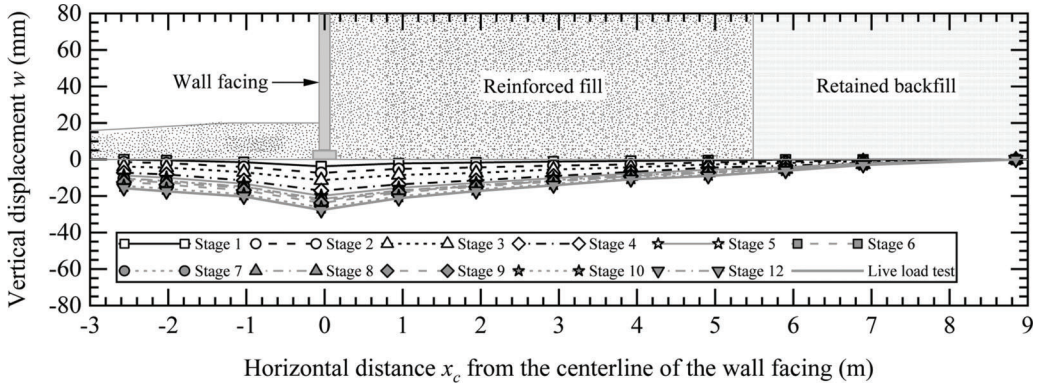

Figure 4.11 Vertical displacement profiles (displacements negative in the downward direction) of the MSE wall foundation during and after bridge construction.

reinforcement-panel connection load T_{con}, the maximum reinforcement tensile load T_{max}, and the normalized lateral displacement u/H of the wall facing for various stages during and after bridge construction, where H is the height of the reinforced fill measured from the top of the leveling pad to the base of the pile cap [≈ 5 m (16.3 ft) for Bent 3 of the Whitestown Parkway Bridge].

Figure 4.11 shows the vertical displacement profiles of the MSE wall foundation for various stages during and after bridge construction. The vertical displacement w of the MSE wall foundation (below the leveling pad) increased from 20 mm (0.8 in.) at the end of wall construction (stage 5) to 26 mm (1.02 in.) at the end of construction of the bridge on top of the MSE wall (stage 10), 27.5 mm (1.08 in.) after 4 months of traffic on the bridge (stage 12), and 27.7 mm (1.09 in.) during the live load test. Given that the width B of the leveling pad is 1 ft (304.8 mm), the relative settlement w/B of the leveling pad is equal to 6.5% at the end of wall construction and 8.5% at the end of construction of the Whitestown Parkway Bridge. For Bent 3 of the Whitestown Parkway Bridge, the top soft clay layer was excavated down to a depth of 1.5 m (5 ft) (based on the SPT boring logs) and replaced with compacted

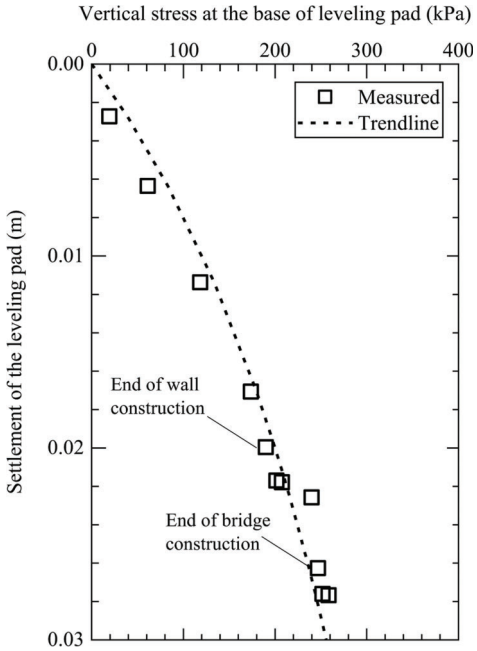

Figure 4.12 Vertical stress at the base of the leveling pad versus the settlement of the leveling pad for Bent 3 of the Whitestown Parkway Bridge.

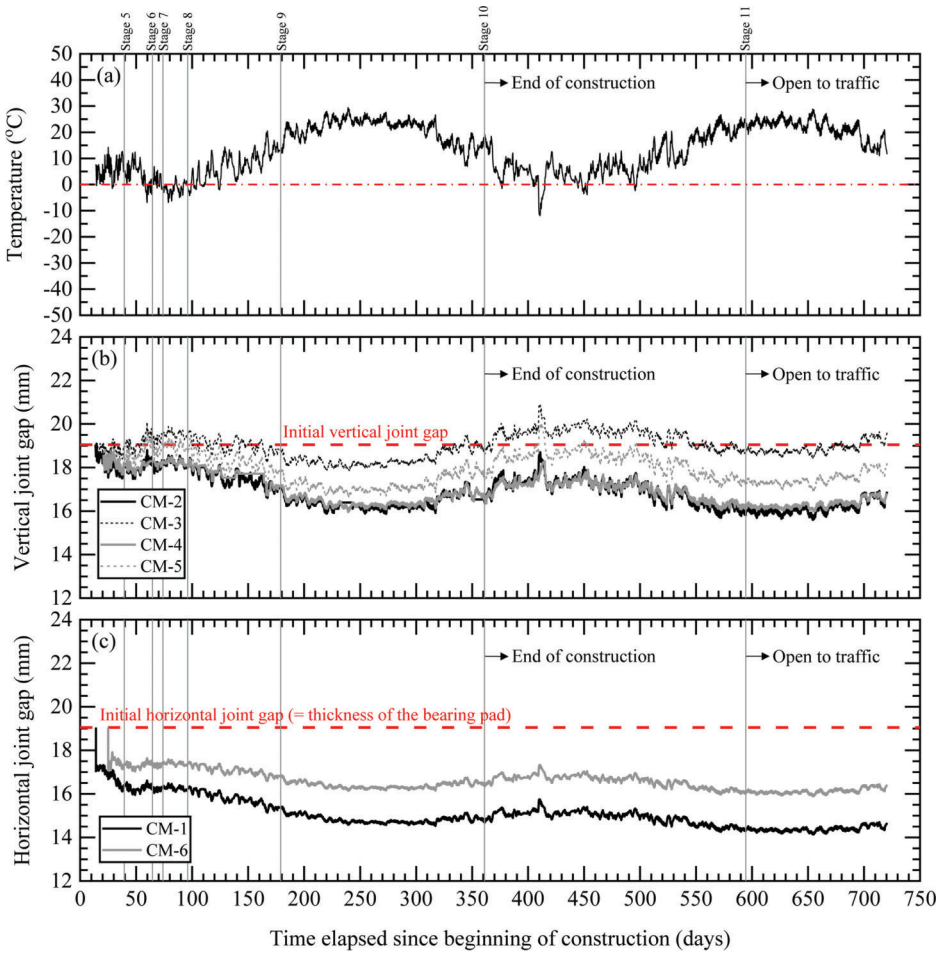

Figure 4.13 Evolution of the horizontal and vertical joint gap width between facing panels during and after bridge construction.

sandy soil prior to the construction of the MSE abutment. The high values of w/B observed for the leveling pad may be attributed to the settlement of the remaining 0.9 m of this layer, as evidenced by the low q_t values [≈ 0.3 MPa (3 tsf)] (see Figure 2.4) measured at that depth from CPT soundings performed near the location of the MSE wall. These results suggest that it would be worthwhile considering using wider pads to limit the relative settlement and to increase the factor of safety of the leveling pad against bearing capacity failure, particularly for cases where weak soil layers are found near the base of the MSE wall foundation.

Based on the data obtained from the pressure cells and the inclinometers used in this study, the vertical stress at the base of the leveling pad can be related to the corresponding settlement of the pad, as shown in Figure 4.12. For Bent 3 of the Whitestown Parkway Bridge, the secant modulus of subgrade reaction k_s of the leveling pad (calculated by taking the slope from the origin to the point of interest on the trendline in Figure 4.12) is equal to 11,450 kPa/m (73 ksf/ft) for a pad settlement of 12.7 mm (0.5 in.) and 9,150 kPa/m (58 ksf/ft) for a pad settlement of 25.4 mm (1 in.), corresponding to 20% degradation of the k_s value.

4.5 Joint Gap Width

Figure 4.13b and Figure 4.13c shows the evolution of the vertical and horizontal joint gap width between facing panels measured by the crackmeters during and after bridge construction. Note that the initial vertical and horizontal joint gap widths at the time of panel installation were 19.05 mm (0.75 in.). From Figure 4.13c, we see that the horizontal joint gap width measured by crackmeter CM-1 is equal to 16.4 mm (0.65 in.) at the end of wall construction (stage 5), decreasing to values equal to 14.7 mm (0.58 in.) near the end of bridge construction (stage 10) and 14.3 mm (0.56 in.) after the bridge has been opened to traffic. By contrast, the horizontal joint gap width measured by crackmeter CM-6, located 5 ft (1.5 m) above CM-1 (Figure 2.12a), is approximately 1–2 mm (0.04–0.08 in.) greater than that measured by CM-1, with higher values corresponding to the end of bridge construction and while the bridge is in service.

From Figure 4.13b, we see that the values of vertical joint gap width measured by crackmeters CM-2 and CM-4 are consistent and close to each other both during and after bridge construction; the corresponding

values are 18.1 mm (0.71 in.) at the end of wall construction (stage 5) and 16.1 mm (0.63 in.) after the bridge was constructed and opened to traffic. By contrast, the values of vertical joint gap width measured by crackmeters CM-3 and CM-5 are greater than those measured by CM-2 and CM-4, and the vertical joint gap width measured by CM-3 is about 0.5–1.5 mm (0.02–0.06 in.) greater than that measured by CM-5, indicating some non-uniformity in gap closure for the vertical joint along which CM-3 and CM-5 were installed (Figure 2.12a).

The effect of temperature on the joint gap measurements during the time period between the end of bridge construction and the opening of the bridge to traffic can be seen in Figure 4.13a. The values of the vertical and horizontal joint gap width between the precast concrete facing panels increased with decreasing temperature due to the contraction of the facing panels and decreased with increasing temperature due to the expansion of the facing panels. In addition, Figure 4.13 shows that the effect of temperature on the joint gap measurements is more pronounced for vertical joints than horizontal joints; for example, as the temperature decreased from 24°C (75°F) on August 10th, 2022, at 12:00 pm (corresponding to day 275 since the beginning of construction of the MSE bridge abutment) to 4°C (39°F) on January 29th, 2023, at 12:00 am (corresponding to day 446 since the beginning of construction), the vertical joint gap width increased by about 1.5 mm (0.06 in.), whereas the horizontal joint gap width increased by 0.5 mm (0.02 in.). The temperature measured by the thermistor in each crackmeter was consistent across all crackmeters installed at the panel joints, and thus only the average temperature [averaged across the six crackmeters for each point in time when data was collected (i.e., every 4 hours)] is plotted in Figure 4.13a; the oscillations in the data reflect the local day/night temperature variations measured by the thermistors in the crackmeters. Both the vertical and horizontal joint gap widths measured by the crackmeters were practically constant and varied by only $\pm$ 0.1 mm (0.004 in.) during the live load test.

5. DCPT-BASED ESTIMATION OF MSE WALL BEARING CAPACITY

5.1 DCPT Results for the Foundation Soil

Four dynamic cone penetration tests (DCPTs) were performed on September 21st, 2021; DCPT-1 and DCPT-2 were performed on either side of boring SPT-1 along the shoulder of I-65, whereas DCPT-3 and DCPT-4 were performed on either side of boring SPT-2 along the shoulder of Perry Worth Road (see Figure 2.3 for the layout of the SPTs and CPTs performed at the MSE wall location). The distances between the DCPTs and the corresponding CPT soundings (CPT-1 to CPT-4) ranged from 5–13 ft (1.5–4.0 m). Figure 5.1 shows the depth profiles of the cumulative DCPT blow count and penetration index for each of the four DCPTs along with the corrected, total cone resistance q_t for each of the four CPTs. The cumulative DCPT blow count for 0.3 m (12 in.) of penetration ranges from 21 blows for DCPT-3 to 35 blows for DCPT-4, whereas for 0.6 m (24 in.) of penetration, the cumulative DCPT blow count ranges from 36 blows for DCPT-3 to 74 blows for DCPT-4. The penetration index is of the order of 20–30 mm/blow (0.8–1.2 in./blow) near the ground surface and generally decreases to values ranging from 5–15 mm/blow (0.2–0.6 in./blow) for penetration depths greater than 0.1 m (4 in.).

Based on the results of laboratory tests performed on split-spoon soil samples collected from boring SPT-1 at a depth of 1.0–2.5 ft (0.30–0.75 m) below the ground surface, the soil layer through which DCPT-1 and DCPT-2 were performed is classified as silty sand with gravel (SM) according to the Unified Soil Classification System (USCS) and A-2–4(0) according to AASHTO (or "sandy loam" according to the description in the SPT-1 boring log). It consists of 18% gravel, 55% sand, 20% silt, and 7% clay, with D_{50} = 0.55 mm, liquid limit LL = 16%, and plasticity index PI = 3%. The peak in cone resistance [= 18 MPa (376 ksf)] observed for CPT-2 at a depth of 0.40–0.45 m (1.3–1.5 ft) may be attributed to the presence of gravel-sized particles at that depth; however, there is no corresponding drop in the DCPT penetration index at that depth (Figure 5.1), indicating some variability in layer thickness or material composition across the 13-ft (4-m) distance between CPT-2 and DCPT-2.

Based on the results of laboratory tests performed on split-spoon soil samples collected from boring SPT-2 at a depth of 1.0–2.5 ft (0.30–0.75 m) below the ground surface, the soil layer through which DCPT-3 and DCPT-4 were performed is classified as silty clay with sand (CL) according to USCS and A-6(8) according to AASHTO (or "clay loam" according to the description in the SPT-2 boring log). It consists of 31% sand, 42% silt, and 26% clay, with D_{50} = 0.02 mm, LL = 36%, and PI = 15%. Figure 5.1 shows that the cumulative DCPT blow count for DCPT-4 is greater than that for DCPT-3, which is consistent with the fact that the corresponding cone resistance for CPT-4 is greater than that for CPT-3. Table 5.1 summarizes the blow counts obtained from each of the four DCPTs for 0–12 in. (0–0.3 m), 12–24 in. (0.3–0.6 m), and 24–28 in. (0.6–0.7 m) penetration depths along with the average cone resistance obtained from each of the four CPTs within these depth increments.

Figure 5.2 plots the normalized CPT cone resistance versus the normalized DCPT penetration index based on the data obtained from the four pairs of CPTs and DCPTs performed in the foundation soil prior to wall construction. The data points corresponding to the peak in cone resistance observed for CPT-2 at a depth of 0.40–0.45 m (1.3–1.5 ft) were considered to be outliers and thus discarded from the plot. It can be

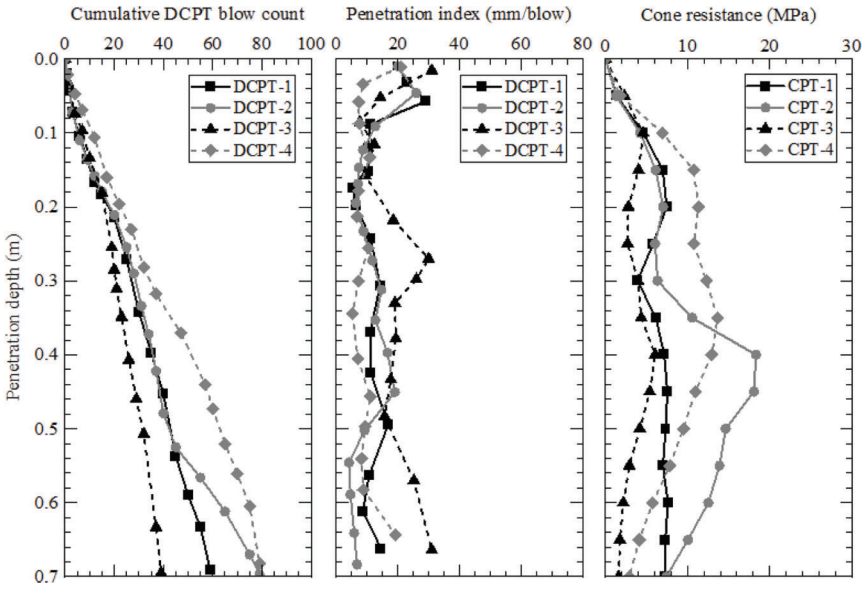

Figure 5.1 Profiles of cumulative DCPT blow count, DCPT penetration index, and CPT cone resistance for the foundation soil prior to wall construction.

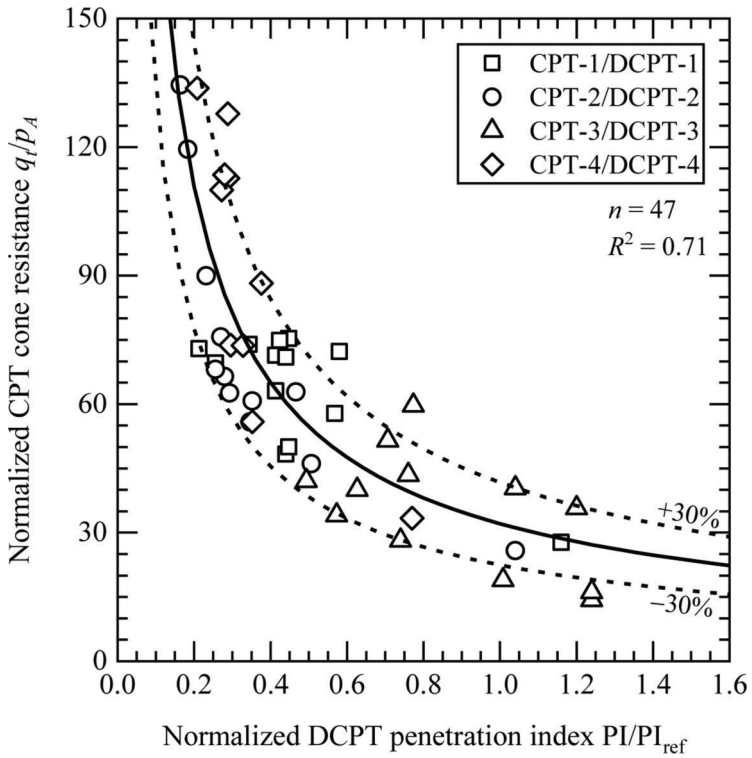

Figure 5.2 Normalized CPT cone resistance versus normalized DCPT penetration index based on CPTs and DCPTs performed in the foundation soil prior to wall construction.

TABLE 5.1
Values of DCPT blow count and CPT cone resistance for 0–12 in., 12–24 in., and 24–28 in. penetration depths in the foundation soil

Penetration Depth (in.) [m]	DCPT Blow Count				CPT Cone Resistance (MPa) [ksf]			
	DCPT-1	DCPT-2	DCPT-3	DCPT-4	CPT-1	CPT-2	CPT-3	CPT-4
0–12 [0.0–0.3]	27	29	21	35	4.3 [90]	4.4 [93]	2.9 [61]	7.7 [161]
12–24 [0.3–0.6]	24	33	15	39	6.7 [139]	13.5 [282]	4.1 [87]	10.4 [218]
24–28 [0.6–0.7]	9	17	3	6	7.4 [154]	10.0 [209]	1.8 [38]	4.3 [89]

observed from Figure 5.2 that most of the 47 data points fall within ±30% of the best fit, which is described by the following relationship:

$$\frac{q_t}{p_A} = 32.1\left(\frac{PI}{PI_{\text{ref}}}\right)^{-0.77} \qquad \text{(Eq. 5.1)}$$

where p_A = reference stress (= 100 kPa or 1 tsf), PI_{ref} = reference DCPT penetration index (= 25 mm or 1 in. per blow), and the coefficient of determination R^2 is equal to 0.71. Equation 5.1 is applicable for the range of stress levels and materials tested in this study (i.e., for silty sand (A-2–4) and silty clay (A-6) type of materials, or, equivalently, for "sandy loam" and "clay loam" type of materials, as reported in the SPT boring logs in Indiana). Further research is needed, and additional CPT and DCPT data need to be collected in different soil profiles to improve this relationship.

5.2 DCPT Results for Compacted B-Borrow Material

5.2.1 DCPTs Adjacent to CPT-5

Two DCPTs (DCPT-5 and DCPT-6) were performed near the location of CPT-5 on November 1st, 2021, after the top 5-ft (1.5-m) of foundation soil was excavated and replaced with compacted B-borrow material (see Figure 2.3 for the location in plan view of CPT-5). Figure 5.3 shows the depth profiles of the cumulative DCPT blow count and penetration index for DCPT-5 and DCPT-6 along with the cone resistance for CPT-5. The results for both DCPT-5 and DCPT-6 are consistent and close to each other. The penetration index is equal to 16 ± 1 mm/blow (0.63 ± 0.04 in./blow) for penetration depths ranging from 0.2–0.6 m (8–24 in.); the corresponding average cone resistance for this depth range is 2.4 MPa (50 ksf). Table 5.2 summarizes the blow counts obtained from DCPT-5 and DCPT-6 for 0–12 in. (0–0.3 m) and 12–24 in. (0.3–0.6 m) penetration depths along with the average cone resistance obtained from CPT-5 within these depth increments. Given the lack of confinement for the first 12 in. (0–0.3 m) of penetration (which may affect the DCPT and CPT results within this zone), the ratio $q_t/p_A N_{DCP}$ was determined for the second 12 in. (0.3–0.6 m) of penetration and found to be equal to 1.1, where p_A = reference stress (= 100 kPa or 1 tsf), and N_{DCP} = DCPT blow count.

5.2.2 DCPTs Adjacent to the Earth Pressure Cells

Figure 5.4 shows the layout of the 12 DCPTs performed on November 10th, 2021, near the pressure cells at the base of the MSE wall foundation. The DCPTs were performed at a distance of 3.5 ft (1.1 m) from the pressure cells and at distances of 8–23 ft (2.4–7.0 m) behind the wall facing. Figure 5.5 shows the depth profiles of the cumulative DCPT blow count and penetration index for each of the 12 DCPTs. The penetration index values for the DCPTs generally lie within a range of 10–20 mm/blow (0.4–0.8 in./blow) for penetration depths ranging from 0.3–0.7 m (12–28 in.). Table 5.3 summarizes the blow counts obtained for each of the 12 DCPTs for 0–12 in. (0–0.3 m), 12–24 in. (0.3–0.6 m), and 24–28 in. (0.6–0.7 m) penetration depths. For 0–12 in. (0–0.3 m) penetration, the mean blow count (rounded to the nearest whole number) is equal to 8, with a coefficient of variation (COV) of 16%. Similarly, the values of mean blow count and COV for 12–24 in. (0.3–0.6 m) penetration are 25% and

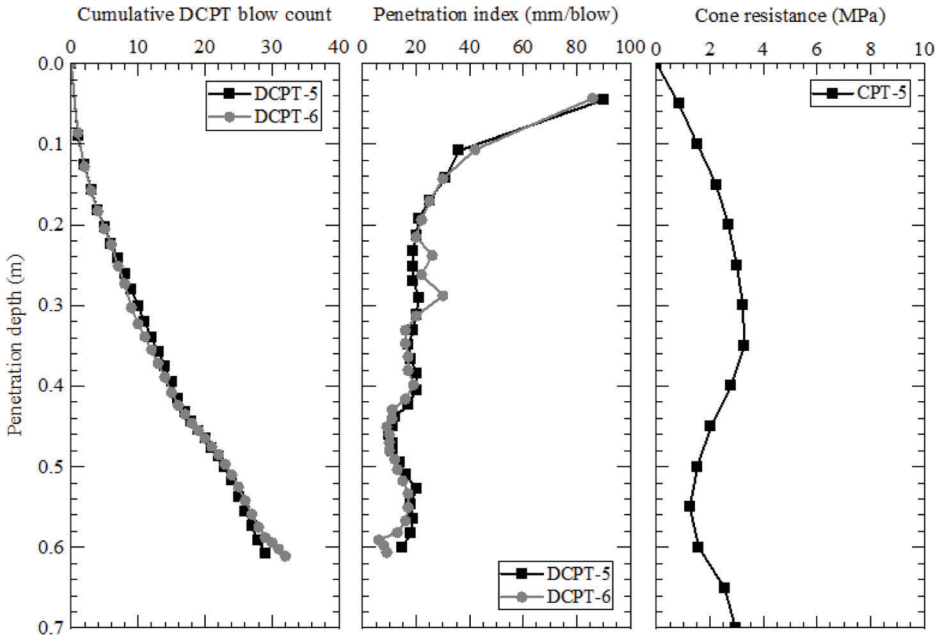

Figure 5.3 Profiles of cumulative DCPT blow count, DCPT penetration index, and CPT cone resistance for the B-borrow material prior to wall construction.

TABLE 5.2
Values of DCPT blow count and CPT cone resistance for 0–12 in. and 12–24 in. penetration depths in B-borrow material

	DCPT Blow Count		Cone Resistance (MPa) [ksf]
Penetration Depth (in.) [m]	**DCPT-5**	**DCPT-6**	**CPT-5**
0–12 [0.0–0.3]	10	9	1.93 [40]
12–24 [0.3–0.6]	19	22	2.24 [47]

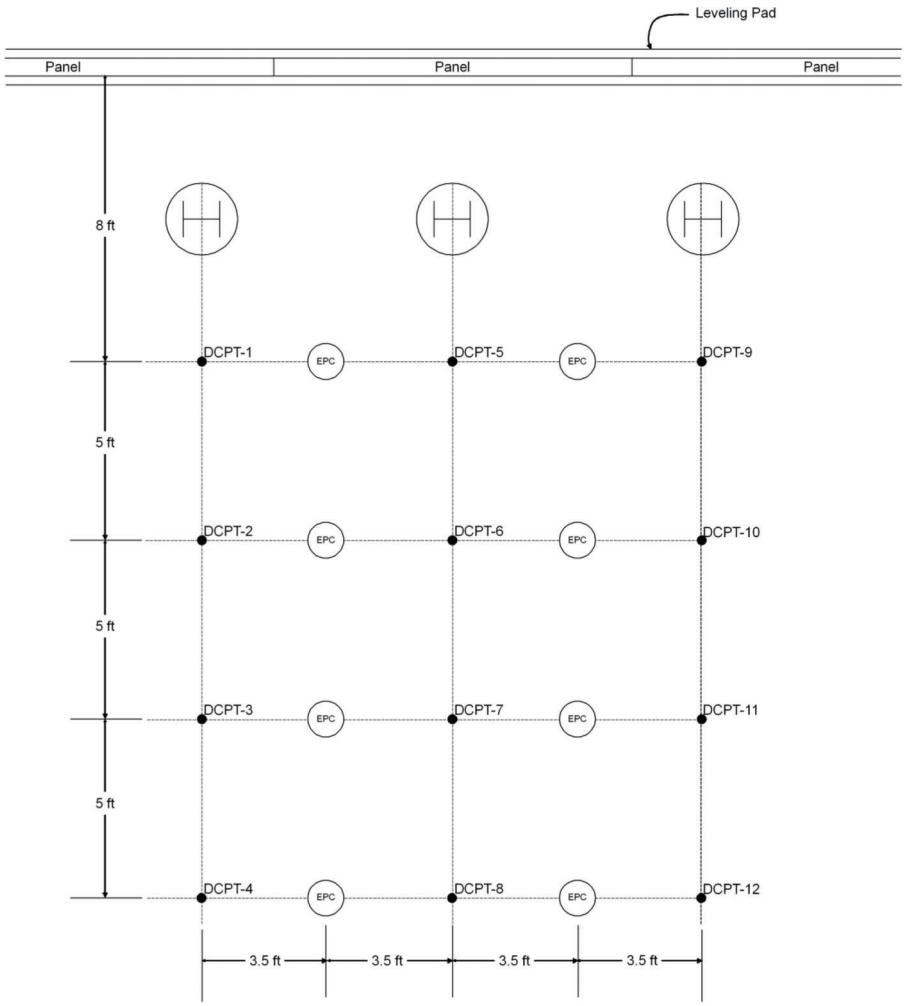

Figure 5.4 Plan view of the layout of the DCPTs performed adjacent to the earth pressure cells near the base of the MSE wall foundation.

17%, while those for 24–28 in. (0.6–0.7 m) penetration are 6 and 18%, respectively. These DCPT results correspond to measured vertical stresses equal to $2\gamma H$ at the base of the leveling pad and approximately γH along the base of the reinforced fill at the end of wall construction, where γ and H are the unit weight and height of the reinforced fill material [$\approx$ 18.5 kN/m^3 (118 pcf) and 5 m (16.3 ft) for the Whitestown MSE wall]. Note that the DCPTs were performed prior to the placement and compaction of the reinforced fill material.

5.3 Application of *INDOT Construction Memorandum 15–08* to Estimate the Factored Bearing Resistance of the Foundation Soil

Among the four DCPTs performed in the foundation soil prior to wall construction, only DCPT-3 and DCPT-4 are applicable because they correspond to approximately the same elevation as that of the base of the leveling pad (RL = 930.1 ft). In contrast, DCPT-1 and DCPT-2 were performed on the shoulder of I-65, which is at a higher elevation (RL $\approx$ 933.6 ft) than the

base of the leveling pad (Figure 2.3). Referring to the data obtained from DCPT-3, which resulted in smaller blow counts than DCPT-4, we see that the blow counts for 0–12 in. and 12–24 in. penetration depths are equal to 21 and 15, respectively. Taking the average of these two values yields a representative 12-in. DCPT blow count of 18, which corresponds to a factored bearing resistance of 6,600 psf (316 kPa) using the chart in *INDOT Construction Memorandum 15–08* (Table 1.2). The factored bearing resistance of 6,600 psf is greater than the factored bearing pressure [= 5,100 psf (244 kPa)] at the base of the MSE wall foundation specified in the contractor's working drawing for Bent 3 of the Whitestown Parkway Bridge. In addition, the value of 6,600 psf is close to the MSE wall factored bearing resistance of 7,000 psf (335 kPa) from the geotechnical report [calculated using s_u = 2,100 psf (100 kPa) and N_c = 5.14] and specified in the contract document *FT Plans 1702146 for Contract Services*.

The zone of influence of the DCPT is of the order of one to two cone diameters below the cone tip. Therefore, the DCPT can only test whether the initial 1–2 ft (0.3–0.6 m) of material below the MSE wall foundation is strong enough to support the wall, but if the top layer is underlain by a layer of weak soil (e.g., soft clay), the DCPT cannot capture the low shear strength of the weak layer. This should be kept in mind when considering potential correlations between the DCPT penetration index and the CPT cone resistance, with the intent of estimating a representative undrained shear strength s_u to calculate the limit unit bearing capacity q_{bL} of MSE wall foundations in fine-grained soils. While the DCPT-based approach does not appropriately characterize MSE wall foundation bearing resistance (due to shallow measurement depth), it could be used to ensure that soil layers at shallow depth transfer the loads effectively from the MSE wall foundation to deeper layers in the soil profile. Other *in situ* tests can be used to assess the undrained shear strength profile with depth to make an assessment of the foundation soil bearing capacity. Note that additional limit states, including those related to MSE wall serviceability and global stability, would need to be checked separately from the bearing capacity limit state.

If some portion of the weak foundation soil needs to be excavated and replaced with B-borrow material, performing a CPT as part of the initial site investigation would be useful to properly identify the depth of excavation required to remove weak foundation soils because the CPT, unlike the SPT, provides continuous profiling measurements with depth. The consistency of the CPT results, in contrast to the variability of the SPT data, would provide a reliable assurance of the type of material that lies below the MSE wall foundation. The following preliminary guidelines may be used to determine the required depth of excavation below the MSE wall foundation based on SPT and CPT data.

- Excavate weak, fine-grained, surficial soil layers (soils with N_{60} < 10–15 or q_t < 15–20 tsf; where N_{60} = corrected SPT blow count, and q_t = corrected, total cone resistance).
- For cases where weak soil layers exist near the ground surface, a minimum depth of excavation of about 6–9B_{lp} below the leveling pad (based on elasticity theory and the 2:1 stress distribution method) is suggested to minimize potential issues related to the stability and settlement of the leveling pad (B_{lp} is the width of the leveling pad).

The undrained shear strength s_u can be obtained from laboratory test results or calculated from q_t using Eq. 1.3. The factored bearing resistance of the MSE wall foundation in fine-grained soil is then calculated in accordance with AASHTO (2020) using the bearing capacity equation (Eq. 1.14), with a representative undrained shear strength determined within the depth of influence of the MSE wall foundation ($\approx 1B$ below the base of the MSE wall); where B is the width of the MSE wall foundation. The preliminary guidelines provided in this section of the report can be refined and improved as additional data is collected in the context of MSE wall INDOT projects.

5.4 Estimation of Bearing Capacity of Leveling Pad in B-Borrow Material

The top 5 ft (1.5 m) of clayey foundation soil was excavated along the footprint of the reinforced fill and replaced with compacted B-borrow material prior to construction of the MSE wall. The 1-ft-(0.3-m)-wide leveling pad was then constructed on top of the compacted B-borrow material. Given the high vertical stresses measured at the base of the leveling pad, it is of interest to calculate the limit unit bearing capacity of the leveling pad and compare this value with the measured stresses. The limit unit bearing capacity q_{bL} of the leveling pad can be calculated by following these steps.

1. The results of the 12 DCPTs performed in compacted B-borrow material indicate that the mean DCPT blow count for 0–12 in. (0–0.3 m) penetration is 8 blows. According to Ganju et al. (2018), for a clean sand with C_U = 3.0 and a 0–12 in. DCPT blow count of 8, the relative compaction (RC) of the soil is estimated to be 97.5%. Assuming a specific gravity G_s of 2.65, the relative density D_R of the B-borrow material (e_{min} = 0.41 and e_{max} = 0.60) works out to be 81%, and, for an *in situ* (placement) water content *wc* of 2.8%, the unit weight γ of the B-borrow material is calculated as 18.5 kN/m^3 (118 pcf).
2. The leveling pad can be idealized as a strip footing, with a width-to-length B/L ratio approximately equal to zero. Following Salgado (2022, p. 470), the representative peak mean effective stress σ'_{mp} below the leveling pad is estimated to be 267 kPa (5,578 psf).
3. Following Bolton (1986), for D_R = 81%, σ'_{mp} = 267 kPa (5,578 psf), and fitting parameters Q = 10 and R_Q = 1 (for clean silica sand), the relative dilatancy index I_R is calculated as 2.57.

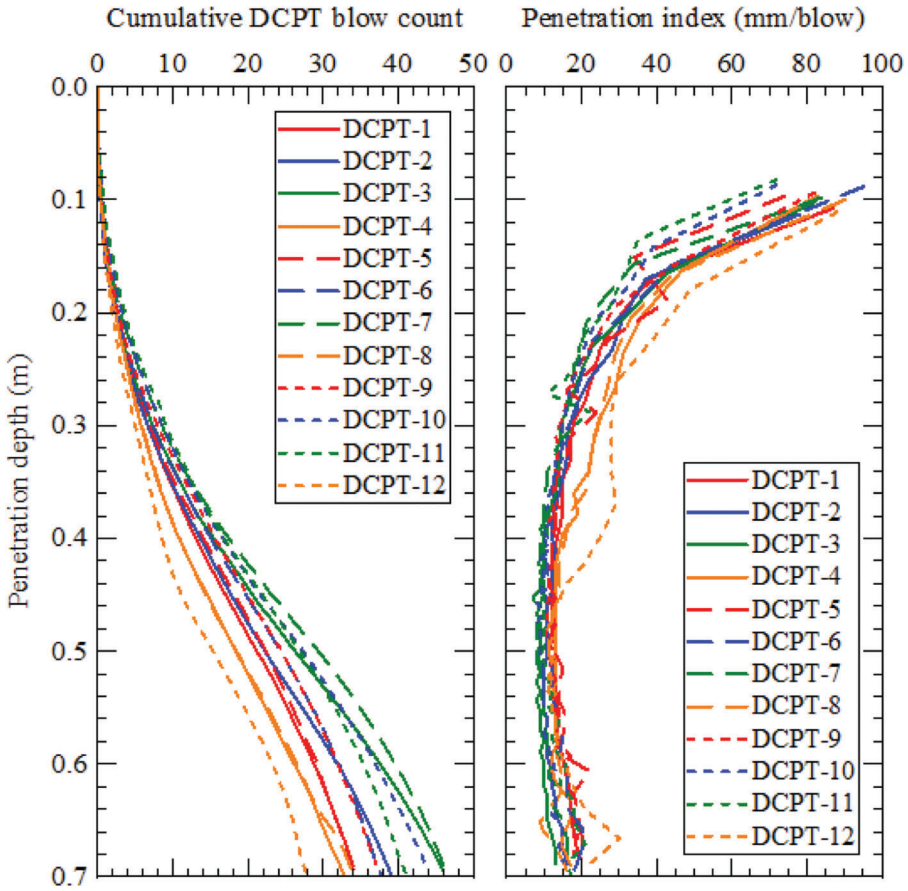

Figure 5.5 Profiles of cumulative DCPT blow count and penetration index for the B-borrow material below the pressure cells.

TABLE 5.3
Values of DCPT blow count for 0–12 in., 12–24 in., and 24–28 in. penetration depths in the B-borrow material below the pressure cells

	Penetration Depth (in.) [m]		
DCPT	**0–12 [0.0–0.3]**	**12–24 [0.3–0.6]**	**24–28 [0.6–0.7]**
DCPT-1	7	23	5
DCPT-2	7	26	7
DCPT-3	8	31	8
DCPT-4	6	21	7
DCPT-5	8	22	5
DCPT-6	8	25	5
DCPT-7	9	32	6
DCPT-8	7	21	7
DCPT-9	9	24	5
DCPT-10	9	29	7
DCPT-11	10	26	6
DCPT-12	6	18	4
Mean	*8*	*25*	*6*
COV (%)	*16*	*17*	*18*

4. The critical-state friction angle $\phi_{c,\mathrm{DS}}$ of B-borrow material in direct shear is assumed to be 31.9° (the same value as that of the reinforced fill material). However, plane-strain conditions are in effect below the leveling pad. Given that the critical-state friction angle $\phi_{c,\mathrm{TXC}}$ of sand in triaxial compression is typically 1° less than that in direct shear (Han et al., 2018), and the fact that the critical-state friction angle $\phi_{c,\mathrm{PS}}$ of sand for plane-strain conditions is generally 3°–5° greater than that in triaxial compression (Chakraborty & Salgado, 2010; Loukidis & Salgado, 2009b; Pradhan et al., 1988; Sutherland & Mesdary, 1969), a conservative (lower-bound) estimate for the value of $\phi_{c,\mathrm{PS}}$ for B-borrow material is 33.9°. The representative peak friction angle ϕ_p and peak dilatancy angle ψ_p of the B-borrow material are then calculated as 46.7° (Bolton, 1986) and 16.1° (Schanz & Vermeer, 1996).
5. Following Loukidis and Salgado (2009a), the bearing capacity factors N_q and N_γ considering flow rule non-associativity are calculated as 109 and 205, respectively.
6. The unfactored limit unit bearing capacity q_{bL} of the 1-ft-(0.3-m)-wide leveling pad is then estimated to be 577 kPa (12,059 psf). Given that the vertical stress measured at the base of the leveling pad is 190 kPa (3,968 psf) at the end of wall construction, the factor of safety of the leveling pad against bearing capacity failure is equal to 3.0 for the Whitestown MSE wall. After the bridge was constructed on top of the MSE wall and opened to traffic, the factor of safety decreased to a value of 2.3 due to a 65-kPa (1,358-psf) increase in vertical stress measured at the base of the leveling pad.
7. Further research is needed to develop a suitable resistance factor for estimation of the factored limit unit bearing capacity of the leveling pad using the

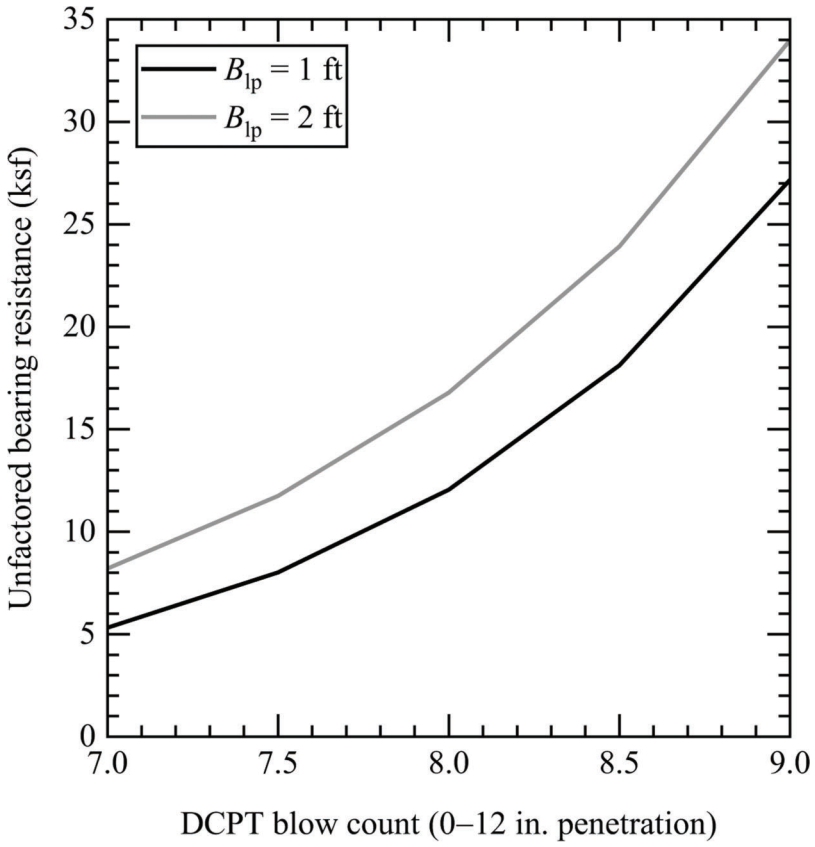

Figure 5.6 Estimation of unfactored (limit) bearing resistance of the leveling pad in B-borrow material based on the DCPT blow count.

TABLE 5.4
Values of unfactored (limit) bearing resistance of the leveling pad in B-borrow material based on the DCPT blow count

	Unfactored Bearing Resistance (psf)	
DCPT Blow Count (0–12 in. penetration)	**B_{lp} = 1 ft**	**B_{lp} = 2 ft**
7.0	5,000	8,000
7.5	8,000	11,500
8.0	12,000	16,500
8.5	18,000	24,000
9.0	27,000	34,000

Note: B_{lp} = width of the leveling pad. A representative DCPT blow count calculated based on the results of multiple DCPTs performed along the leveling pad footprint is recommended.

above procedure. However, for illustration, if we use the resistance factor (= 0.65) recommended by AASHTO (2020) for the MSE wall foundation bearing capacity limit state, the factored bearing resistance of the leveling pad is equal to 375 kPa (7,838 psf), which exceeds the factored bearing pressure [= 244 kPa (5,100 psf)] at the base of the MSE wall foundation specified in the contractor's working drawing.

Figure 5.6 shows the unfactored (limit) bearing resistance of the leveling pad in B-borrow material (calculated using the above procedure) versus the 0–12 in. (0–0.3 m) DCPT blow count for pad widths B_{lp} equal to 1 ft (0.3 m) and 2 ft (0.6 m). For simplicity, the effects of embedment depth and load inclination/eccentricity were not considered in the bearing capacity calculations for the leveling pad. AASHTO (2020) does not provide a procedure to calculate the bearing capacity of the leveling pad, instead bearing capacity calculations are prescribed for the entire width of the MSE wall (taken as equal to the length of the reinforcement). However, AASHTO (2020) specifies a minimum embedment depth for the leveling pad to "preclude local bearing resistance failure under the leveling pad due to the high vertical stresses transmitted by the facing." The embedment depth is measured from the top of the finished grade in front of the wall to the

top of the leveling pad. According to AASHTO (2020), the minimum embedment depth of the leveling pad is equal to $0.05H$ for MSE walls and $0.1H$ for MSE abutments constructed on level ground, where H is the wall height (measured from the top of the leveling pad to the top of the wall). For the Whitestown MSE abutment, the depth of embedment of the leveling pad is approximately 2.5 ft (0.75 m), corresponding to a value of $0.13H$. Additional considerations for the minimum embedment depth of the leveling pad based on scour, frost penetration, and construction on sloping ground are given in AASHTO (2020).

Table 5.4 summarizes the values of the unfactored (limit) bearing resistance of the leveling pad in B-borrow material based on the DCPT blow count. A minimum of eight DCPTs performed along the footprint of the leveling pad is suggested to obtain a representative 0–12 in. DCPT blow count. Further research is needed to validate the preliminary procedure used in this study to estimate the unfactored (limit) bearing resistance of the leveling pad in compacted B-borrow material based on the 0–12 in. DCPT blow count. Also, as mentioned previously, further research is needed to develop a suitable resistance factor for estimation of the factored bearing resistance of the leveling pad using this procedure. The resulting factored bearing resistance of the leveling pad should exceed the factored bearing pressure at the base of the MSE wall foundation specified in the contractor's working drawing.

6. SUMMARY AND CONCLUSIONS

This report presented the results of a comprehensive study of the performance of a steel strip-reinforced, mixed MSE abutment wall in Whitestown, Indiana, USA, during construction and while in service. The MSE abutment was instrumented with an array of sensors to measure and obtain several quantities of interest, such as the dead and live loads carried by the piles and pile cap, the vertical stresses at the base of the leveling pad and within the reinforced fill, the lateral stresses behind the wall facing, the tensile loads in the reinforcements, and the vertical and lateral displacements of the MSE wall. The data collected from the sensors were compared with predictions obtained from MSE wall design methods specified in AASHTO (2020) as well as other methods available in the literature. A live load test was performed by parking twelve triaxle trucks at different locations along the approach to the instrumented MSE abutment as well as on the bridge deck near the abutment. Based on the results of this study, we can draw the following conclusions.

1. The vertical stresses measured at the base of the 1-ft-(0.3-m)-wide leveling pad are greater than those calculated based on the self-weight of the wall facing both during and after wall construction. The ratio of these quantities increased from 1.6 at stage 1 of wall construction to 2.4 at the end of wall construction (stage 5), and, subsequently, to 3.2 after the bridge was constructed and opened to traffic (stage 11). The additional vertical stress transferred to the leveling pad are attributed mainly to the downward shear stresses mobilized along the facing-soil interface and possibly some downdrag forces at the reinforcement-panel connections. These additional stresses should be considered in bearing capacity calculations. Settlement calculations should also be performed to ensure that tolerable settlement values are not exceeded, particularly if weak soil layers exist at shallow depths below the B-borrow material. To address these concerns, consideration should be given to increasing the width of the leveling pad for MSE walls (this is even more important for walls taller than the one instrumented in this study). For the Whitestown MSE abutment wall, the factor of safety for the leveling pad against bearing capacity failure was estimated to be 3.0 at the end of wall construction and 2.3 after the bridge was constructed and opened to traffic.
2. Based on the data obtained from the three instrumented piles and the instrumented zone of the pile cap around these piles, the piles carried about 90% of the dead load from the superstructure during bridge construction, while the remaining 10% was carried by the fill material in contact with the pile cap. At the end of bridge construction, the piles carried about 92% [= 1,316 kN (296 kips)] of the dead load [= 1,430 kN (322 kips)] from the bridge superstructure, resulting in a mobilized cap resistance equal to 8% [= 114 kN (26 kips)] of the superstructure load (the cap resistance decreased to 6% after 4 months of traffic on the bridge). Assuming no contribution from cap resistance (as is typically done in MSE abutment design), the average dead load per pile, based on the data obtained for the three instrumented piles, is 477 kN (107 kips) at the end of bridge construction. This value is in good agreement with the unfactored dead load of 456 kN (103 kips) per pile used in the design of Bent 3 of the Whitestown Parkway Bridge. During the live load test, approximately 91% of the live load in the instrumented zone of the pile cap was carried by the three instrumented piles, while the remaining 9% of the live load was carried by the fill material in contact with the pile cap.
3. The vertical stresses below the centerline of the pile cap and the lateral stresses on the back of the wall facing increased by 12–16 kPa (251–334 psf) and 4–9 kPa (83–188 psf) at the end of bridge construction compared to those measured at the end of construction of the MSE wall. Both the vertical and lateral stresses were generally constant during the period of time from the end of bridge construction up to 4 months after the bridge was opened to traffic. During the live load test, the vertical stresses measured by the pressure cells within the MSE abutment increased by 5–9 kPa (104–188 psf) compared to those measured before the test, whereas the lateral stresses on the back of the wall facing increased by 1–4 kPa (21–84 psf). The lateral earth pressure coefficient K_r at the end of wall construction ranged from 0.2 to 0.5 (with higher values observed near the bottom of the wall); K_r increased to values ranging from 0.3 to 0.6 after the bridge was constructed and opened to traffic.
4. The values of K_r back-calculated from the reinforcement strain gauge data were in good agreement with those determined from the lateral stresses measured by the pressure cells on the back of the wall facing, except

for the bottommost reinforcement level, where K_r from the strain gauge data was smaller than that obtained from the pressure cell data, both during and after bridge construction. The coherent gravity method and the simplified method underpredict the lateral stresses measured on the back of the bottommost facing panel due to the passive resistance provided by the compacted sandy soil placed in front of it during wall construction.

5. At the end of wall construction, the ratio of the tensile load T_{con} near the reinforcement-panel connection to the maximum tensile load T_{max} in the reinforcement is in the range of 0.4 to 0.6. However, after the bridge was constructed and opened to traffic, the ratio T_{con}/T_{max} ranged from 0.4 to 0.95, with higher values corresponding to reinforcement levels located closer to the base of the pile cap. This observation supports the AASHTO (2020) recommendation of performing the reinforcement-panel connection limit state check with $T_{con}/T_{max} = 1.0$ for internal stability design of MSE bridge abutments.
6. The coherent gravity method, the simplified method, and the simplified stiffness method are sensitive to the value of the backfill soil peak friction angle ϕ_p used to calculate T_{max} at the end of wall construction. For $\phi_p = 40^\circ$, the simplified stiffness method provides the best estimate of T_{max} for the four instrumented levels of steel strips considered in this study, whereas for $\phi_p = 34^\circ$, the methods generally overpredict the maximum reinforcement tensile loads at the end of wall construction. Note that these methods have been calibrated specifically for MSE walls at the end of wall construction, i.e., under initial operational conditions. For the Whitestown MSE abutment wall, the value of T_{max} increased by about 3%–5% during the period of time from the end of bridge construction up to 4 months after the bridge was opened to traffic. Because the contribution of dilatancy towards soil shear strength may progressively degrade during the service life of the MSE abutment wall due to traffic and other events (e.g., earthquakes and rainstorms), the critical-state friction angle ϕ_c of the backfill soil could be the most appropriate value of friction angle to use in MSE abutment wall design.
7. Most of the lateral displacement of the wall facing occurred during construction of the MSE wall. The maximum lateral displacement of the wall facing was 10 mm (0.4 in.) at the end of wall construction, and it increased by a maximum value of 2.1 mm (0.08 in.) at the end of bridge construction. Based on the positions of the tilt sensors along the inclinometer string, the maximum lateral displacement of the wall facing [= 12.1 mm (0.48 in.)] at the end of bridge construction occurred at a depth of 2.8 m (9.2 ft) below the top of the reinforced fill; this is close to the depth where the maximum tensile load T_{max} [= 21.8 kN/m (1,494 lb/ft)] was measured in the instrumented steel strips. During the live load test, the lateral displacement of the wall facing increased by a maximum value of 0.8 mm (0.03 in.) compared to that measured before the test; this occurred at a depth of 0.3 m (1 ft), which is near the elevation of the topmost reinforcement level, where the largest increment in tensile load [= 0.9 kN/m (62 lb/ft)] was measured during the test.
8. The vertical displacement w of the MSE wall foundation (below the leveling pad) increased from 20 mm (0.8 in.) at the end of wall construction to 26 mm (1.02 in.) at the end of bridge construction; no significant change in pad settlement was observed during the live load test. The relative settlement w/B of the leveling pad was 6.5% at the end of wall construction and 8.5% at the end of bridge construction. The value of the secant modulus of subgrade reaction of the leveling pad decreased by 20%, from 11,450 kPa/m (73 ksf/ft) for a pad settlement of 12.7 mm (0.5 in.) to 9,150 kPa/m (58 ksf/ft) for a pad settlement of 25.4 mm (1 in.).
9. The results of the DCPTs performed in the foundation soil prior to wall construction show that the factored bearing resistance [= 6,600 psf (316 kPa)] obtained using the chart in *INDOT Construction Memorandum 15–08* is greater than the factored bearing pressure [= 5,100 psf (244 kPa)] at the base of the MSE wall foundation specified in the contractor's working drawing. In addition, the value of 6,600 psf (316 kPa) is close to the MSE wall factored bearing resistance of 7,000 psf (335 kPa) derived from the geotechnical report (based on the bearing capacity equation) and specified in the project contract documents.
10. The results of the DCPTs performed in compacted B-borrow material near the pressure cells at the base of the MSE wall foundation show that the mean DCPT blow count values for 0–12 in. (0–0.3 m), 12–24 in. (0.3–0.6 m), and 24–28 in. (0.6–0.7 m) penetration depths are equal to 8, 25, and 6, respectively. These blow counts correspond to measured vertical stresses equal to $2\gamma H$ at the base of the leveling pad and approximately γH along the base of the reinforced fill at the end of construction of 16 ft (5 m) of reinforced fill material.

The results obtained in this study could be used as a practical reference for acceptable performance of MSE abutment walls of similar heights constructed in similar soil profiles in Indiana. Additional CPT, DCPT, and plate load tests performed in test pads of compacted B-borrow material as well as in different foundation soil profiles in Indiana along with long-term monitoring of instrumented MSE walls constructed with different heights would be desirable to expand the applicability of the findings of this study. The corners of an MSE wall, where the abutment wall meets the wing wall, could be considered for instrumentation to investigate the possibility of wall distress that may occur at these critical locations. In addition, pressure cells could be installed on the front face of the bottommost facing panel to measure the passive resistance provided by the soil placed in front of it both during and after wall construction.

REFERENCES

AASHTO. (1994). *Standard specifications for highway bridges*. American Association of State Highway and Transportation Officials.

AASHTO. (1996). *Standard specifications for highway bridges* (16th ed.). American Association of State Highway and Transportation Officials.

AASHTO. (2008). *Standard specification for classification of soils and soil-aggregate mixtures for highway construction*

purposes (AASHTO M 145–91). American Association of State Highway and Transportation Officials.

AASHTO. (2012). *AASHTO LRFD bridge design specifications* (6th ed.). American Association of State Highway and Transportation Officials.

AASHTO. (2020). *AASHTO LRFD bridge design specifications* (9th ed.). American Association of State Highway and Transportation Officials.

Abu-Hejleh, N., Wang, T., & Zornberg, J. G. (2000). Performance of geosynthetic-reinforced walls supporting bridge and approaching roadway structures. In J. G. Zornberg and B. R. Christopher (Eds.), *Proceedings of Geo-Denver 2000: Advances in Transportation and Geoenvironmental Systems Using Geosynthetics* (pp. 218–243). American Society of Civil Engineers.

Abu-Hejleh, N., Zornberg, J. G., Elias, V., & Watcharamonthein, J. (2003). Design assessment of the Founders/Meadows GRS abutment structure. In *Proceedings of the 82nd Annual Meeting of the Transportation Research Board* (pp. 1–19).

Abu-Hejleh, N., Zornberg, J. G., Wang, T., & Watcharamonthein, J. (2002). Monitored displacements of unique geosynthetic-reinforced soil bridge abutments. *Geosynthetics International*, *9*(1), 71–95. https://doi.org/10.1680/gein.9.0211

Allen, T. M., & Bathurst, R. J. (2015). Improved simplified method for prediction of loads in reinforced soil walls. *Journal of Geotechnical and Geoenvironmental Engineering*, *141*(11), 04015049. https://doi.org/10.1061/(ASCE)GT.1943-5606.0001355

Allen, T. M., & Bathurst, R. J. (2018). Application of the simplified stiffness method to design of reinforced soil walls. *Journal of Geotechnical and Geoenvironmental Engineering*, *144*(5), 04018024. https://doi.org/10.1061/(ASCE)GT.1943-5606.0001874

Allen, T., Christopher, B., Elias, V., & DiMaggio, J. (2001, July). *Development of the simplified method for internal stability design of mechanically stabilized earth (MSE) walls* (Report No. WA-RD 513.1). Washington State Department of Transportation.

Anderson, P. L., & Brabant, K. (2005). Increased use of MSE abutments. *Proceedings of the 22nd Annual International Bridge Conference* (Paper 5–10).

Anderson, P. L., Gladstone, R. A., & Sankey, J. E. (2012). State of the practice of MSE wall design for highway structures. *Geotechnical Engineering State of the Art and Practice: Keynote Lectures from GeoCongress 2012* (pp. 443–463). American Society of Civil Engineers.

Anderson, P. L., Gladstone, R. A., & Withiam, J. L. (2010). Coherent gravity: The correct design method for steel-reinforced MSE walls. *Proceedings of Earth Retention Conference 3*, 512–521. American Society of Civil Engineers.

ASTM. (2017). *ASTM D2487: Standard practice for classification of soils for engineering purposes (unified soil classification system)*. ASTM International.

ASTM. (2018a). *ASTM D6951: Standard test method for use of the dynamic cone penetrometer in shallow pavement applications*. ASTM International.

ASTM. (2018b). *ASTM A572/A572M: Standard specification for high-strength low-alloy columbium-vanadium structural steel*. ASTM International.

ASTM. (2018c). *ASTM D2000: Standard classification system for rubber products in automotive applications*. ASTM International.

Balunaini, U., & Prezzi, M. (2010). Interaction of ribbed-metal-strip reinforcement with tire shred-sand mixtures. *Geotechnical and Geological Engineering*, *28*(2), 147–163.

Bareither, C. A., Benson, C. H., & Edil, T. B. (2008). Comparison of shear strength of sand backfills measured in small-scale and large-scale direct shear tests. *Canadian Geotechnical Journal*, *45*(9), 1224–1236. https://doi.org/10.1139/T08-058

Bastick, M., Schlosser, F., Segrestin, P., Amar, S., & Canepa, Y. (1993). Experimental reinforced earth structure of Bourron Marlotte: Slender wall and abutment test. In *Reinforcement des sols: Experimentations en vraie grandeur des annees*, *80*, 201–228. Presses de L'École Nationale des Ponts et Chaussees.

Bathurst, R. J. (2014). Reinforced soil walls–design and construction. *The Bridge and Structural Engineer*, *44*(3), 15–24.

Bathurst, R. J. (2019). Developments in MSE wall research and design. In F. Tatsouka, E. Guler, H. Shehata, and J. P. Giroud (Eds.), *Innovative Infrastructure Solutions Using Geosynthetics* (pp. 22–50). Springer.

Bathurst, R. J., Bozorgzadeh, N., & Allen, T. (2021). LRFD calibration of internal limit states for MSE walls using steel strip reinforcement. *Journal of Geotechnical and Geoenvironmental Engineering*, *147*(12), 04021156. https://doi.org/10.1061/(ASCE)GT.1943-5606.0002678

Bathurst, R. J., Nernheim, A., & Allen, T. M. (2008). Predicted and measured loads using the coherent gravity method. *Proceedings of the Institution of Civil Engineers - Ground Improvement*, *161*(3), 113–120. https://doi.org/10.1680/grim.2008.161.3.113

Bathurst, R. J., Nernheim, A., & Allen, T. M. (2009). Predicted loads in steel reinforced soil walls using the AASHTO simplified method. *Journal of Geotechnical and Geoenvironmental Engineering*, *135*(2), 177–184. https://doi.org/10.1061/(ASCE)1090-0241(2009)135:2(177)

Bisht, V., Salgado, R., & Prezzi, M. (2021). Material point method for cone penetration in clays. *Journal of Geotechnical and Geoenvironmental Engineering*, *147*(12), 04021158. https://doi.org/10.1061/(ASCE)GT.1943-5606.0002687

Bisht, V., Salgado, R., & Prezzi, M. (2024). Simulation of cone penetration in soil using the material point method. *Computer Geotechnology*, *172*, 106430. https://doi.org/10.1016/j.compgeo.2024.106430

Bolton, M. D. (1986). The strength and dilatancy of sands. *Géotechnique*, *36*(1), 65–78. https://doi.org/10.1680/geot.1986.36.1.65

Bolton, M. D. (1991a). *Geotechnical stress analysis: A possible approach for cantilever retaining walls on spread foundations* (Contractor Report 271). Transport and Road Research Laboratory.

Bolton, M. D. (1991b). *Geotechnical stress analysis for bridge abutment design* (Contractor Report 270). Transport and Road Research Laboratory.

Bolton, M. D. (1996). Geotechnical design of retaining walls. *The Structural Engineer*, *74*(21), 365–369.

Bolton, M. D., & Pang, P. L. R. (1982, December). Collapse limit states of reinforced earth retaining walls. *Géotechnique*, *32*(4), 349–367. https://doi.org/10.1680/geot.1982.32.4.349

Boutet, M., Doré, G., Bilodeau, J.-P., & Pierre, P. (2011). Development of models for the interpretation of the dynamic cone penetrometer data. *International Journal of*

Pavement Engineering, *12*(3), 201–214. https://doi.org/10.1080/10298436.2010.488727

Bowser-Morner, Inc. (2020). *Laboratory analysis of structure backfill sample* (Report No. 302184). Bowser-Morner, Inc.

Bozorgzadeh, N., Bathurst, R. J., Allen, T. M., & Miyata, Y. (2020). Reliability-based analysis of internal limit states for MSE walls using steel-strip reinforcement. *Journal of Geotechnical and Geoenvironmental Engineering*, *146*(1), 04019119.

Brooker, E. W., & Ireland, H. O. (1965). Earth pressures at rest related to stress history. *Canadian Geotechnical Journal*, *2*(1), 1–15.

Caquot, A., & Kérisel, J. (1953). Sur le terme de surface dans le calcul des fondations en milieu puélverent. *3rd International Conference on Soil Mechanics and Foundation Engineering* (pp. 336–337).

Carraro, J. A. H., Prezzi, M., & Salgado, R. (2009). Shear strength and stiffness of sands containing plastic or nonplastic fines. *Journal of Geotechnical and Geoenvironmental Engineering*, *135*(9), 1167–1178.

Chakraborty, T., & Salgado, R. (2010). Dilatancy and shear strength of sand at low confining pressures. *Journal of Geotechnical and Geoenvironmental Engineering*, *136*(3), 527–532.

Chida, S., & Nakagaki, M. (1979). Test and experiment on a full-scale model of reinforced earth wall. *Proceedings of International Conference on Soil Reinforcement*, *2*, 533–538.

Christopher, B. R. (1993). *Deformation response and wall stiffness in relation to reinforced soil wall design* [Doctoral Dissertation, Purdue University]. Purdue e-Pubs. https://docs.lib.purdue.edu/dissertations/AAI9420806/

Christopher, B. R., Gill, S. A., Giroud, J.-P., Juran, I., Mitchell, J. K., Schlosser, F., & Dunnicliff, J. (1990, November). *Reinforced soil structures volume I. Design and construction guidelines* (Publication No. FHWA-RD-89–043). Federal Highway Administration.

Christopher, B. R., Schwartz, C., & Boudreau, R. (2006). *Geotechnical aspects of pavements* (Publication No. FHWA NHI-05–037). National Highway Institute.

Coulomb, C. A. (1776). Essai sur une application des règles de maximis & minimis à quelques problèmes de statique relatifs à l'architecture. *Memoires de Mathematique de l'Academie Royale de Science*, *7*, 343–382.

Dagger, R., Saftner, D., & Mayne, P. W. (2018). *Cone penetration test design guide for state geotechnical engineers* (Report No. MN/RC 2018–32). Minnesota Department of Transportation.

Damians, I. P., Bathurst, R. J., Josa, A., Lloret, A., & Albuquerque, P. J. R. (2013). Vertical-facing loads in steel-reinforced soil walls. *Journal of Geotechnical and Geoenvironmental Engineering*, *139*(9), 1419–1432.

Damians, I. P., Bathurst, R. J., Lloret, A., & Josa, A. (2016). Vertical facing panel-joint gap analysis for steel-reinforced soil walls. *International Journal of Geomechanics*, *16*(4), 04015103.

Desai, C. S., & El-Hoseiny, K. E. (2005). Prediction of field behavior of reinforced soil wall using advanced constitutive model. *Journal of Geotechnical and Geoenvironmental Engineering*, *131*(6), 729–739.

Desai, C. S., & El-Hoseiny, K. E. (2007). Closure to "Prediction of field behavior of reinforced soil wall using advanced constitutive model" by Chandra S. Desai and Khaled E. El-Hoseiny. *Journal of Geotechnical and Geoenvironmental Engineering*, *133*(1), 123.

Dunnicliff, J., & Green, G. E. (1988). *Geotechnical instrumentation for monitoring field performance*. John Wiley & Sons.

Farouz, E., Esterhuizen, J., & Landers, P. (2004). Performance of MSE walls supporting bridge foundations. In M. K. Yegian and E. Kavazanjian (Eds.), *Proceedings of GeoTrans 2004: Geotechnical Engineering for Transportation Projects* (pp. 2231–2245). American Society of Civil Engineers.

FHWA. (2009a). *Design and construction of mechanically stabilized earth walls and reinforced soil slopes–Volume I* (Publication No. FHWA-NHI-10-024). National Highway Institute, Federal Highway Administration.

FHWA. (2009b). *Design and construction of mechanically stabilized earth walls and reinforced soil slopes–Volume II* (Report No. FHWA-NHI-10–025). Federal Highway Administration, U.S. Department of Transportation.

Ganju, E., Kim, H., Prezzi, M., Salgado, R., & Siddiki, N. Z. (2018). Quality assurance and quality control of subgrade compaction using the dynamic cone penetrometer. *International Journal of Pavement Engineering*, *19*(11), 966–975. https://doi.org/10.1080/10298436.2016.1227664

Ganju, E., Prezzi, M., Salgado, R., Siddiki, N., & Sommer, K. (2015). *QA/QC of subgrade and embankment construction: Technology replacement and updated procedures* (Joint Transportation Research Program Publication No. FHWA/IN/JTRP-2015/01). West Lafayette, IN: Purdue University. https://doi.org/10.5703/1288284315521

Hadala, P. F. (1967). *The effect of placement method on the response of soil stress gages* (Technical Report No. 3–803). U.S. Army Corps of Engineers.

Han, F., Ganju, E., Prezzi, M., & Salgado, R. (2019). Closure to "Effects of interface roughness, particle geometry, and gradation on the sand–steel interface friction angle" by Fei Han, Eshan Ganju, Rodrigo Salgado, and Monica Prezzi. *Journal of Geotechnical and Geoenvironmental Engineering*, *145*(11), 07019017.

Han, F., Ganju, E., Salgado, R., & Prezzi, M. (2018). Effects of interface roughness, particle geometry, and gradation on the sand-steel interface friction angle. *Journal of Geotechnical and Geoenvironmental Engineering*, *144*(12), 04018096.

Han, F., Marashi, M., Prezzi, M., Salgado, R., Wells, T., & Zaheer, M. (2021). Monitoring of the response of the Sagamore Parkway bridge and its foundations during a live load test. *Transportation Research Record: Journal of the Transportation Research Board*, *2675*(3), 358–366. https://doi.org/10.1177/0361198120971263

Han, F., Prezzi, M., Salgado, R., Marashi, M., Wells, T., & Zaheer, M. (2020). *Verification of bridge foundation design assumptions and calculations* (Joint Transportation Research Program Publication No. FHWA/IN/JTRP-2020/18). West Lafayette, IN: Purdue University. https://doi.org/10.5703/1288284317084

Handy, R. L. (1985). The arch in soil arching. *Journal of Geotechnical Engineering*, *111*(3), 302–318.

Handy, R. L. (2007). Discussion: Prediction of field behavior of reinforced soil wall using advanced constitutive model. *Journal of Geotechnical and Geoenvironmental Engineering*, *133*(1), 121–123.

Huang, B., Bathurst, R. J., & Allen, T. M. (2012). LRFD calibration for steel strip reinforced soil walls. *Journal of Geotechnical and Geoenvironmental Engineering*, *138*(8), 922–933.

Huang, J., Han, J., Parsons, R. L., & Pierson, M. C. (2013). Refined numerical modeling of a laterally-loaded drilled shaft in an MSE wall. *Geotextiles and Geomembranes*, *37*, 61–73. https://doi.org/10.1016/j.geotexmem.2013.02.004

INDOT. (2024). *Indiana Department of Transportation standard specifications*. Indiana Department of Transportation. https://www.in.gov/dot/div/contracts/standards/book/sep23/2024%20Standard%20Specifications.pdf

Janabi, F. H., Raja, R. A., Sakleshpur, V. A., Prezzi, M., & Salgado, R. (2023). Experimental study of shape and depth factors and deformations of footings in sand. *Journal of Geotechnical and Geoenvironmental Engineering*, *149*(2), 04022128. https://doi.org/10.1061/JGGEFK.GTENG-10874

Jones, C. J. F. P. (1996). *Earth reinforcement and soil structures: 2nd edition*. Thomas Telford Ltd.

Juran, I., & Schlosser, F. (1978). Theoretical analysis of failure in reinforced earth structures. *Proceedings of Symposium on Earth Reinforcement* (pp. 528–555). American Society of Civil Engineers.

Kim, D. (2008). *Load and resistance factor design of slopes and MSE walls* [Doctoral dissertation, Purdue University]. Purdue e-Pubs. https://docs.lib.purdue.edu/dissertations/AAI3344075/

Kim, D., Bica, A. V. D., Salgado, R., Prezzi, M., & Lee, W. (2009). Load testing of a closed-ended pipe pile driven in multilayered soil. *Journal of Geotechnical and Geoenvironmental Engineering*, *135*(4), 463–473.

Kim, D., & Salgado, R. (2008). *Limit states and load and resistance design of slopes and retaining structures* (Joint Transportation Research Program Publication FHWA/IN/JTRP-2008/05) West Lafayette, IN: Purdue University. https://doi.org/10.5703/1288284314326

Kim, D., & Salgado, R. (2012a). Load and resistance factors for external stability checks of mechanically stabilized earth walls. *Journal of Geotechnical and Geoenvironmental Engineering*, *138*(3), 241–251.

Kim, D., & Salgado, R. (2012b). Load and resistance factors for internal stability checks of mechanically stabilized earth walls. *Journal of Geotechnical and Geoenvironmental Engineering*, *138*(8), 910–921.

Kim, H., Prezzi, M., & Salgado, R. (2010). *Use of dynamic cone penetration and Clegg hammer tests for quality control of roadway compaction and construction* (Joint Transportation Research Program Publication FHWA/IN/JTRP-2010/27). West Lafayette, IN: Purdue University. https://doi.org/10.5703/1288284314246

Kim, K. K., Prezzi, M., & Salgado, R. (2006). *Interpretation of cone penetration tests in cohesive soils* (Joint Transportation Research Program Publication FHWA/IN/JTRP-2006/22). West Lafayette, IN: Purdue University. https://doi.org/10.5703/1288284313387

Kim, K., Prezzi, M., Salgado, R., & Lee, W. (2008). Effect of penetration rate on cone penetration resistance in saturated clayey soils. *Journal of Geotechnical and Geoenvironmental Engineering*, *134*(8), 1142–1153.

Krumbein, W. C., & Sloss, L. L. (1951). *Stratigraphy and sedimentation*. W. H. Freeman and Company.

Lancellotta, R. (2002). Analytical solution of passive earth pressure. *Géotechnique*, *52*(8), 617–619.

Lee, J., Salgado, R., & Carraro, J. A. H. (2004, September). Stiffness degradation and shear strength of silty sands. *Canadian Geotechnical Journal*, *41*(5), 831–843. https://doi.org/10.1139/t04-034

Lee, K. Z. Z., & Wu, J. T. H. (2004). A synthesis of case histories on GRS bridge-supporting structures with flexible facing. *Geotextiles and Geomembranes*, *22*(4), 181–204. https://doi.org/10.1016/j.geotexmem.2004.03.002

Leshchinsky, D., Vahedifard, F., & Leshchinsky, B. A. (2012). Revisiting bearing capacity analysis of MSE walls. *Geotextiles and Geomembranes*, *34*, 100–107. https://doi.org/10.1016/j.geotexmem.2012.05.006

Liang, R. Y., & Almoh, I. M. (2004). Monitoring results of an instrumented, mechanically stabilized earth wall: Comparison with current practice. *Transportation Research Record: Journal of the Transportation Research Board*, *1868*(1), 53–67. https://doi.org/10.3141/1868-06

Loukidis, D., & Salgado, R. (2009a). Bearing capacity of strip and circular footings in sand using finite elements. *Computer Geotechnical*, *36*(5), 871–879. https://doi.org/10.1016/j.compgeo.2009.01.012

Loukidis, D., & Salgado, R. (2009b). Modeling sand response using two-surface plasticity. *Computer Geotech*, *36*(1–2), 166–186.

Loukidis, D., & Salgado, R. (2011). Effect of relative density and stress level on the bearing capacity of footings on sand. *Géotechnique*, *61*(2), 107–119. https://doi.org/10.1680/geot.8.P.150.3771

Lunne, T., Robertson, P. K., & Powell, J. J. M. (1997). *Cone penetration testing in geotechnical practice*. Blakie Academic and Professional.

Luo, Z. (2022). System reliability of mechanically stabilized earth walls incorporating complete external failure modes. *ASCE-ASME Journal of Risk and Uncertainty in Engineering Systems*, *8*(2), 04022006. https://doi.org/10.1061/AJRUA6.0001226

Lyamin, A. V., Salgado, R., Sloan, S. W., & Prezzi, M. (2007). Two- and three-dimensional bearing capacity of footings in sand. *Géotechnique*, *57*(8), 647–662.

Maccarini, M. (1993). A comparison of direct shear box tests with triaxial compression tests for a residual soil. *Geotechnical and Geological Engineering*, *11*, 69–80. https://doi.org/10.1007/BF00423336

Mandolini, A., Russo, G., & Viggiani, C. (2005). Pile foundations: Experimental investigations, analysis and design. *Proceedings of the 16th International Conference on Soil Mechanics and Geotechnical Engineering* (pp. 177–213). Millpress Science Publishers/IOS Press.

Mayne, P. W. (2007). *Cone penetration testing: A synthesis of highway practice* (NCHRP Synthesis Report 368). Transportation Research Board.

Mayne, P. W., & Peuchen, J. (2018). Evaluation of CPTU Nkt cone factor for undrained strength of clays. *Proceedings of 4th International Symposium on Cone Penetration Testing* (pp. 423–429). CRC Press.

Mayne, P. W., & Peuchen, J. (2022). Undrained shear strength of clays from piezocone tests: A database approach. In G. Gottardi and L. Tonni (Eds.), *Cone Penetration Testing 2022* (pp. 546–551). CRC Press.

Meyerhof, G. G. (1953). The bearing capacity of foundations under eccentric and inclined loads. *Proceedings of the 3rd International Conference on Soil Mechanics and Foundation Engineering* (pp. 440–445). https://www.issmge.org/uploads/publications/1/42/1953_01_0090.pdf

Miller, M. A. (2015, May 19). *Construction memo 15–08: Use of "INDOT construction verification chart for factored bearing resistance based on DCP blow counts" for MSE wall* [Construction memorandum]. Indiana Department of Transportation. https://www.in.gov/dot/div/contracts/conmemo/15-08.pdf

Mitchell, J. K., & Christopher, B. R. (1990). North American practice in reinforced soil systems. In P. C. Lambe (Ed.), *Design and Performance of Earth Retaining Structures* (pp. 322–346). American Society of Civil Engineers.

Mitchell, J. K., & Soga, K. (2005, May). *Fundamentals of soil behavior* (3rd ed.). John Wiley & Sons.

Mitchell, J. K., & Villet, W. C. B. (1987, June). *Reinforcement of earth slopes and embankments* (NCHRP Report 290). Transportation Research Board.

Miyata, Y., & Bathurst, R. J. (2012a). Measured and predicted loads in steel strip reinforced c−ϕ soil walls in Japan. *Soils and Foundations*, *52*(1), 1–17. https://doi.org/10.1016/j.sandf.2012.01.009

Miyata, Y., & Bathurst, R. J. (2012b). Analysis and calibration of default steel strip pullout models used in Japan. *Soils and Foundations*, *52*(3), 481–497.

Murthy, T. G., Loukidis, D., Carraro, J. A. H., Prezzi, M., & Salgado, R. (2007). Undrained monotonic response of clean and silty sands. *Géotechnique*, *57*(3), 273–288. https://doi.org/10.1680/geot.2007.57.3.273

NCHRP. (2014). *Non-nuclear methods for compaction control of unbound materials* (NCHRP Synthesis Report 456). National Cooperative Highway Research Program.

Niazi, F. S. (2021). *CPT-based geotechnical design manual, Volume I: CPT interpretation—Estimation of soil properties* (Joint Transportation Research Program Publication No. FHWA/IN/JTRP-2021/22). West Lafayette, IN: Purdue University. https://doi.org/10.5703/1288284317346

Paik, K. H., & Salgado, R. (2003). Estimation of active earth pressure against rigid retaining walls considering arching effects. *Géotechnique*, *53*(7), 643–653. https://doi.org/10.1680/geot.2003.53.7.643

Peattie, K. R., & Sparrow, R. W. (1954). The fundamental action of earth pressure cells. *Journal of the Mechanics and Physics of Solids*, *2*(3), 141–155. https://doi.org/10.1016/0022-5096(54)90021-6

Pierson, M. C. (2008). *Behavior of laterally loaded shafts constructed behind the face of a mechanically stabilized earth block wall* [Master's thesis, University of Kansas]. KU ScholarWorks. https://hdl.handle.net/1808/4053

Pile Dynamics. (2014). *CAPWAP® interactive tutorial*. Pile Dynamics, Inc. https://www.pile.com/resources/demonstration-programs/capwap-interactive-tutorial/

Pradhan, T. B. S., Tatsuoka, F., & Horii, N. (1988). Strength and deformation, characteristics of sand in torsional simple shear. *Soils and Foundations*, *28*(3), 131–148.

Prezzi, M., Salgado, R., Han, F., Raja, R. A., & Kilic, M. (2025). Monitoring of the foundations of a bridge during construction and while in service. *Journal of Geotechnical and Geoenvironmental Engineering*, *151*(6).

Rahman, S., Salgado, R., Prezzi, M., & Becker, P. (2020). *Improvement of stiffness and strength of backfill soils through optimization of compaction procedures and specifications* (Joint Transportation Research Program Publication No. FHWA/IN/JTRP-2020/16). West Lafayette, IN: Purdue University. https://doi.org/10.5703/1288284317134

Raja, R. A., Sakleshpur, V. A., Prezzi, M., & Salgado, R. (2024). Effect of footing geometry and embedment on the bearing capacity and collapse mechanism of shallow foundations in sand. *Journal of Geotechnical and Geoenvironmental Engineering*, *150*(6), 04024042. https://doi.org/10.1061/JGGEFK.GTENG-11802

Raja, R. A., Toshniwal, V., & Salgado, R. (2023). *GIS-based geotechnical database for collaborative GIS* (Joint Transportation Research Program Publication No. FHWA/IN/JTRP-2023/14). West Lafayette, IN: Purdue University. https://doi.org/10.5703/1288284317637

RECo. (2025, May). Construction and quality control manual: Reinforced earth MSE retaining wall system – Rectangular concrete facing panels and steel soil (Version v2025.1). The Reinforced Earth Company. https://www.geoquest-group.us/wp-content/uploads/sites/31/2025/05/RLA-Construction-Manual-v2025.1.pdf

Reissner, H. (1924). Zum erddruckproblem. *Proceedings of 1st International Congress of Applied Mechanics* (pp. 295–311). Delft.

Robertson, P. K. (2009). Interpretation of cone penetration tests—a unified approach. *Canadian Geotechnical Journal*, *46*(11), 1337–1355.

Rowe, P. W. (1969). The relation between the shear strength of sands in triaxial compression, plane strain and direct. *Géotechnique*, *19*(1), 75–86.

Runser, D. J. (1999). *Instrumentation and experimental evaluation of a 17m tall reinforced earth retaining wall* [Master's thesis, Purdue University].

Runser, D. J., Fox, P. J., & Bourdeau, P. L. (2001). Field performance of a 17 m-high reinforced soil retaining wall. *Geosynthetics International*, *8*(5), 367–391. https://doi.org/10.1680/gein.8.0200

Sakleshpur, V. A., Ganju, E., Salgado, R., & Prezzi, M. (2022a). Estimation of optimal spacing between CPT soundings. *Proceedings of Geo-Congress 2022* (pp. 406–414). American Society of Civil Engineers.

Sakleshpur, V. A., Prezzi, M., & Salgado, R. (2022b). Validation of CPT-based methods for estimation of footing settlement in sand. G. Gottardi and T. Laura (Eds.), *Cone Penetration Testing 2022* (pp. 1089–1094). CRC Press.

Sakleshpur, V. A., Prezzi, M., & Salgado, R. (2023). CPT-based design of pile foundations in sand and clay: perspectives. *Proceedings of 8th International Symposium on Deformation Characteristics of Geomaterial* (pp. 1–8).

Sakleshpur, V. A., Prezzi, M., Salgado, R., & Zaheer, M. (2021a). *CPT-based geotechnical design manual, Volume 2: CPT-based design of foundations—Methods* (Joint Transportation Research Program Publication No. FHWA/IN/JTRP-2021/23). West Lafayette, IN: Purdue University. https://doi.org/10.5703/1288284317347

Sakleshpur, V. A., Prezzi, M., Salgado, R., & Zaheer, M. (2021b). *CPT-based geotechnical design manual, Volume 3: CPT-based design of foundations—Example problems* (Joint Transportation Research Program Publication No. FHWA/IN/JTRP-2021/24). West Lafayette, IN: Purdue University. https://doi.org/10.5703/1288284317348

Salgado, R. (2013). The mechanics of cone penetration: Contributions from experimental and theoretical studies. R. Q. Coutinho and P. W. Mayne (Eds.), *Proceedings of Geotechnical and Geophysical Site Characterization 4*, *1*, 131–153. CRC Press.

Salgado, R. (2014). Experimental research on cone penetration resistance. *Geo-Congress 2014 Keynote Lectures: Geo-Characterization and Modeling for Sustainability* (pp. 140–163). American Society of Civil Engineers. https://doi.org/10.1061/9780784413289.007

Salgado, R. (2020). Forks in the road: Rethinking modeling decisions that defined the teaching and practice of geotechnical engineering. In M. Pantazidou, M. Calvello, and M. P. Lopes (Eds.), *Geotechnical Engineering Education 2020* (pp. 51–68). International Society for Soil Mechanics and Geotechnical Engineering.

Salgado, R. (2022). *The engineering of foundations, slopes and retaining structures* (2nd ed.). CRC Press.

Salgado, R. (2024). Forks in the road: Decisions that have shaped and will shape the teaching and practice of geotechnical engineering. *Soils and Rocks*, *47*(2), e2024010123. https://doi.org/10.28927/SR.2024.010123

Salgado, R., Bandini, P., & Karim, A. (2000). Shear strength and stiffness of silty sand. *Journal of Geotechnical and Geoenvironmental Engineering*, *126*(5), 451–462.

Salgado, R., Lyamin, A. V., Sloan, S. W., & Yu, H. S. (2004). Two-and three-dimensional bearing capacity of foundations in clay. *Géotechnique*, *54*(5), 297–306.

Salgado, R., & Prezzi, M. (2007). Computation of cavity expansion pressure and penetration resistance in sands. *International Journal of Geomechanics*, *7*(4), 251–265.

Salgado, R., & Prezzi, M. (2014). Penetration rate effects on cone resistance: Insights from calibration chamber and field testing. *Soils and Rocks*, *37*(3), 233–242.

Salgado, R., & Yoon, S. (2003). *Dynamic cone penetration test (DCPT) for subgrade assessment* (Joint Transportation Research Program Publication FHWA/IN/JTRP-2002/30). West Lafayette, IN: Purdue University. https://doi.org/10.5703/1288284313196

Schanz, T., & Vermeer, P. A. (1996). Angles of friction and dilatancy of sand. *Géotechnique*, *46*(1), 145–151. https://doi.org/10.1680/geot.1996.46.1.145

Schlosser, F. (1978). History, current development and future developments of reinforced earth. *Proceedings of the Symposium on Soil Reinforcing and Stabilizing Techniques*. Transport and Road Research Laboratory.

Schlosser, F., & Bastick, M. (1991). Reinforced earth. In H.-Y. Fang (Ed.), *Foundation Engineering Handbook* (pp. 778–795). Springer.

Schlosser, F., & Segrestin, P. (1979). Dimensionnement des Ouvrages en Terre Armee par la Methode de l'Equilibre Local. *Proceedings of International Conference on Soil Reinforcement: Reinforced Earth and Other Techniques*, *1*, 157–162.

Seo, H., Yildirim, I. Z., & Prezzi, M. (2009). Assessment of the axial load response of an H pile driven in multilayered soil. *Journal of Geotechnical and Geoenvironmental Engineering*, *135*(12), 1789–1804. https://doi.org/10.1061/(ASCE)GT.1943-5606.0000156

Shulyat'ev, O. A., & Kharichkin, A. I. (2009). In-situ measurements of pile-to-pile load distribution in foundations. *Soil Mechanics and Foundation Engineering*, *46*(6), 239–246. https://doi.org/10.1007/s11204-010-9074-8

Singh, K., & Sadeghi, F. (2024). Fundamental relationship between rolling contact fatigue driven surface damage and torsional fatigue. *International Journal of Mechanical Sciences*, *264*, 108831. https://doi.org/10.1016/j.ijmecsci.2023.108831

Skempton, A. W. (1953). The colloidal "activity" of clays. *Proceedings of the 3rd International Conference on Soil Mechanics and Foundation Engineering* (pp. 57–61). International Society for Soil Mechanics and Geotechnical Engineering.

Skempton, A. W. (1986). Standard penetration test procedures and the effects in sands of overburden pressure, relative density, particle size, ageing and overconsolidation. *Geotechnique*, *36*(3), 425–447.

Stark, T. D., Handy, R., & Lustig, M. (2019). MSE wall global stability and lesson learned. In *Geo-Congress 2019: Embankments, Dams, and Slopes* (pp. 277–289).

Strahler, A. W., Walters, J. J., & Stuedlein, A. W. (2016). Frictional resistance of closely spaced steel reinforcement strips used in MSE walls. *Journal of Geotechnical and Geoenvironmental Engineering*, *142*(8), 04016030. https://doi.org/10.1061/(ASCE)GT.1943-5606.0001492

Stuedlein, A. W., Allen, T. M., Holtz, R. D., & Christopher, B. R. (2012). Assessment of reinforcement strains in very tall mechanically stabilized earth walls. *Journal of Geotechnical and Geoenvironmental Engineering*, *138*(3), 345–356. https://doi.org/10.1061/(ASCE)GT.1943-5606.0000586

Sutherland, H. B., & Mesdary, M. S. (1969). The influence of the intermediate principal stress on the strength of sand. *Proceedings of the 7th International Conference on Soil Mechanics and Foundation Engineering (ICSMFE)*, *1*, 391–399. Sociedad Mexicana de Mecanica.

Take, W. A., Bolton, M. D., Wong, P. C. P., & Yeung, F. J. (2004). Evaluation of landslide triggering mechanisms in model fill slopes. *Landslides*, *1*(3), 173–184. https://doi.org/10.1007/s10346-004-0025-1

Taylor, D. W. (1945). *Review of pressure distribution theories: Earth pressure cell investigations and pressure distribution data* (Contract Report W22–053 eng-185). U.S. Army Corps of Engineer Waterways Experiment Station.

Thurairajah, A. (1962). *Some shear properties of kaolin and of sand* [Doctoral dissertation, University of Cambridge]. Apollo. https://doi.org/10.17863/cam.31111

Tovar-Valencia, R. D., Galvis-Castro, A., Salgado, R., & Prezzi, M. (2018). Effect of surface roughness on the shaft resistance of displacement model piles in sand. *Journal of Geotechnical and Geoenvironmental Engineering*, *144*(3), 04017120.

Vesic, A. S. (1973). Analysis of ultimate loads of shallow foundations. *Journal of the Soil Mechanics and Foundations Division*, *99*(1), 45–73.

Wadell, H. (1932). Volume, shape, and roundness of rock particles. *The Journal of Geology*, *40*(5), 443–451.

Wadell, H. (1933). Sphericity and roundness of rock particles. *The Journal of Geology*, *41*(3), 310–331.

Weiler, W. A., Jr., & Kulhawy, F. H. (1982). Factors affecting stress cell measurements in soil. *Journal of the Geotechnical Engineering Division*, *108*(12), 1529–1548. https://doi.org/10.1061/AJGEB6.0001393

Yamashita, K., Yamada, T., & Hamada, J. (2011). Investigation of settlement and load sharing on piled rafts by monitoring full-scale structures. *Soils and Foundations*, *51*(3), 513–532. https://doi.org/10.3208/sandf.51.513

Yin, J.-H., Wang, Y.-J., & Selvadurai, A. P. S. (2001). Influence of nonassociativity on the bearing capacity of a strip footing. *Journal of Geotechnical and Geoenvironmental Engineering*, *127*(11), 985–989.

Zevgolis, L., & Bourdeau, P. L. (2007). *Mechanically stabilized earth wall abutments for bridge support* (Joint Transportation Research Program Publication FHWA/IN/JTRP-2006/38). West Lafayette, IN: Purdue University. https://doi.org/10.5703/1288284313451

Zheng, J., & Hryciw, R. D. (2015). Traditional soil particle sphericity, roundness and surface roughness by computational geometry. *Géotechnique*, *65*(6), 494–506. https://doi.org/10.1680/geot.14.P.192

Zheng, J., & Hryciw, R. D. (2016). Roundness and sphericity of soil particles in assemblies by computational geometry. *Journal of Computing in Civil Engineering*, *30*(6), 04016021. https://doi.org/10.1061/(ASCE)CP.1943-5487.0000578

About the Joint Transportation Research Program (JTRP)

On March 11, 1937, the Indiana Legislature passed an act which authorized the Indiana State Highway Commission to cooperate with and assist Purdue University in developing the best methods of improving and maintaining the highways of the state and the respective counties thereof. That collaborative effort was called the Joint Highway Research Project (JHRP). In 1997 the collaborative venture was renamed as the Joint Transportation Research Program (JTRP) to reflect the state and national efforts to integrate the management and operation of various transportation modes.

The first studies of JHRP were concerned with Test Road No. 1—evaluation of the weathering characteristics of stabilized materials. After World War II, the JHRP program grew substantially and was regularly producing technical reports. Over 1,600 technical reports are now available, published as part of the JHRP and subsequently JTRP collaborative venture between Purdue University and what is now the Indiana Department of Transportation.

Free online access to all reports is provided through a unique collaboration between JTRP and Purdue Libraries. These are available at http://docs.lib.purdue.edu/jtrp.

Further information about JTRP and its current research program is available at http://www.purdue.edu/jtrp.

About This Report

An open access version of this publication is available online. See the URL in the citation below.

Sakleshpur, V. A., Prezzi, M., Salgado, R., Becker, P., & Zafari, Y. (2025). *Monitoring of a steel-reinforced MSE abutment wall and evaluation of its bearing capacity based on the CPT and DCPT* (Joint Transportation Research Program Publication No. FHWA/IN/JTRP-2025/04). West Lafayette, IN: Purdue University. https://doi.org/10.5703/1288284317845